Moving Fast: Neural Constraints in Closed Loop

by

Shreya Saxena

B.Sc., École Polytechnique Fédérale de Lausanne (2009)
M.Sc., Johns Hopkins University (2011)

Submitted to the Department of Electrical Engineering and Computer Science
in partial fulfillment of the requirements for the degree of

Doctor of Philosophy in Electrical Engineering

at the

MASSACHUSETTS INSTITUTE OF TECHNOLOGY

September 2017

Author .... Signature redacted
Department of Electrical Engineering and Computer Science
August 29, 2017

Certified by .... Signature redacted ....
Munther Dahleh
William Coolidge Professor of Electrical Engineering and Computer Science
Thesis Supervisor

Accepted by.................. Signature redacted
Leslie A. Kolodziejski
Professor of Electrical Engineering and Computer Science
Chair, Department Committee on Graduate Students

Moving Fast: Neural Constraints in Closed Loop

by

Shreya Saxena

Submitted to the Department of Electrical Engineering and Computer Science
on August 29, 2017, in partial fulfillment of the
requirements for the degree of
Doctor of Philosophy in Electrical Engineering

Abstract

The generation of fast movements during sensorimotor control is fundamentally limited by the biophysics of neural activity and the physiological dynamics of the muscles involved. Yet, the limiting factors and the corresponding tradeoffs have not been rigorously quantified. We use feedback control principles to identify limitations in the ability of the sensorimotor control system to track intended fast periodic movements. We show that (i) a linear model for movement generation fails to predict known undesirable phenomena encountered in the regime of fast movements, and (ii) the theory of pulsatile control of movement generation allows us to correctly characterize fundamental limitations in this regime.

This thesis identifies the fastest periodic movement possible for given musculoskeletal and neuronal dynamics, which has far-reaching implications in sensorimotor control. The use of neuronal decoders in the Brain Machine Interface setting is discussed; we introduce a real-time decoder of neuronal activity, and derive conditions for its stability in the presence of feedback. The framework developed in this thesis allows us to characterize the effect of compromised neural and physiological activity on movement, and guide the design of corresponding therapeutic measures.

Thesis Supervisor: Munther Dahleh
Title: William Coolidge Professor of Electrical Engineering and Computer Science

This thesis is dedicated to my husband, Purushottam Dixit.

Acknowledgments

First and foremost, I would like to thank my advisor, Munther Dahleh. His technical insights and his ability to quickly grasp concepts were crucial to the development of the ideas presented in this thesis. He has been a big advocate of this work near the end of my PhD, for which I am especially grateful. His advice, interspersed with random conversations, was always a pleasure during my time at LIDS.

Next, I would like to thank my doctoral committee, namely, Sridevi V. Sarma, Emery Brown, and George Verghese, for taking the time out to deftly advise me during this journey. The interdisciplinary nature of this thesis required exactly such an interdisciplinary committee. Sri, who was my Masters' advisor at Johns Hopkins University, was the one who piqued my interest in applying systems and control theoretic methods to neuroscience data, and started me on this career path. She remains an active collaborator for some of the work discussed in this thesis, and her support and insight was invaluable during this time. Emery has kept this research grounded and provided very valuable insight in every meeting. George, who I have also had the chance to TA with, was very helpful, and not hesitant to delve in the details of the projects. He also had the time to think of connections of these projects to other biomedical systems, which I hope to leverage in the future.

Members of Munzer's group were extremely helpful in this journey. Some honorable mentions include the following. Rose, who was the first friend I made at LIDS, having met her during my masters. She was always a great sounding board and an amazing friend. Qingqing, with whom I shared an office for 5 years, whose drive and motivation always impressed me, and who became one of my closest friends here. Cha-yo! Elie, who had a wild path in LIDS, and I could always count on for advice. Giancarlo, who was my other long term office-mate, for 4.5 years, and was always very helpful along my journey. Thank you to many other labmates - Yola, Daria, Yasin, Lina, Ali, Mardavij, Spyros, Tuhin, Flora, Ian, Bomin, Dalton, as well as Mitra and Omer, who are honorary labmates. I would also like to thank Albert and Alina for always getting me in for a meeting, even at the last minute.

I would like to thank all the members of the Laboratory of Information and Decision

Systems (LIDS). I am very proud to call LIDS a home, and though it took a while for me to get there, it was definitely worth it. The enthusiasm of the professors and the administrative assistants were key to this process. Organizing many of the social and professional activities at LIDS - being on various committees, organizing the LIDS student conference - proved to be some of the most enjoyable times here, and I was very happy to join Christina, Omer and Jennifer in these endeavors.

I don't think I would have gotten very far if it was not for my friends at MIT. Kat, one of my best friends and roommate. She was a frequent running and gym buddy. I ran my first half marathon with her, and I have a written promise that she will join me on my next marathon. Sudeep and Abhishek, with whom I have shared many great trips over the years. They were almost the first people I met at MIT, my rocks. The four of us went on many adventures, and they were the source of many interesting topics of discussion over the years. A special thanks to my high school friend Pauline, who lived in Cambridge for a year. I still miss her amazing presence and a whole lot of lattes together. All of you, and others who I am lucky to call friends, thank you for everything.

I would like to thank my family. My sister, Shubhra, and brother-in-law, Pranav, have always called me crazy for doing a PhD, but provided much-needed breaks when we are together. My husband Purushottam's parents, for being extremely helpful every step of the way. My parents, whose support was essential during this process. They have always valued education and health over everything else, which definitely helped me take the step towards a PhD, and more importantly, kept me going. They have always tried to build me up for success, partly by having very successful careers themselves, thus leading by example, and partly by providing great sounding boards when it comes to the big questions.

Finally, thank you to my husband Purushottam for his encouragement during the rough spots, as well as accompanying me in the happy times. Thank you for being up for anything. This thesis is dedicated to you.

Contents

List of Figures

List of Tables

Chapter 1

Introduction

Movement generation is one of the primary goals of the brain. Movements are required for communicating with each other, hunting, feeding, and in fact, all basic activities. The ability to make voluntary movements is the primary difference between the animal kingdom and most plant species.

The mechanism of the generation of movements as an experimental paradigm has been explored in detail for more than a century. The neural control of movements has also been in active exploration since the early 1900's [46, 103], with some of the seminal experiments in movement neuroscience performed in the 1950's [78, 8, 43, 44]. Through the years, the exact mechanism of how movements are driven has been studied at different levels of detail, using diverse methods such as electrophysiology, behavioral, and whole brain imaging methods. In the 1970's, the idea of analyzing discontinuities in simple arm movements in order to study the role of feedback in the generation of movement was popularized [7, 1]. Moreover, the characterization and role of the different types of motor neurons was also studied in great detail during this time [15, 39].

With all these pieces of experimental evidence, we have an excellent idea of the functioning of different types of motor neurons on one hand, and a systems level view of the generation of movements on the other. However, relatively few studies tie these ideas together and delve into the fundamental limitations arising due to the neural control of movement in simple movements. In the first part of this thesis, we focus on the limitations due to neural constraints in the generation of fast movements.

More recently, studies have collected vast amounts of data from neural activity during motor tasks, with a large number of experiments focusing on decoding task information from neural activity [13, 80]. In general, the analysis of movements has long been aided by studies involving the recording of neural signals in order to perform goal-directed movements. These studies, while highlighting the enormous leaps in feats of engineering, also provide us some insight into the role of different brain structures and fundamental questions on the encoding of information by neurons. The paradigm of driving machines like prosthetic devices using neural activity is named brain machine interface (BMI), and is key to testing out ideas in movement generation that are formulated using other basic science techniques. In the second part of this thesis, we provide some results in the BMI setting, again focusing on the fast movement regime.

Understanding movement generation as an optimal feedback control problem is a well-known concept in sensorimotor control [74, 105, 101, 113]. Consider the closed-loop sensorimotor control system (SCS) shown in Fig. 1-1. An anatomical schematic is shown in the left panel, and a block diagram of the SCS is shown in the right panel of Fig. 1-1. We assume that the SCS input is the intended voluntary or reference movement signal, $r(t)$, that exists in some part of the brain (e.g. in parietal regions). The reference input is processed by brain structures including the sensorimotor, premotor and motor cortices, and ultimately the neurons in premotor and motor areas send spike train signals to muscles via the spinal cord. Appropriate muscles are innervated to generate a movement, $z(t)$, as the system attempts to follow or "track" $r(t)$. The generated movement (output of SCS) is then fed back, via proprioceptive and visual feedback, to be processed by structures including the cerebellum and sensorimotor cortex. There are other structures involved in the generation of movements such as the basal ganglia and motor thalamus not explicitly shown.

In this thesis, we focus primarily on the regime of fast movements. Although many experimental studies have analyzed different speeds of movements, we have yet to find studies that explicitly model neural control of movement in the regime of fast movements, i.e., when accurate tracking of movements starts to break down. In the first part of this thesis, we set out to model healthy movement generation in accurate tracking regimes, as well as in fast movement regimes. This leads us to a cutoff speed past which tracking

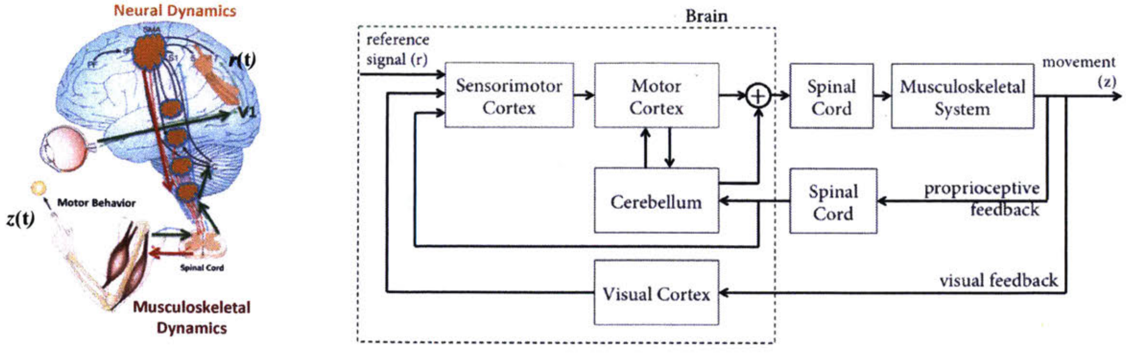

(A) (B)

Figure 1-1: (A) Schematic of the sensorimotor control system. (B) Block diagram of the intact SCS with the relevant structures for movement generation.

suffers; we quantify the dependence of this cutoff speed on the SCS parameters. In the second part of this thesis, in a BMI setting, we consider the reconstruction of movement signals using recorded neural activity, and provide a decoding paradigm that inverts the neural encoding model in real time, and is tunable to function in the fast movement regime. We also provide conditions on the musculoskeletal system and the feedback system such that this decoder is stable in closed loop.

1.1 Models of Neural Activity

We consider neural activity as emanating from the brain and driving the musculoskeletal system in closed loop, as in Figure 1-1A. This section gives a brief overview of some widely accepted models for the activity of single neurons. We consider a neuron to be primarily an input-output device. A neuron communicates information in the form of time-dependent events which capture the end result of a neuron-specific computation. These critical events manifest themselves as sudden spikes in the neuronal transmembrane voltage, and are called action potentials, or spikes [86, 54]. A collection of these binary events in time forms a spike train. The spikes are modulated by both extrinsic factors (e.g. behavioral, visual, auditory stimuli) and intrinsic factors (e.g. the neuron's own spiking history, ensemble activity) [107].

"All models are wrong but some are useful" [5]. We rely on models of neural activity to guide us in the analysis of the neural control of movement; discussions of how to fit the utilized models to data are provided in the relevant chapters. We broadly divide the different types of models describing neural activity into two categories, (i) models of membrane output voltage, and (ii) probabilistic models for spike occurrences. For details on the connections between the models in these two categories, refer to [84].

1.1.1 Models for Membrane Potential

The models in this category characterize the membrane potential of a neuron as a function of the input current provided to the neuron. This input current could be in the form of an electrical stimulation provided directly to the neuron, or the effect of the input neurons' spiking activity. Some of these models only hold for supra-threshold activity, while others are accurate for sub-threshold activity as well. Following are certain key models that fall in this category, with the most detailed model first.

- The **Hodgkin Huxley (HH)** [44] model is one of the most detailed and widely accepted models of the neuron. It is a complex model characterizing the opening and closing of three ion channels, thus modeling the dynamics of the sodium, potassium and calcium currents found in a neuron, as well as the membrane potential of the neuron, using four nonlinear differential equations. Although the subthreshold voltage activity as well as the cellular ionic concentrations are modeled accurately, the model becomes intractable to analyze for the purposes of this study.

- Numerous forms of model reductions of the Hodgkin Huxley model have been documented [33]. The most notable amongst these are the **FitzHugh-Nagumo** [49], the **Hindmarsh Rose** [42] and the **Izhikevich** [48]. Each differs in the exact form of the approximations performed (mainly discounting the dynamics of the slower calcium channel), with the Izhikevich model resorting to a black-box type approach. These nonlinear oscillator-type models have been analyzed using sophisticated tools in nonlinear control theory to, for example, analyze bifurcations in the states to characterize different modes of neuronal activity. For the purposes of this study, where we would like to perform a systems-level analysis, these models are also intractable.

- **Integrate and Fire (IAF) [60, 54, 11]** and its variations have been extensively used in the past to model neural activity. The basic IAF models takes as its input the external current inputting the neuron, which is integrated till a threshold is reached. This integral denotes the subthreshold membrane voltage. Once the threshold is reached, the integral is reset, and a spike or an action potential is emitted; the spike train is considered as the output of this model. The simplest variation of the IAF includes a 'leak' term such that the integral is not held constant for an infinite amount of time if the input stops, but drops naturally in time. This denotes a 'leak' of the membrane potential without a current to keep it at a constant level. This variation is called the 'leaky IAF'. In general, one can add linear dynamics before the threshold operator to create a 'generalized IAF'. This generalized IAF can fit neuronal activity quite accurately [33, 6]. Moreover, theoretical studies have also guaranteed an input-output equivalence between a multiplicative or additive extrinsic signal applied to the HH model, and the same signal applied to an IAF neuron model with variable thresholds [64]. We briefly discuss the implications of this to our work in Chapter 3 and Chapter 5. Important for this thesis, generalized IAF models have been used to model motor neurons in both experimental and computational studies [36, 16].

1.1.2 Probabilistic Models for Spike Occurrences

Several statistics are computed in the neuroscience community to unravel how neurons encode information through spiking activity. The models in this category generate a probabilistic relationship directly between the input stimulus to spike occurrences. They do not attempt to model the subthreshold dynamics of the neuronal membrane voltage, concentrating on the spike train dynamics. The spike train can be discretized into bins of length Δ, and if Δ is small enough, we are left with a discrete time series of 1s and 0s. In this case, the 1s are individual spike times and the 0s are the times at which no spikes occur. The probability of spiking can be expressed as the following, for some function f, and the stimulus $s(t)$.

$$\Pr(\text{spike in}(t, t+\Delta]) \simeq f(s(t))\Delta. \tag{1.1}$$

Point Process Models (PPMs) utilize the point process nature of a neuron's spiking activity to model the timing between spikes. The timings between spike events can be described as a stochastic point process and its probability distribution is characterized by a rate function, $\lambda(t|\cdot)$, formally known as the conditional intensity function (CIF). The CIF can be modeled as an explicit function of extrinsic and intrinsic factors, and can be estimated directly from extracellular in-vivo recordings. It is an estimation of the entire probability distribution of the spiking activity. Point process methods have been used to analyze the spike train activity for a broad range of neural systems [4, 83, 89, 107, 92]. A neural spike train can be treated as a stochastic series of random binary events (i.e., the spike times) continuously occurring in time, otherwise known as a point process [83, 107].

To define a PPM of neural spiking activity, an observation interval $(0, T]$ is considered to be the length of the spike train, and $N(t)$ is allotted to be the number of spikes counted in interval $(0, t]$ for $t \in (0, T]$. A PPM of a neural spike train is completely characterized on a given observation interval $(0, T]$ by defining the CIF [17, 102]:

$$\lambda(t|H_t) \triangleq \lim_{\Delta \to 0} \frac{\Pr(N(t+\Delta) - N(t) = 1|H_t)}{\Delta}, \tag{1.2}$$

where H_t is a vector comprising the relevant covariates at time t, and Pr the probability. It follows from (1.2) that the probability of a single spike in a small interval $(t, t+\Delta]$ is approximately $\lambda(t|H_t)\Delta$. Details can be found in [17, 102].

In this thesis, we focus on the IAF and its variations; however, as mentioned earlier in this section, it is possible to use similar analysis methods for a reduced order HH model. Moreover, the relationship between the IAF and probabilistic models as in Section 1.1.2 is provided in [84]. An abstract simplified model to describe neural activity is extremely important for fundamental analyses, and a brief discussion of the methods in the face of approximate models is given in Chapter 6.

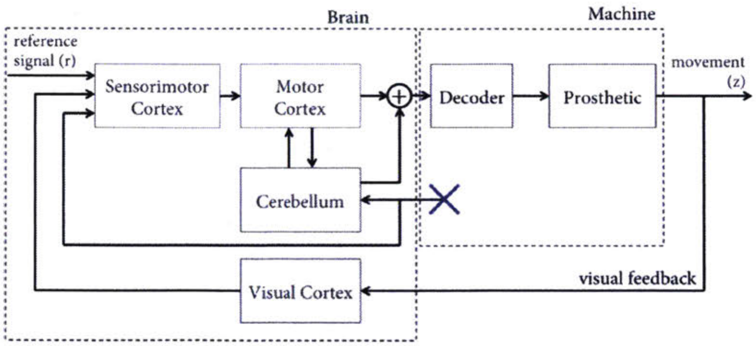

Figure 1-2: Block diagram of the severed SCS, with the 'brain' structures interacting with the 'machine' structures, including a prosthetic device driving movement. In this setting, proprioceptive feedback is usually not possible, but visual feedback is present.

1.2 Sensorimotor Control

The field of neural control of movement ranges from non-mechanistic models of movement generation at a large scale [57, 22, 112], to mechanistic models and descriptions of individual cellular structures [50, 39, 73]. These different types of models each have their own utility; however, there is little effort made to unify these in a single theory. Although this thesis focuses on using abstract models to describe movement generation, some care is taken to make sure that these models have mechanistic origins. I believe that in future studies, more care needs to be taken in order to unify detailed mechanistic models and abstract models of movement generation, and to provide a pathway from mechanistic underpinnings to phenomena predicted at a larger scale.

In this thesis, we consider two separate settings: (i) intact SCS, and (ii) severed SCS. Firstly, we examine healthy movements made with an intact SCS as shown in Figure 1-1. In this context, we analyze movement generation, and the existence of a speed cutoff; a speed such that if we try to move faster, we may not be able to accurately track desired movements. In this setting, we analyze the dependence of this speed cutoff on the musculoskeletal system as well as feedback and the neural dynamics. Secondly, we consider the severed SCS; specifically severed at the spinal cord, such as in Figure 1-2. In this setting, we assume that the neural activity is being recorded and is driving a decoder and prosthetic device in real time. In this BMI setting, we consider receiving visual feedback in the absence of proprioceptive feedback. Next, we introduce the two separate settings as well as the questions we pose in this thesis.

1.2.1 Analysis of Healthy Movements

What limits fast movements? As basic as this question may appear, it has not been rigorously tackled before. Several experimental settings have detailed that as the desired movement speed increases, we start seeing undesirable phenomena, such as overshoot, undershoot, and skipping cycles. Although current models of movement generation work well for lower movement speeds, they fail to predict these phenomena, especially the skipping of cycles. This leads us to the question - are there mechanistic ways to model movement generation that lead to these phenomena, and can we rigorously show the existence of a cutoff movement speed past which we see undesirable phenomena?

1.2.2 Brain Machine Interfaces

Building a BMI requires decoding neural activity from recorded areas of the brain in order to produce a movement signal, with the eventual goal of driving a prosthetic device. Although the recorded signals are emanating from a combination of neurons, one usually sidesteps the encoding of the signal by neurons, instead treating the structures of the brain as a combination of linear plants. Extensive research in neuroscience has provided us with basic tenets of neuronal firing, but these biophysical models have largely been ignored when building BMIs. Often, linear decoders are designed, with the firing rates of single neurons being the input to the decoder, and parameterized movement kinematics being the output [13, 99, 114]. Assuming firing rates as the output of the neuron averages out the data and incurs inherent delays in the decoding process. As we record the spikes from single neurons, can we invert the model for the generation of neural activity in real-time? Can we design this decoder in such way as to ensure the stability of the closed loop?

1.3 Thesis Objectives

Aim 1: To analyze fundamental limitations on movement speed during healthy movement generation.

This aim involves (i) building a model of movement generation that holds for the fast movement regime, while displaying known properties of motor neuron activity as well as responses to different desired movements, and (ii) performing a rigorous analysis to find the movement speed cutoff past which we see undesirable phenomena as a function of model parameters. This aim is addressed in Chapters 2 and 3.

Aim 2: To build a stabilizable, real-time decoder of neural activity to drive a prosthetic device in the closed-loop BMI setting.

This aim involves (i) the design of a tunable real-time decoder of neural spikes, with full knowledge of the encoding model, such that the reconstruction error decreases with time, and (ii) deriving conditions on the stability of the real-time decoder in the closed-loop BMI setting in order to drive desired movements of varying speeds. The real-time decoder contains a tunable parameter that governs the frequency of reconstructed signals based on the density of spiking. This aim is addressed in Chapters 4 and 5.

While the specific contributions of this thesis lie in addressing the thesis objectives outlined above, the primary contribution is to provide a way to think about movement generation using the language of the control theory community. This enables the use of sophisticated tools from control theory to address 'difficult' open problems in neuroscience. The questions addressed in this thesis have their roots in theoretical neuroscience, control theory, as well as signal processing.

Chapter 2

Model for the Neural Control of Movement

2.1 Introduction

Tracking fast unpredictable movements is a very valuable skill in many different situations. In the animal kingdom, the context includes the action of hunters chasing prey that is running and dodging at high speeds, for example, a cheetah chasing a gazelle. In the human setting, the context includes football players tackling others for the ball. The neural control of tracking unpredictable high speed movements requires substantial feedback information. Neural control of movement has been studied in the past, with feedforward and feedback models hypothesized to be activated in various settings [54, 75]. For the purposes of tracking unpredictable movements, we place ourselves in the feedback setting, while also discussing ways in which feedforward models can be incorporated in this setting.

In this chapter, we introduce a feedback model for the neural control of movement that reproduces many experimental properties of movement generation. Tracking periodic signals is an experimental paradigm that has been explored in many visuo-motor and memory tasks [37, 98]. Although tracking of movements has been well studied, with competing mathematical models to describe the phenomena observed [37], the applicability of these models in the regime of high frequency periodic movements have been overlooked. Importantly, it has been shown in experimental settings that tracking faster and faster movements leads to a regime where subjects skip cycles because they are unable to keep up. In [30], monkeys performed an oculomotor task in which they were required to track periodic inputs with their eye muscles. Tracking was shown to be reasonably accurate at low frequencies, and the frequency of the input was slowly increased. These monkeys eventually reached a limit wherein it was difficult to track the movement above a certain cutoff frequency (here termed as ω_c), and started to skip cycles (Figure 2-1A). In [108], human subjects were asked to make quick downward motions on hearing an auditory stimulus, which was periodic with varying frequency. As expected, when the frequency of the input increased, accuracy decreased. More importantly, several undesirable phenomena were observed in the high frequency regime: namely, occasional overshoot, undershoot, and skipped cycles (Figure 2-1B). In Figure 2-2, we also show example tracking for an in-house demo made using Psychtoolbox-3 [56] on MATLAB showing similar results for almost every subject we tried it on, although this was not verified rigorously. Subjects were asked to direct the cursor to track the black lines moving horizontally across the screen using the mouse by making vertical (up-and-down) movements while the cursor was horizontally constrained to the center of the screen. The horizontal black lines could be programmed to move at a variety of speeds. The lines that were not reached were subsequently colored in red while the lines that were reached with the cursor were colored in green.

Models of movement generation have not previously attempted to capture or calculate such a fundamental frequency ω_c, or to characterize movements past this frequency in the regime of fast movements. In this chapter, we formulate a quantitative biophysically-based model that reproduces these phenomena, as well as other experimental properties observed in literature and well known properties of motor neurons. Linear models describing the sensorimotor control system (SCS) components at the systems level fail to capture such undesirable tracking phenomena, while more complex biophysical models of the SCS are analytically intractable. In this chapter, we also briefly explore the shortcomings of linear models describing the sensorimotor control system (e.g. firing rates driving muscles as opposed to spikes).

In Chapter 3, we provide formal methods to compute ω_c based on the neural activity and models for the cerebrocerebellar system and the musculoskeletal system. We also show

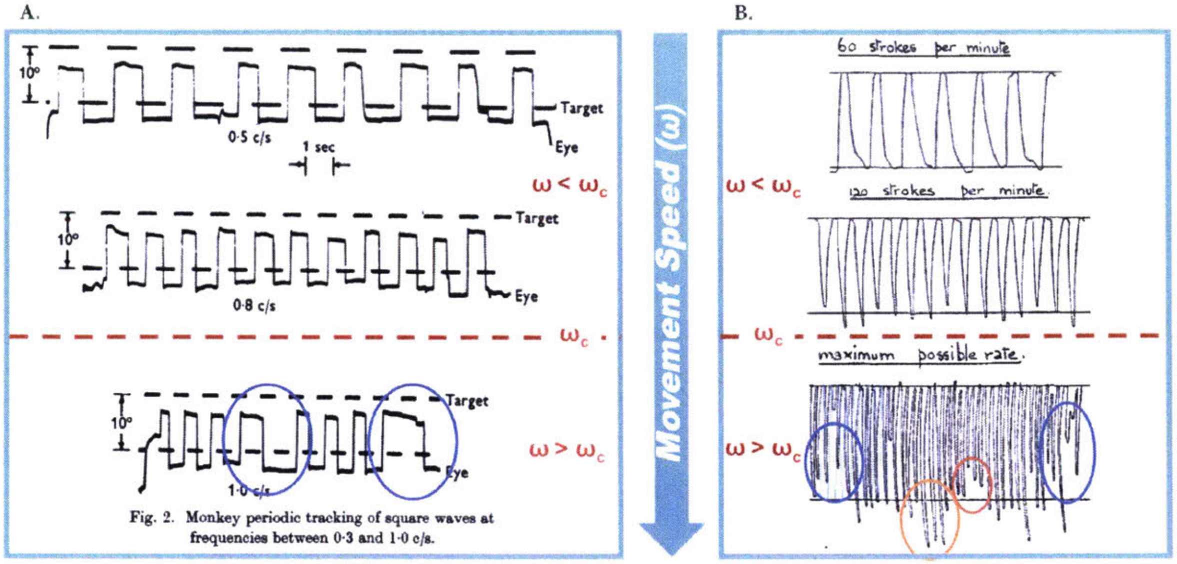

Figure 2-1: Undesirable phenomena as seen in experiments, figures adapted from A. [30] and B. [108]. In both cases, fairly accurate tracking is seen in relatively low frequency reference signals (i.e. $\omega < \omega_c$), whereas undesirable phenomena such as skipped cycles (blue circles), overshoot (orange circle) and undershoot (red circles) are seen in high frequency signals for $\omega > \omega_c$ for some ω_c.

the dependence of ω_c on parameters of the models introduced in this chapter.

We first introduce and motivate the different components of our proposed model for movement generation. Next, we present some computational results showing the reproduction of experimental properties, and importantly, the phenomena reproduced past the fundamental frequency ω_c. We finally discuss the implications of the model and the procedure for fitting it to data with available neural recordings.

2.2 Model Components

The English physiologist and Nobel Prize winner, Charles Sherrington, described the role of alpha motor neurons as the final common pathway of the motor system [109]. The upstream computations performed by the brain are converted to spiking activity by the motor neurons, that directly drive the musculoskeletal system. In this study, we model movement generation as a dynamical model for the cerebrocerebellar processing, that drives the motor neurons' spiking activity, which directly feeds into a model for the musculoskeletal

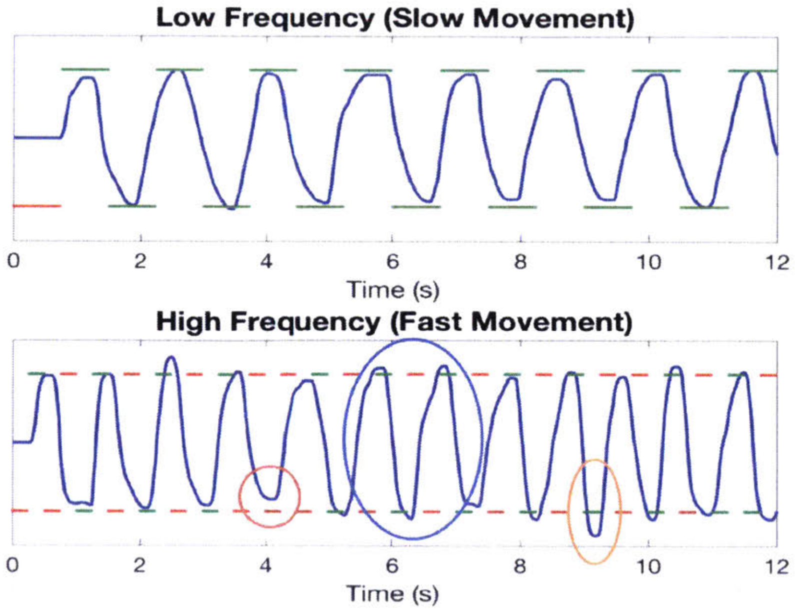

Figure 2-2: An example figure for a subject using an in-house demo built using Psychtoolbox-3 [56] on MATLAB. Demo details are provided in the main text. Briefly, subjects made periodic vertical movements to reach horizontally moving lines on the screen with their cursor. The lines that were reached by the cursor are colored in green, while those that were not reached are colored in red. Similarly to Figure 2-1, accurate tracking is seen in relatively low frequency reference signals (i.e. $\omega < \omega_c$), whereas undesirable phenomena such as skipped cycles (blue circles), overshoot (orange circle) and undershoot (red circles) are seen in high frequency signals for $\omega > \omega_c$ for some ω_c.

system, all in feedback.

Specifically, we consider a single-joint movement in closed loop, and we assume that the spike trains that are driving the musculoskeletal system can be modeled using integrate-and-fire (IAF) dynamics, as introduced in Section 1.1.1 [54]. We model the agonist and antagonist parts of the musculoskeletal system and the cerebrocerebellar feedback controller as linear time-invariant (LTI) systems, termed here M and K respectively [100]. Specific dynamical systems are shown for the purposes of this chapter, but this analysis is applicable to a wide range of LTI M and K.

Discontinuities appearing in slow movements are a well known feature that have been studied to elucidate the wiring in the downstream motor neurons. Specifically, slow movements display evidence of discontinuities in the finger position trace even while trying hard to follow a smooth trace. Following this observation, the threshold-based pulsatile control of movements was first suggested in 1947 [18], and since then has been in active exploration in the feedback setting [28, 71, 72, 77, 81, 111, 37, 24]. Most of these models differ in the details of computation before the threshold-based pulsatile movement activation (in some cases, the movement is termed ballistic; one can consider a ballistic movement as being a pulsatile output innervating a set movement plan). Here, we use a mechanistic model for movement generation that also happens to produce pulses; we use known dynamical models of neurons in conjunction with previously studied cerebrocerebellar and musculoskeletal models to come up with a specific structure for the processing of $r(t)$ that is transformed into the movement $z(t)$. It is possible, however, to use the same analysis techniques as discussed in this work for the intermittent control paradigm as discussed in the cited works.

To develop theory that provides insight into fundamental limitations of the SCS to generate fast movements, we simplify the SCS model to be parameterized by two major components (a) neural dynamics, and (b) musculoskeletal dynamics, as in Figure 2-3. Specifically, we treat the effective contribution of relevant brain structures (e.g. cerebellum, motor cortical regions) as a linear dynamical feedback controller (K) that processes errors between actual movements and intended movements. This processed error is encoded in spike trains which aggregate in the spinal cord to generate spikes in alpha motor neurons. In our SCS model, we consider two "groups" of alpha motor neurons with spiking threshold q that actuate agonist and antagonist muscles, respectively for each joint. When q is small, the density of spikes in the motor neurons is large increasing the bandwidth of the SCS. Similarly, when q is large the density of spikes is small, which decreases the bandwidth of the SCS. This simplicity of the brain and spinal cord characterizations enables tractable analysis of the SCS.

2.2.1 Neural Dynamics

We analytically study the case where the neural activity driving the muscle can be modeled by generalized IAF models. IAF models have been used to model motor neurons in both experimental and computational studies [36, 16].

A. Integrate-and-Fire Dynamics

The spikes innervate an agonist and an antagonist muscle model, as shown in Figure 5-1A. These two muscle models work in tandem to produce single joint movements. The IAF model integrates the input signal till the integral reaches a threshold q, at which time it produces a weighted spike $q\delta(t)$, as shown in Figure 5-1B. These spikes innervate the corresponding muscle model. The weight of the spike was chosen to be the same as the integral, following the Henneman's size principle [39]. In general, if we have more than one neuron innervating the muscle, the innervation amplitude should be proportional to the activation threshold in keeping with the Henneman's size principle.

B. Cerebrocerebellar System

It is well known that the cerebellum plays a critical role in processing feedback responses for maintenance of balance and posture. Also it is empirically observed that large numbers of the cerebellar cells that are involved in motor control are activated by both voluntary movement commands and passive movement of the body by an external examiner. These facts suggest that at least important parts of the sensorimotor control cerebellum lie in the forward path of a control loop that processes both feedforward and feedback control signals. It is also well established that the cerebellum operates in close association with

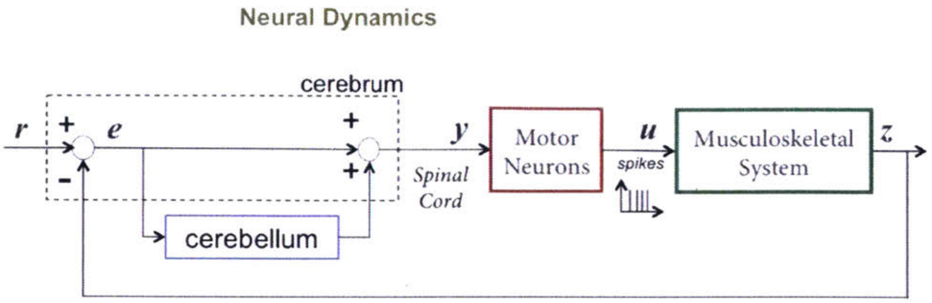

Figure 2-3: Closed loop model for movement generation at a high level. The reference movement signal r drives the SCS, which is composed of the cerebrum and cerebellum feeding into the motor neurons, which themselves drive the musculoskeletal system in feedback.

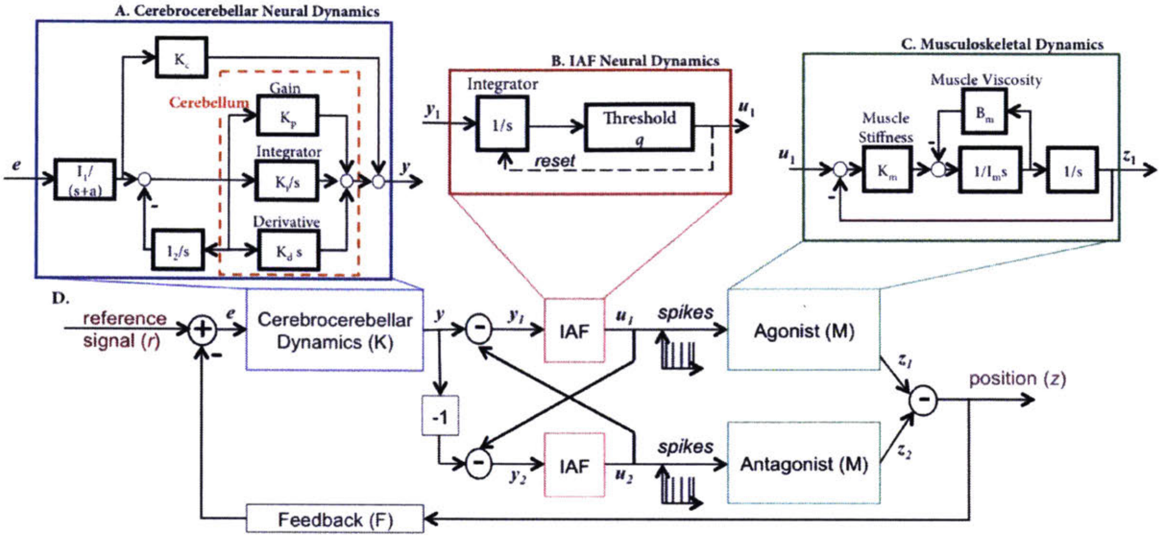

Figure 2-4: Proposed closed-loop model for movement generation. A. Details of cerebrocerebellar dynamics, adapted from [52, 51, 74]. B. Details of the IAF Model [54]. C. Details of the musculoskeletal system, adapted from [75]. D. A closed-loop model of the agonist / antagonist muscles acting around a single joint.

the cerebrum where motor commands are issued and where most likely the comparison between command and sensory signals occurs.

A basic cerebrocerebellar system diagram favored by the neuroscience community is given in Fig. 2-4A [52, 51, 74]. Thus, to begin with an analytically tractable SCS model, we propose to characterize the cerebrocerebellar SCS component as a dynamical feedback control system (K) that compares the intended movement with actual movement. Much available behavioral and neurophysiological data on human and animal cerebellar motor control relates to stabilization of posture and accurate control of movements rather than explicit control of contact force or joint torques. Importantly, though, because of the uniformity of its circuitry, intra-cerebellar mechanisms are almost certainly common to both position and force control systems, especially for fast movements. This motivates our choice of modeling the cerebrocerebellar system, K, as belonging to a class of linear time invariant systems including proportional (k_p), integral (k_I) and derivative (k_d) (PID) controllers as in [74, 105, 101, 113].

$$K(s) = k_p + \frac{k_I}{s} + k_d s \tag{2.1}$$

Our choice for K is motivated by neuroanatomical and physiological observations that have suggested strongly that an important part of cerebellar control may be PID [74, 105, 101, 113]. First, proportional scaling of signals is ubiquitous in the nervous system, and twenty years of research on the control of eye movements indicates the presence of an oculomotor "leaky" (slowly decaying) integrator associated with brainstem nuclei [69]. This work strongly indicates that the cerebellum controls the leakiness of this integrator. Other work suggests that the cerebellum balances the scaling of the proportional and integral processing of vestibular signals that are transmitted to the eye control circuits [51]. Other parts of the cerebellum are associated with positive feedback "reverberatory" circuits in the brainstem that involve the interpositus or fastigial nuclei [2]. These likely also yield integrator activity. Accordingly, damage to these areas results in a reduced ability to sustain posture against gravity or against passive elastic restoring forces due to muscles and soft tissues. From these studies, it appears that the cerebellum is intimately associated with modulating at least PI control. On the other hand, the dentate nucleus of the cerebellum and parts of the cerebellum that project to it appear to be important for enhancing the rapidity of movement onset and with suppression of target overshoot [104]. This is highly consistent with the presence of derivative action. Consistent with this is the observation that signals recorded at the dentate appear to be the derivatives of signals recorded at the interpositus.

2.2.2 Musculoskeletal Dynamics

Considerable work has been done on modeling the forward dynamics of the arm [31]. In principle, models can be very complex taking into account multiple muscles [3], their geometries of origin and insertion [3], effective moment arms [3], activation dynamics [31, 110, 115], nonlinear force-velocity relations [110, 115], skeletal mass distributions [31], and spindle behavior [47].

As this study requires analytical tractability of the SCS model, we use a simplified model of the musculoskeletal system of a single joint as in [75] (Fig. 2-4C). In this model, the muscle acts like a spring for passive displacements. This formulation is consistent with alpha-gamma coactivation that maintains the sensitivity of the muscle model to multiple

Parameter	K_c	K_p	K_i	K_d	I_1	I_2	K_a	K_m	I_m	B_m	K_f
Value	1	1	0.2	2	0.8	1	1	4	0.1	1	1

Table 2.1: Table showing the values used in this thesis for several parameters. The corresponding model is shown in Figure 2-4.

inputs; deafferented monkey experiments in which the proprioceptive feedback to the spinal cord is compromised; as well as reflex function of the limbs. As shown in Fig. 2-4C, K_M corresponds to the net stiffness of all muscles acting around the joint, as determined by the level of agonist/antagonist coactivation, B_M is the net viscosity, and I_M is the inertia.

This model is taken from the class of "equilibrium-point models" for motor control [75]. Under this class of models, the mechanical properties of muscles and the myotactic reflexes generate equilibrium positions for the limb. If the limb is displaced from rest position, the spring-like properties of the muscles generate the appropriate restoring torques to return the limb to rest (equilibrium).

These models are in reasonable agreement with experimental data, yet are simple enough to analyze. Analysis can also be carried out using Hill-type models for a single muscle [100]; however, various combinations of these Hill-type muscle models would be needed to model a single joint.

2.3 Results

We first show results for some elemental signals. We consider three signals, while briefly describing what they correspond to in a movement situation. Unless expressly mentioned otherwise, the responses correspond to model simulations with parameter values as shown in Table 2.1. Responses using the model in Section 2.2 are provided in Figure 2-5, and compared with similar movement types in [79].

1. Step Movement: A step signal corresponds to moving from one location to the other, and staying there. This paradigm has been explored at length in center-out reach tasks. Typically, the subject controls a cursor on a screen; the subject starts from the center position, moves as fast as possible, and stops the cursor within a cued

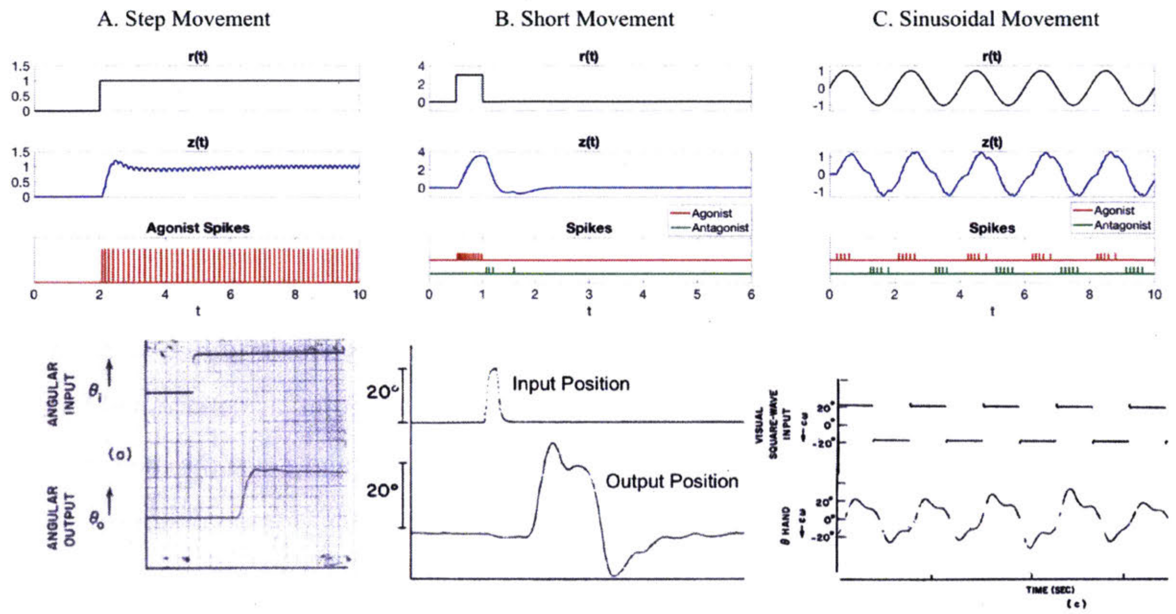

Figure 2-5: Examples of movement responses to desired movement signals as described in the text. In the top row, simulation using our model. In the bottom row, experimental data (adapted from [79]). A. Step Movement, B. Short Movement, C. Sinusoidal Movement.

target at some radial distance. This movement requires the subject to actively halt the movement. Figure 2-5A shows the response of the model to the step signal, and we can see that the response reaches the desired value after some overshoot, which is seen in experimental paradigms as well. Depending on the model parameters, there may be some oscillatory activity as well, before the desired value is reached, as in Figure 2-6C.

2. Short Movement: A short movement corresponds to moving to one location and then quickly making your way back. In an experimental setting, the subject would start from the center position, with the hand moving as fast as possible to a cued peripheral target, immediately reverse direction and return to the center, home target. This movement requires the subject to rapidly reverse the direction of motion with no stationary period. Figure 2-5B shows the response of the model to this signal, and we can see that there is some overshoot while reaching for the target, as well as on the way back.

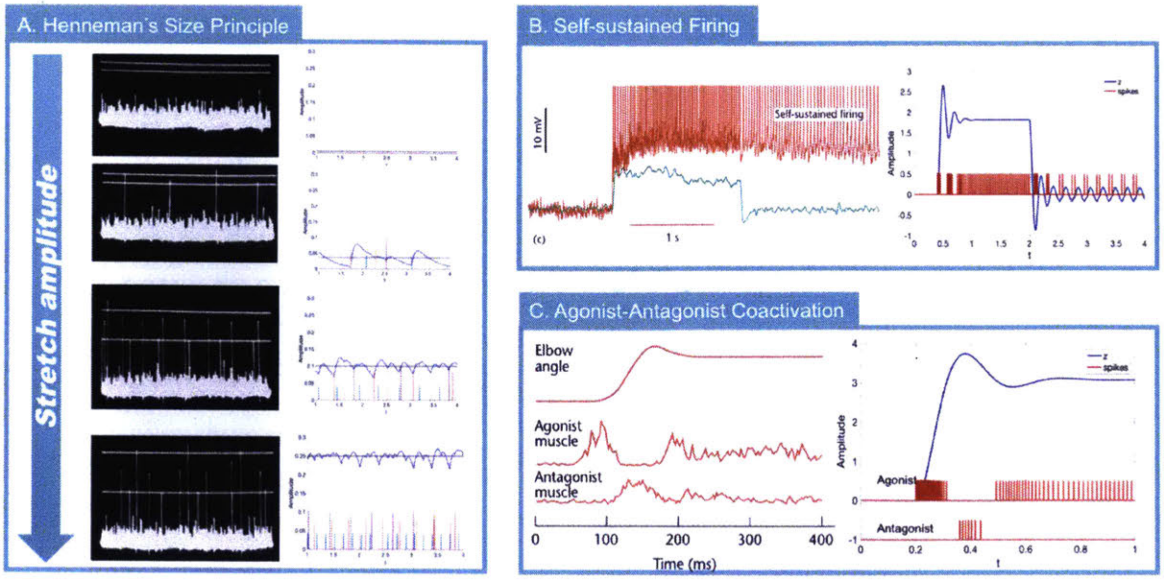

Figure 2-6: Experimental properties displayed in alpha motor neuron activity. In all these diagrams, to the left is experimental data adapted from literature, and to the right are simulations using our model. A. Henneman's principle [41], B. self-sustained oscillations [38], C. agonist-antagonist coactivation [34].

3. Sinusoidal Movement: A sinusoidal movement reference movement corresponds to a back-and-forth movement. In an experimental setting, starting from the center position the hand will move to a cued peripheral target. As the hand approaches the first target, the opposite target will illuminate, requiring the subject to move to that target. This back and forth motion will be repeated at the same tempo for some number of cycles. By varying the timing of target illumination, the subject can be required to oscillate between the targets at different frequencies. Figure 2-5C shows the response of the model to the sinusoidal signal, and we can see that the movement tracks the sinusoidal fairly well.

Our model can be shown to display several important experimental properties that motor neurons are known to follow. Alpha-motor neurons are known to display several experimental properties, including Henneman's size principle, self-sustained oscillations and agonist-antagonist coactivation [40]. A summary of these experimental properties is shown in Figure 2-6; the left portions of each panel shows experimental data, while the right portions of each panel show our model simulations.

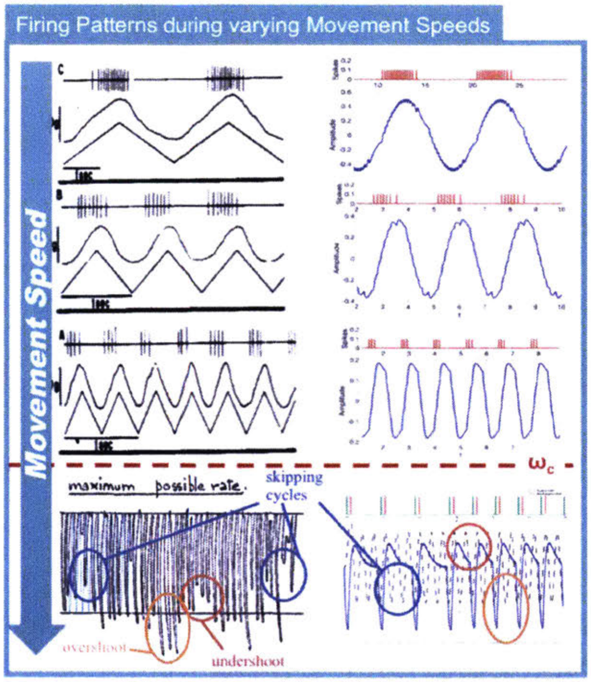

Figure 2-7: Experimental properties displayed by closed loop system for movement generation. The top three rows show the match between spiking patterns for periodic movements, adapted from [53] (Left), and our simulation results (Right). The bottom row shows data adapted from [108] (Left), and our simulation results for $\omega > \omega_c$ (Right). We see undesirable phenomena in the bottom row, for example, undershoot (red circle), overshoot (orange circle), and skipped cycles (blue circle).

- As seen in the Fig. 2-6A, the more force that is needed, the more motor units are recruited in a precise order according to the magnitude of their force output, with small units being recruited first (Henneman's size principle). Here, in order to display the accordance with the Henneman's principle, we simulated a network of neurons, with the signal y going into multiple IAF models, and the output of this network was a consolidated spike train with reweighted spikes. The weights on the consolidated spike train corresponded to the integral of y since the last spike from any IAF, which we can calculate with knowledge of the spike times from every IAF, as long as the they all have the same initial condition.

- Fig. 2-6B illustrates how motor neurons may produce plateau potentials, resulting in self-sustained firing, providing a mechanism for translating short-lasting synaptic inputs into long-lasting motor output. This self-sustained oscillatory behavior is a key property observed in more complex models of neural behavior, as described in Chapter 1.

- Fig. 2-6C shows how during the voluntary contraction of a muscle group, agonist and antagonist muscles can both be active with a specific activation pattern (agonist first, then antagonist, and then agonist again at a lower level). This concurrent activation of agonist and antagonist muscles is referred to commonly as coactivation and is captured by our model.

Finally, and most importantly, in Fig. 2-7, we show that our model is able to maintain good tracking performance of a sinusoidal input until the input frequency is larger than the bandwidth ω_c. After this input frequency, the model displays undesirable phenomena seen in experimental data. This undesirable phenomena includes the following.

- **Undershoot:** The fast movements in Figure 2-7 show that these movements may not reach the desired target.

- **Overshoot:** The fast movements in Figure 2-7 show that the movements may reach past the desired target when trying to reach a certain frequency. Both undershoot and overshoot are phenomena accompanying fast movements in general - i.e. lower accuracy while reaching for a target, and then correcting the movement when close to the target. In a repetitive movement, however, the movement is not corrected for the duration of several cycles, as seen in Figure 2-7. Note that both overshoot and undershoot are reproducible in linear systems as well.

- **Skipped cycles:** The fast movements in Figure 2-7, as well as the fast movements in Figure 2-1A clearly have skipped cycles as a feature (circled in blue). The frequency of the resulting movement is inherently changed in this paradigm. This is the most important feature observed in fast movements, since this phenomena (a) cannot be modeled using linear systems, and (b) cannot be remedied in open loop using a linear system at the output of the movement.

To our knowledge, this is the first model for movement generation that has been extended to the fast movement regime.

2.3.1 Linear Models Characterizing Movement Generation

One can assume that the transformation from the current to the firing rate of the neuronal spikes (here assumed to be the output signal of a neuron) is LTI, i.e. the firing rate output is some linear and time invariant function of the input entering the neuron. By attempting to learn the movement parameters for the cerebrocerebellar system and the musculoskeletal system from given desired and actual movement data for $\omega < \omega_c$, in the best case scenario, we would learn the LTI systems as in Sections 2.2.1.B and 2.2.2. If we simulate this linear model, we see that the response does not display overshoot or skipped cycles, even at high target frequencies. In Figure 2-8A, for low frequencies, we see that the linear response z_{linear} approximates the full, nonlinear response z adequately. As the frequency increases, the approximation of the nonlinear response with the linear response gets worse and worse. Finally, for $\omega > \omega_c$ as in Figure 2-8B, the nonlinear response displays skipped cycles, which the linear response does not display. Indeed, next we rigorously show that for any linear model, the response cannot display skipped cycles.

Using principles in linear dynamical systems, we can show that the closed loop system without the IAF nonlinearity in the loop, i.e. for $z_{linear} = \frac{M}{1+MKF}r$, and with $r(t) = R\sin(2\pi\omega t + \phi)$, the amplitude of $z_{linear}(t)$ in the steady state decreases as a function of ω for low pass M and K. The steady state has the following equation, with $G_{linear} = \frac{M}{1+MKF}$.

$$z_{linear}(t) = R|G_{linear}(j\omega)|\sin(2\pi\omega t + \phi + \angle G_{linear}(j\omega)) \tag{2.2}$$

Importantly, this linear characterization fails to reproduce the phenomena we see in experiments, i.e. the phenomena of skipped cycles. Thus the nonlinear component here described by the IAF (or some other such nonlinear component) is necessary for the existence of the specific undesirable phenomena seen in experiments.

2.4 Discussion

Humans can make flexible and fairly fast movements, however damage to various parts of the central nervous system can limit motor performance. Whether damage is caused

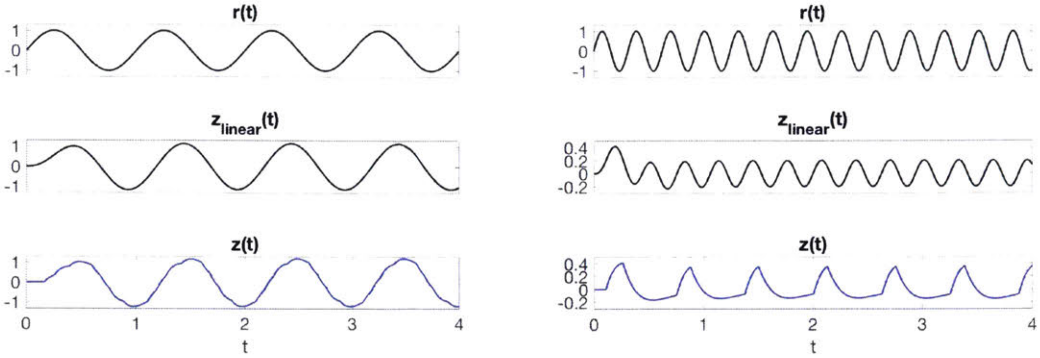

(A) $\omega = 1 < \omega_c$ (B) $\omega = 3.2 > \omega_c$

Figure 2-8: z is the response of the full, nonlinear feedback system as shown in Figure 2-4, while z_{linear} is the response of G_{linear}. The driving signal r is a sinusoid, i.e., $r = \sin(\omega t)$. The linear system assumes that the firing rates of the individual neurons are the outputs of the neuronal system. A. The desired movement r is a 'slow' movement; we see that z_{linear} approximates z. B. The desired movement r is a 'fast' movement; we see that z_{linear} does not approximate z, since z contains skipped cycles.

by stroke, multiple sclerosis, amyotrophic lateral sclerosis, or spinal cord injury, weakness (paresis) occurs routinely after injury to the primary motor cortex (M1) or its output to the spinal cord. This weakness is known to be associated with reduced voluntary recruitment of motor units in the spinal cord, both in terms of the number of motor units recruited and the firing rates they achieve. Given that weakness translates to deficient production of muscular forces that are used to accelerate the limbs, we expect weakness to limit fast movements, with progressively more reduction of neural activity being associated with a deceleration of voluntary movements. However, to the best of our knowledge, this is the first time that this relationship can be quantified in one model. The model discussed in this chapter, while primarily being a feedback control model, is amenable to the addition of a feedforward system without changing the core results. The quantification as well as the dependence of the parameters introduced in this section on ω_c will be presented in Chapter 3.

Chapter 3

Quantifying Fundamental Limitations in Movement Speed

3.1 Introduction

Periodic movements faster than a certain 'fundamental frequency' produce undesirable effects such as skipped cycles, overshoot and undershoot. These phenomena are described in more detail in Chapter 2. Moreover, a model that reproduces these phenomena in the regime of fast movements, as well as other experimental properties of motor neurons, is motivated and discussed in detail. Here, we focus on the phenomenon described till now as 'skipped cycles', that is otherwise known in nonlinear control theory as subharmonic oscillations (defined later). In this chapter, we proceed with the theoretical analysis of a feedback system containing the integrate and fire (IAF) nonlinearity, as detailed in Chapter 2, while proceeding with analysis for general linear time invariant (LTI) cerebrocerebellar K and musculoskeletal M models. Specifically, we ask two questions, (i) Does there exist a clear cutoff frequency ω_c, such that for $\omega \geq \omega_c$ we may see subharmonic oscillations, and (ii) Can we calculate ω_c as a function of the rest of the parameters of the feedback system.

In this chapter, we first derive conditions for which the movement signal includes subharmonic oscillations as a function of the parameters of the closed-loop system. We then show that as ω increases, the conditions for the occurrence of these subharmonic oscillations become easier to satisfy. Lastly, we present a method to calculate the initial conditions that will produce subharmonic oscillations given a ω, and relatedly, a method to calculate the ω_c such that for some $\omega \geq \omega_c$, we can calculate initial conditions that lead to subharmonic oscillations. It is important to note that these ideas and results apply to a large class of systems, thus can be flexibly utilized with different choices of model structures. We finally present the results for the model introduced in Chapter 2, while discussing the sensitivity of ω_c on the relevant model parameters.

3.2 Preliminaries

Linear fractional transformations (LFT) of linear systems were shown to be a powerful tool for analysis and synthesis of robust controllers [118]. On one hand, feedback interconnections are all LFTs in both the plant and controller. On the other hand, and more importantly, LFTs are powerful models for representing plant uncertainty. In order to clarify the notation used in this chapter, let G be a general LTI system that has two vector-valued inputs and two vector-valued outputs. G can then be decomposed with these two inputs and outputs as follows:

$$\begin{bmatrix} y \\ z \end{bmatrix} = \begin{bmatrix} G_{11} & G_{12} \\ G_{21} & G_{22} \end{bmatrix} \begin{bmatrix} u \\ r \end{bmatrix} \tag{3.1}$$

Now, consider the feedback interconnection defined as $u = sN_R y$ (Fig. 3-1C). Then the closed-loop mapping from r to z is given by the LFT defined as:

$$z = LFT(G, N_R)r = [G_{22} + G_{21}N_R(I - N_R G_{11})^{-1}N_R G_{12}]r \tag{3.2}$$

An interesting observation is that LFTs can be used to model very general classes of nonlinear systems, where the nonlinear part is subsumed in N_R. It can be easily verified that any nonlinearity that appears in either part of a feedforward or feedback loop of a system can be cast in this form. Therefore, one can show that our SCS model has an LFT of the form: $SCS = LFT(G, N_R)$.

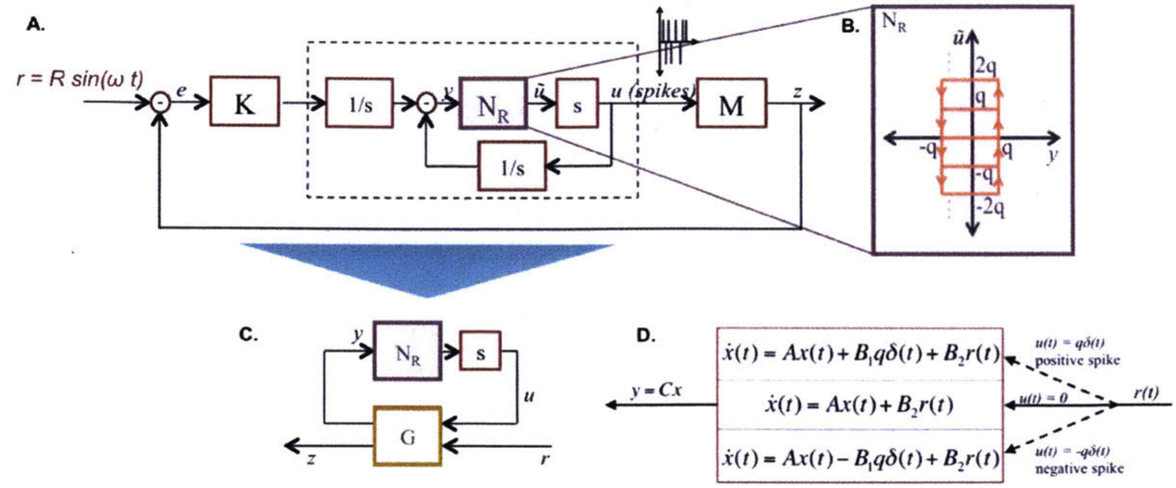

Figure 3-1: Feedback Loop considered in this study. A. The reformulation of the neurons in the feedback loop as a nonlinearity (as in B.) and the linear systems. B. The nonlinearity N_R. C. Standard nonlinear control framework separating the effect of the nonlinearity N_R from the linear system. D. Switched System, with matrices defined as in (3.9).

3.3 Problem Formulation

First, we map the feedback system shown in Fig. 3-1A to a nonlinear system, $N_R : y \rightarrow \tilde{u}$, interacting with the linear systems as shown in Fig. 3-1B. This is an exact mapping. Note that the derivative of the output of N_R is a spike train with positive and negative spikes (this realized in the actual SCS as two positive spike trains activating two different groups of motor units in the spinal cord). Then, we separate the effect of the nonlinear operator, N_R, and the derivative operator s from the rest of the interconnection, G, as shown in Fig. 3-1C. G is a 2x2 system that represents the mapping from $(u \;\; r)$ to $(y \;\; z)$. The model for G can be derived as follows. Let the following equations define the dynamics for the minimal state-space representation for the musculoskeletal system M and cerebrocerebellar system K.

$$
\begin{aligned}
M: \ \frac{d}{dt}x_M(t) &= A_M x_M(t) + B_M u(t); \quad x_M(0) = x_{M0} && (3.3)\\
y_M(t) &= C_M x_M(t) && (3.4)\\
K: \ \frac{d}{dt}x_K(t) &= A_K x_K(t) + B_K u(t); \quad x_K(0) = x_{K0} &&\\
y_K(t) &= C_K x_K(t) + D_K u(t) &&
\end{aligned}
$$

Then, the dynamics of the closed loop system can be expressed as follows:

$$
\begin{aligned}
G: \ \frac{d}{dt}x(t) &= Ax(t) + B_1 u(t) + B_2 r(t) && (3.5)\\
y(t) &= Cx(t) && (3.6)\\
x(0) &= x_0 && (3.7)\\
N_R: \ u(t) &= \begin{cases} q\delta(t) & y \geq q \\ -q\delta(t) & y \leq -q \\ 0 & -q < y < q \end{cases} && (3.8)
\end{aligned}
$$

$$
A = \begin{bmatrix} A_K & -B_K C_M & \mathbf{0} \\ \mathbf{0} & A_M & \mathbf{0} \\ -C_K & -D_K C_M & 0 \end{bmatrix}; \ B_1 = \begin{bmatrix} \mathbf{0} \\ B_M \\ -1 \end{bmatrix}; \ B_2 = \begin{bmatrix} B_K \\ \mathbf{0} \\ D_K \end{bmatrix}; \ C = \begin{bmatrix} \mathbf{0} & \mathbf{0} & 1 \end{bmatrix}; \ x_0 = \begin{bmatrix} x_{K0} \\ x_{M0} \\ \tilde{x}_0 \end{bmatrix} \tag{3.9}
$$

where $\tilde{x}_0$ is the initial condition of the IAF integrator, and **0** represents a zero matrix of the appropriate size. We say that a 'negative' or a 'positive' spike is emitted whenever $y(t)$ reaches q and $-q$, respectively, at which point $u(t)$ takes values $q\delta(t)$ and $-q\delta(t)$, respectively. See Fig. 3-1D. Note that between spikes, G operates in open loop, i.e., without any effect from the nonlinearity. We can thus formulate the feedback system as a switched system (Fig. 3-1D); where the state equation switches every time the IAF emits a spike. In our case, the SCS switches between 3 LTI systems when: (i) $y > q$, (ii) $y < -q$, and (iii) $q \leq y \leq q$, which can be analyzed in a straightforward manner with linear systems theory [118].

We study the output of the closed-loop system under periodic forcing, specifically $r(t) = R\sin(2\pi\omega t + \phi)$, and we are interested in how well $z(t)$ follows $r(t)$ as the bandwidth of the reference movement signal ω increases. We use tools in nonlinear control theory to analyze the output for different input classes; we first map the feedback system as in Fig. 3-1A as a nonlinear system $N_R : y \rightarrow u$ (Fig. 3-1B) interacting with linear systems $\{M, K\}$ as in Fig. 3-1C. This is an exact mapping.

The feedback system's state vector evolves according to the following equation.

$$x(t) = \mathrm{e}^{At}x_0 + \int_0^t \mathrm{e}^{A(t-\tau)}(B_1u(\tau) + B_2r(\tau))d\tau \tag{3.10}$$

Definition: Let $r(t) = R\sin(2\pi\omega t + \phi)$. We define the occurrence of a *subharmonic oscillation* of order k, where $k \in \mathbb{Z},\ k > 1$, as the case where there is exactly one positive spike and one negative spike per k periods of the input, i.e. there is exactly one up-crossing and one down-crossing of y within $[t, t + 2\pi k/\omega)$ for any $t \in \mathbb{R}$.

We want to find the minimum frequency past which we see a degradation in tracking in the form of subharmonic oscillations, i.e. ω_c s.t. $\forall\omega > \omega_c,\ \exists\{x_0, \phi\}$ s.t. $\int_0^{2\pi k/\omega} u(t)dt = 0$ and $\int_0^{2\pi k/\omega} |u(t)|dt = 2q$ for some $k \in \mathbb{Z},\ k > 1$. That is to say, $u(t)$ only emits one positive and one negative spike during more than one period of the input oscillation. This can be formulated using switching systems theory as $y(t)$ reaches q exactly once and $-q$ exactly once for $t \in [0, 2\pi k/\omega)$, and $|y(t)| < q$ for the rest of the time. Moreover, for this to be a valid oscillation, the state of the system needs to be the same after every $2\pi k/\omega$, i.e. $x(t + 2\pi k/\omega) = x(t)\ \forall t \in \mathbb{R}$. An example sketch is provided in Figure 3-2 to illustrate this point. This gives us the intuition for the following theoretical results.

3.4 Theoretical Results

We first provide necessary and sufficient conditions for subharmonic oscillations to exist in this system.

Theorem 1. *Consider the system as in Equations 3.5-3.8, with* $r(t) = R\sin(2\pi\omega t + \phi_r)$, *where* $\omega > 0$ *and* $R > 0$. *Assume* $(I - \mathrm{e}^{A_{MK}})$ *is invertible. Then,* $\exists\{x_0, \phi_r\}$ *such that*

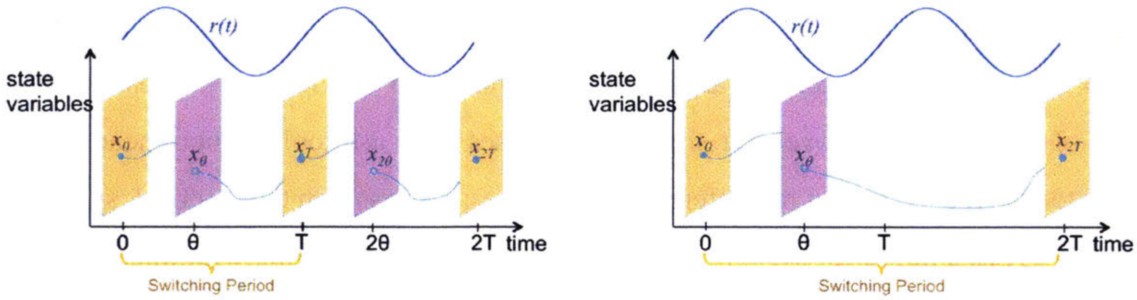

Figure 3-2: A graphical illustration of subharmonic oscillations. Here, the reference signal $r(t)$ shown in blue is a sinusoidal signal with period T. The state variables of the system $x(t)$ are represented as a two dimensional object in green. The switching planes are depicted in yellow for negative spikes and purple for positive spikes. Left: The switching period of the system is equal to the period of $r(t)$, which is the desirable case. Right: An example of subharmonics oscillations for which the switching period is double that of $r(t)$.

subharmonic oscillations occur iff $\exists k > 1,\ k \in \mathbb{Z}$ *s.t. for some* $\phi_n \in (-\pi, \pi]$, *and for some* $\theta^* \in (0, k)$, *the following is true.*

$$1 = y_n^1(\theta^*) \tag{3.11}$$

$$1 > |y_n^1(\theta)| \ \ \forall \theta \in (0, \theta^*) \tag{3.12}$$

$$1 > |y_n^2(\theta)| \ \ \forall \theta \in (\theta^*, k) \tag{3.13}$$

, *where*

$$\begin{aligned} y_n^1(\theta) &= C\mathrm{e}^{A\theta/\omega}\frac{a_n}{q} - C\mathrm{e}^{A\theta/\omega}B_1 + \frac{R_0}{2\pi\omega q}(\cos(\phi_n) - \cos(2\pi\theta + \phi_n)) \\ y_n^2(\theta) &= C\mathrm{e}^{A\theta/\omega}\frac{a_n}{q} - C(\mathrm{e}^{A\theta/\omega} - \mathrm{e}^{A(\theta-\theta^*)/\omega})B_1 + \frac{R_0}{2\pi\omega q}(\cos(\phi_n) - \cos(2\pi\theta + \phi_n)) \\ a_n &= \begin{bmatrix} (I - \mathrm{e}^{A_{MK}k/\omega})^{-1}\mathrm{e}^{A_{MK}k/\omega}(\mathrm{e}^{-A_{MK}\theta^*/\omega} - I)B_{MK}q \\ -q \end{bmatrix} \end{aligned} \tag{3.14}$$

Proof. Provided in Section 3.6. □

We also provide the following two functions; the conditions above can be restated in terms of these (as provided in Section 3.6).

$$\begin{aligned} y_p^1(\theta) &= C\mathrm{e}^{A\theta/\omega}\frac{a_p}{q} + C\mathrm{e}^{A\theta/\omega}B_1 + \frac{R_0}{2\pi\omega q}(\cos(\phi_p) - \cos(2\pi\theta + \phi_p)) \\ y_p^2(\theta) &= C\mathrm{e}^{A\theta/\omega}\frac{a_n}{q} + C(\mathrm{e}^{A\theta/\omega} - \mathrm{e}^{A(\theta-\theta^*)/\omega})B_1 + \frac{R_0}{2\pi\omega q}(\cos(\phi_p) - \cos(2\pi\theta + \phi_p)) \\ a_p &= \begin{bmatrix} (I - \mathrm{e}^{A_{MK}k/\omega})^{-1}\mathrm{e}^{A_{MK}k/\omega}(I - \mathrm{e}^{-A_{MK}\theta^*/\omega})B_{MK}q \\ q \end{bmatrix} \end{aligned} \tag{3.15}$$

With the conditions above, we can now examine the existence of subharmonic oscillations as a function of the frequency of stimulation ω. Firstly, we show that, under certain conditions, one of the key conditions (Equation 3.24) is easier to satisfy with higher ω, specifically $\max_{\theta\in(0,1)} y_n^1(\theta,\omega_2) \leq \max_{\theta\in(0,1)} y_n^1(\theta,\omega_1)$ for $\omega_2 > \omega_1$ (and similarly for y_p^1). Thus, a necessary condition for subharmonic oscillations is satisfied only for high values of ω.

Corollary 1. *Consider the system as in Equations 3.5-3.8, with* $r(t) = R\sin(2\pi\omega t + \phi_r)$, *where* $\omega > 0$ *and* $R > 0$. *If the dynamical system defined by* $ss(A, B_1, C, 0)$ *has an impulse response that is monotonic in t, i.e.* $Ce^{At_1}B_1\alpha \geq Ce^{At_2}B_1\alpha \; \forall t_1 < t_2$ *and* $\alpha > 0$, *then for a given* $\{a, \phi\}$,

$$\max_{\theta\in(0,1)} y_n^1(\theta,\omega_2) \leq \max_{\theta\in(0,1)} y_n^1(\theta,\omega_1) \quad \text{for } \omega_2 > \omega_1 \tag{3.16}$$

$$\min_{\theta\in(0,1)} y_p^1(\theta,\omega_2) \geq \min_{\theta\in(0,1)} y_p^1(\theta,\omega_1) \quad \text{for } \omega_2 > \omega_1 \tag{3.17}$$

Proof. Provided in Section 3.6. ☐

We next provide a means of calculation of $\{\omega, x_0, \phi_r\}$ where $\omega > \omega_c$ and $\{x_0, \phi_r\}$ lead to subharmonic oscillations.

Corollary 2. *Consider the system as in Equations 3.5-3.8, with* $r(t) = R\sin(2\pi\omega t + \phi_r)$. *Assume* $I - \mathrm{e}^{A_{MK}}$ *is invertible and all eigenvalues of* A_{MK} *are negative. Then, there exists a* $\omega_c > 0$ *such that for some* $\omega \geq \omega_c$, $\exists\{x_0, \phi_r\}$, *that will lead to subharmonic oscillations.*

Proof. Provided in Section 3.6. ☐

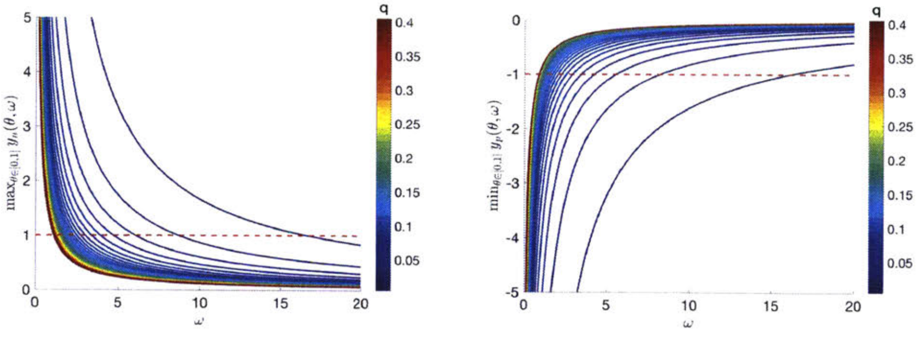

Figure 3-3: A. $\max_{\theta\in[0,1]} y_n(\theta,\omega)$ as a function of ω, with $a_n = 0$ and $\phi_n = -\frac{\pi}{2}$. B. $\min_{\theta\in[0,1]} y_p(\theta,\omega)$ as a function of ω, with $a_p = 0$ and $\phi_p = -\frac{\pi}{2}$

As an example, to show that the conditions leading to subharmonic oscillations are satisfied primarily for high values of ω, we fix a_n and ϕ_n, and in Figure 3-3A, we show the evolution of $\max_{\theta\in[0,1]} y_n^1(\theta,\omega)$; we see that this is less than 1 only for $\omega > \omega_c$ for some ω_c. Next, we fix a_p and ϕ_p, and in Figure 3-3B, we show the evolution of $\min_{\theta\in[0,1]} y_p^1(\theta,\omega)$; we see that this is greater than -1 only for $\omega > \omega_c$ for some ω_c. Thus, we see that since these conditions are not satisfied for low values of ω, there exists some cutoff frequency ω_c such that at least one of these conditions is satisfied. We can indeed calculate ω_c by taking the joint minimum of the two functions $(\max_{\theta\in[0,1]} y_n^1(\theta,\omega) - 1)$ and $(-\min_{\theta\in[0,1]} y_p^1(\theta,\omega) - 1)$ over ω.

Thus, we provide a formulation to the highest frequency after which we see subharmonic oscillations with initial conditions as given in the proof of Corollary 1. In Figure 3-4, we see ω_c as a function of q for a given value of R, M and K. In general, ω_c as q increases, i.e., as the spikes become sparser, the fastest movement possible is decreased. In Figure 3-5, we see the effect of varying various model parameters on ω_c. This shows that as the feedback gain becomes higher, and as the bandwidth of M becomes higher, we have higher maximum speeds.

3.4.1 Results for $K = 1$

We consider a musculoskeletal model as motivated in Section 2.2.2, with $M(s) = \frac{p}{0.1s^2+1.78s+p}$. We first consider $K = 1$, and show results for ω_c as a function of q, for

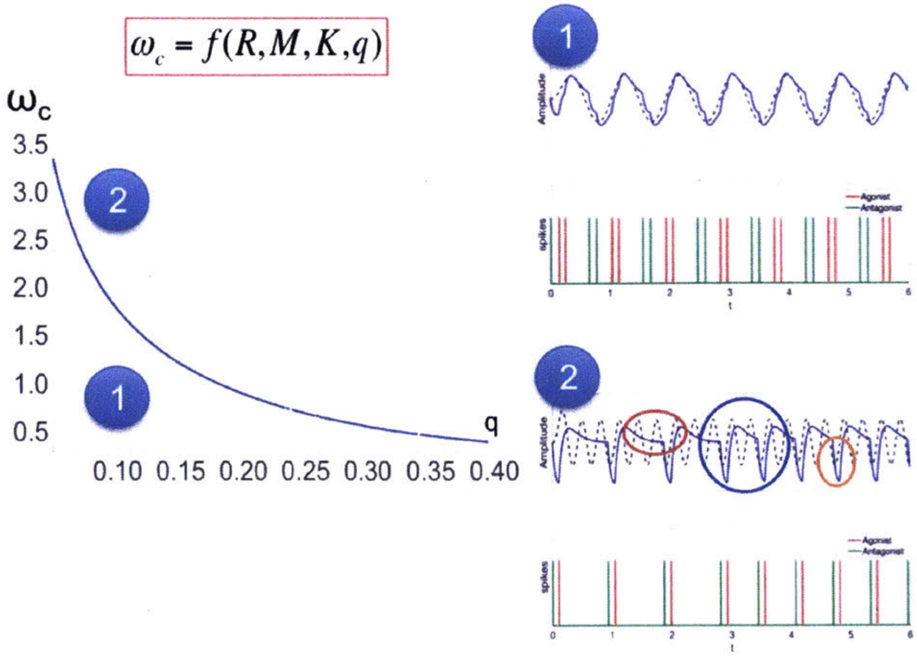

Figure 3-4: Undesirable subharmonic oscillations with a sinusoidal excitation. Left: ω_c for varying q. Top Right: $q = 0.1$, $\omega = 1$, $\phi = 0$, $x_0 = [0\ 0\ -0.1]'$. Bottom Right: $q = 0.1$, $\omega = 3.18$, $\phi = 0$, $x_0 = [0\ 0\ -0.1]'$. Here, $R = 1$, $K = 1$, $F = 1$, $M(s) = \frac{4}{0.1s^2+1.78s+4}$.

$R = 1$, and $F = f$, while varying p and f. In Fig. 3-4, we see that as q increases, the maximum bandwidth ω_c decreases. Moreover, we see in Figure 3-5 that as the feedback gain or as the bandwidth of the musculoskeletal system increases, we have a higher ω_c for all values of q.

3.4.2 Results for K as in Section 2.2.1

Next, we show the results for neural dynamics in full generality as described in Chapter 2, specifically, implementing the cerebrocerebellar model as in Section 2.2.1.These results are shown in Figure 3-6. We see that as the feedback gain or as the bandwidth of the musculoskeletal system increases, we have a higher ω_c for all values of q, as is also true for $K = 1$. Moreover, as the cerebellar proportional gain (K_p) increases, ω_c increases, but not to a large extent. However, as the cerebellar derivative gain (K_d) increases, ω_c increases drastically, showing the large degree of sensitivity to K_d. The derivative action is hypothesized to take place in the dentate neurons of the cerebellum [51], which are known

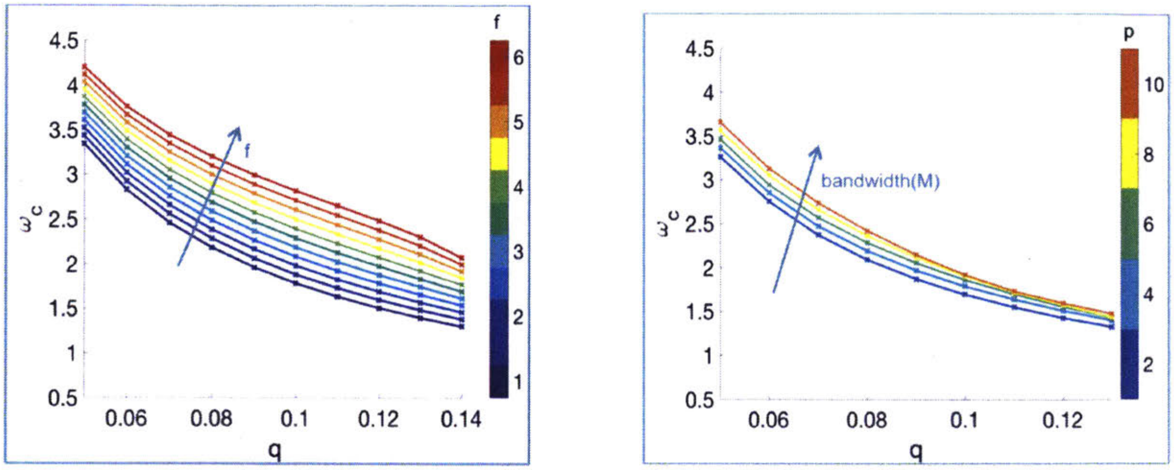

Figure 3-5: ω_c for $R = 1$, $M(s) = \frac{p}{0.1s^2+1.78s+p}$, $K = 1$, $F = f$. Left: ω_c for varying q and f, with $p = 4$. Right: ω_c for varying q and p, with $f = 1$.

to be hypothesized to be important for rapidly implementing a desired action [87, 104]. This feature is corroborated in Figure 3-6D.

3.5 Discussion

The formulation described above provides us an explicit dependence of the emergence of undesirable phenomena on q, the parameter that directly dictates the density of spikes. Specifically, we show that for a fixed musculoskeletal system M, cerebrocerebellar dynamics K, and a pair of motor neurons with thresholds q (for activation of agonist/antagonist pair of muscles), the oscillation input (periodic back-and-forth movement) with frequency ω may generate undesired subharmonics if ω is 'too large' and/or the density of spikes (related to q) is 'too small'. Such undesirable phenomena are consistent with symptoms observed in patients with movement disorders, and finger tracking experiments wherein subjects are trained to follow a trace back and forth quickly.

These undesirable phenomena have been reported in various experimental studies. In [108], also shown in Figure 2-1, we see evidence of subharmonic oscillations as well as overshoot and undershoot. In [30], we see evidence of skipped cycles in oculomotor tracking in apes. Pulsatile control of movement has provided us with insights in the 'slow' movement regime, but has rarely been analyzed for limitations in tracking 'fast' move-

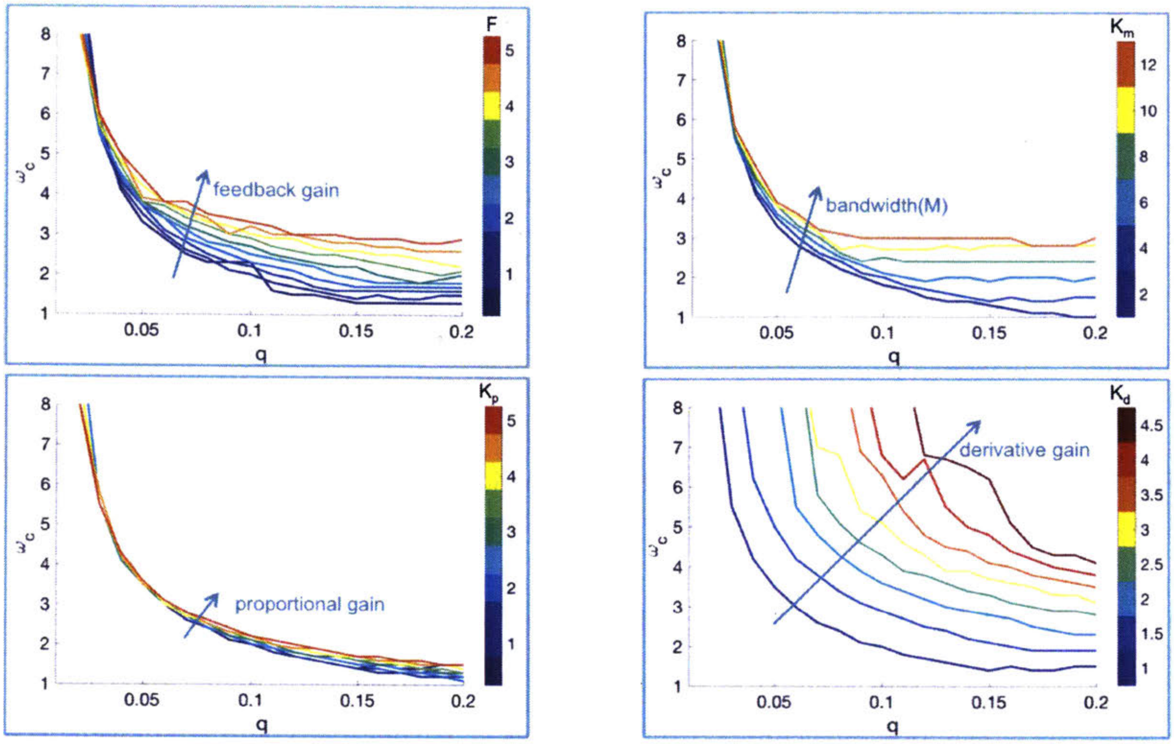

Figure 3-6: ω_c for $R = 1$, $F = f$, M as in 2.2.2, K as in 2.2.1. In all the plots, the default parameters are as in Chapter 2, unless explicitly mentioned.

ments. The processing of the reference signal $r(t)$ leading to the threshold-based condition has been conjectured as various functions of the error $e(t)$, all producing a pulsatile behavior [37]. However, these conjectured models do not have a basis in the mechanistic transfer of neural signals. The proposed model can reproduce experimentally known properties of motor neurons. However, other threshold-based pulsatile models for neural control can be readily applied to the theory developed here.

With a time varying threshold for each neuron, i.e. threshold for spike i is q_i, the presence of undesirable phenomena would be restricted to a temporary setting. However, skipped cycles would still be possible with certain initial conditions, and the maximum threshold would be the relevant parameter, i.e. similar conditions for skipped cycles would apply as for subharmonic oscillations in this chapter, while replacing q with $\max_i q_i$.

Although this study focuses on a pair of neurons driving an agonist and antagonist muscle, we believe that this phenomenon holds at the brain level as well. Although the mechanism of translating this study of a limitation due to alpha motor neuron spiking into

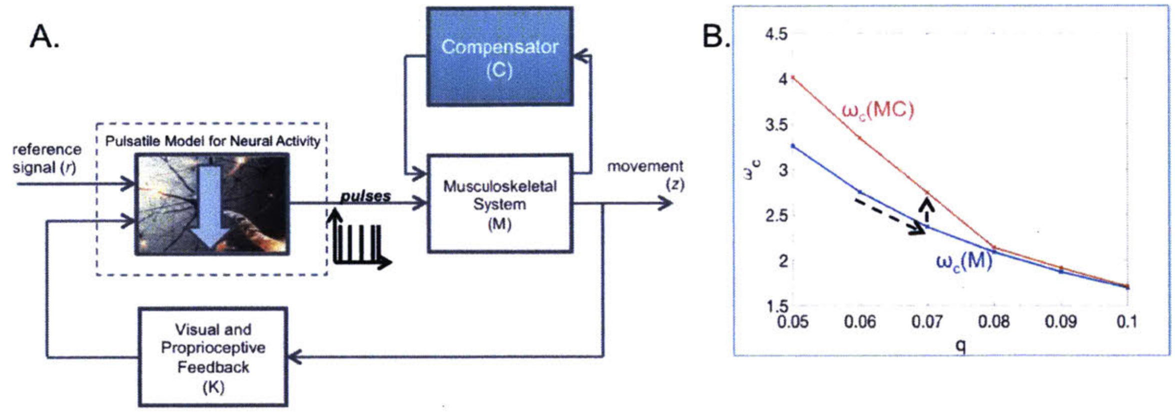

Figure 3-7: Design of a compensator to restore functioning of the SCS in the presence of a compromised neural system; more details in the text.

a limitation due to the M1 neurons is challenging due to a lack of unified mechanistic models for the relevant brain structures, these same principles can be applied using an appropriate model for these neuronal structures. Indeed, the pulsatile control of movements as discussed in [28, 71, 72, 77, 81, 111, 37, 24] all have a threshold nonlinearity at heart, which is the driver for the undesirable phenomena in the fast movement regime.

The formulation in this paper *quantifies* the increase in maximum speed gained due to the system parameters. It can also help us compensate in limbs by providing either electrical stimulation directly to the muscles, or using an exoskeletal device that can provide extra assistance to the limb. An example of these ideas is presented in Figure 3-7. Here, the block for neural activity contains the cerebrocerebellar model as well as the IAF block with the threshold parameter q as earlier. Let ω_c as a function of q for the normal regime be given by the blue curve in Figure 3-7B, and let the neural activity be compromised such that q increases (this could correspond to a damage directly in the alpha motor neurons or the spine). In this case, the operating value for ω_c would decrease as well. If we add a compensator as in Figure 3-7A, which takes in the output of the musculoskeletal system, and directly stimulates the musculoskeletal system in feedback (here, $C = 10$), and the output of the musculoskeletal system is also driven up by the same amount, i.e. $z_{new} = 10z$, then we can drive up the operating curve to the red curve shown in Figure 3-7B. This shows us that it is possible to compensate for damage to the neural system using a reinforcements at the musculoskeletal end. Moreover, the framework allows us to quantitatively design the compensator C given the neural and musculoskeletal parameters, i.e. K, q, F, and M.

3.6 Proofs for Chapter 3

This section contains the proofs for Chapter 3. For readability, the theorems are also rewritten.

Theorem 1. *Consider the system as in Equations 3.5-3.8, with* $r(t) = R\sin(2\pi\omega t + \phi_r)$, *where* $\omega > 0$ *and* $R > 0$. *Assume* $(I - \mathrm{e}^{A_{MK}})$ *is invertible. Then,* $\exists\{x_0, \phi_r\}$ *such that subharmonic oscillations occur iff* $\exists k > 1,\ k \in \mathbb{Z}$ *s.t. for some* $\phi_n \in (-\pi, \pi]$, *and for some* $\theta^* \in (0, k)$, *the following is true.*

$$\begin{aligned} 1 &= y_n^1(\theta^*) && (3.18)\\ 1 &> |y_n^1(\theta)|\ \forall\theta \in (0, \theta^*) && (3.19)\\ 1 &> |y_n^2(\theta)|\ \forall\theta \in (\theta^*, k) && (3.20) \end{aligned}$$

, *where*

$$\begin{aligned} y_n^1(\theta) &= C\mathrm{e}^{A\theta/\omega}\frac{a_n}{q} - C\mathrm{e}^{A\theta/\omega}B_1 + \frac{R_0}{2\pi\omega q}(\cos(\phi_n) - \cos(2\pi\theta + \phi_n))\\ y_n^2(\theta) &= C\mathrm{e}^{A\theta/\omega}\frac{a_n}{q} - C(\mathrm{e}^{A\theta/\omega} - \mathrm{e}^{A(\theta-\theta^*)/\omega})B_1 + \frac{R_0}{2\pi\omega q}(\cos(\phi_n) - \cos(2\pi\theta + \phi_n))\\ a_n &= \begin{bmatrix} (I - \mathrm{e}^{A_{MK}k/\omega})^{-1}\mathrm{e}^{A_{MK}k/\omega}(\mathrm{e}^{-A_{MK}\theta^*/\omega} - I)B_{MK}q \\ -q \end{bmatrix} \qquad (3.21) \end{aligned}$$

Proof. Assume that an asymmetric subharmonic oscillation exists. We let $a_n = [a_{MK}; -q]$ be the state of the system at a negative spike, i.e. a down-crossing of y, and ϕ_n the offset of $r(t)$ at the time of the negative spike. Given Equation 3.5-3.8, we can express the condition that the state returns to a_n after k periods, as the following.

$$a_n = \mathrm{e}^{Ak/\omega}(a_n - B_1q) + \mathrm{e}^{A(k-\theta^*)/\omega}B_1q \qquad (3.22)$$

Given Equations 3.9, this simplifies to Equation 3.21 as a constraint for a_n, under the condition that $I - \mathrm{e}^{A_{MK}}$ is invertible (which implies that $I - \mathrm{e}^{A_{MK}k/\omega}$ is also invertible).

Given the state evolution as in Equation 3.10, we can now express the condition that a positive spike, i.e. an up-crossing of y occurs at θ^*/ω, as $Cx(\theta^*/\omega) = q$, which simplifies to Equation 3.23.

Equations 3.24 and 3.25 represent conditions that there are strictly 2 spikes per k periods of the reference signal.

The resulting a_{MK} and ϕ define the initial conditions that will lead to subharmonic oscillations, i.e. if $x_0 = \begin{bmatrix} a_{MK} \\ -q \end{bmatrix}$ and $\phi_r = \phi_n$, the system will display subharmonic oscillations of order k.

Similarly, the conditions can also be stated in terms of the first spike being positive, as the following. Note that these are equivalent conditions for subharmonic oscillations.

We can find $\{x_0, \phi_r\}$ such that subharmonic oscillations occur iff $\exists k > 1,\ k \in \mathbb{Z}$ s.t. for some $\phi_p \in (-\pi, \pi]$, and for some $\theta^* \in (0, k)$,

$$\begin{aligned} -1 &= y_p^1(\theta^*) && (3.23) \\ 1 &> |y_p^1(\theta)|\ \forall \theta \in (0, \theta^*) && (3.24) \\ 1 &> |y_p^2(\theta)|\ \forall \theta \in (\theta^*, k) && (3.25) \end{aligned}$$

, where

$$\begin{aligned} y_p^1(\theta) &= C\mathrm{e}^{A\theta/\omega}\frac{a_p}{q} + C\mathrm{e}^{A\theta/\omega}B_1 + \frac{R_0}{2\pi\omega q}(\cos(\phi_p) - \cos(2\pi\theta + \phi_p)) \\ y_p^2(\theta) &= C\mathrm{e}^{A\theta/\omega}\frac{a_n}{q} + C(\mathrm{e}^{A\theta/\omega} - \mathrm{e}^{A(\theta-\theta^*)/\omega})B_1 + \frac{R_0}{2\pi\omega q}(\cos(\phi_p) - \cos(2\pi\theta + \phi_p)) \\ a_p &= \begin{bmatrix} (I - \mathrm{e}^{A_{MK}k/\omega})^{-1}\mathrm{e}^{A_{MK}k/\omega}(I - \mathrm{e}^{-A_{MK}\theta^*/\omega})B_{MK}q \\ q \end{bmatrix} && (3.26) \end{aligned}$$

□

Corollary 1. *Consider the system as in Equations 3.5-3.8, with* $r(t) = R\sin(2\pi\omega t + \phi_r)$, *where* $\omega > 0$ *and* $R > 0$. *If the dynamical system defined by* $ss(A, B_1, C, 0)$ *has an impulse* *response that is monotonic in t, i.e.* $Ce^{At_1}B_1\alpha \geq Ce^{At_2}B_1\alpha\ \forall t_1 < t_2$ *and* $\alpha > 0$, *then for a given* $\{a, \phi\}$,

$$\max_{\theta\in(0,1)} y_n^1(\theta,\omega_2) \leq \max_{\theta\in(0,1)} y_n^1(\theta,\omega_1) \quad \text{for } \omega_2 > \omega_1 \tag{3.27}$$

$$\min_{\theta\in(0,1)} y_p^1(\theta,\omega_2) \geq \min_{\theta\in(0,1)} y_p^1(\theta,\omega_1) \quad \text{for } \omega_2 > \omega_1 \tag{3.28}$$

Proof. There are two possibilities for subharmonic oscillations, namely, the system starts with a negative spike and misses the first peak, or the system starts with a positive spike and misses the first trough. We will consider these two possibilities separately.

Negative Spike. Let a_n and ϕ_n be the initial condition and the phase offset in question, with $a_n = \begin{bmatrix} a_1 \\ -q \end{bmatrix}$. Let $A = VDV^{-1}$, where D is the diagonal matrix of eigenvalues and V a full matrix whose columns are the corresponding eigenvectors. A necessary condition for subharmonic oscillations is $y_1(\theta) < q$, where $y_1(\theta) = Ce^{A\theta/\omega}(a_n - B_1 q) + CRV\left(\int_0^{\theta/\omega} e^{D(\theta/\omega-\tau)}\sin(2\pi\omega\tau + \phi_n)d\tau\right)V^{-1}B_1$. Since the impulse response is monotonic in t, this can be bounded from above for $a_n - B_1q < 0$, by the following.

$$y_1^{max} = Ce^{A/\omega}(a_n - B_1 q) + CRV\tilde{D}V^{-1}B_1 \tag{3.29}$$

, where $\tilde{D}$ is a diagonal matrix with the following as its i^{th} entry.

$$\tilde{D}_{ii} = \frac{2\pi\omega(e^{\theta\lambda_i/\omega}\cos(\phi_n) - \cos(2\pi\theta + \phi_n)) + \lambda_i(e^{\theta\lambda_i/\omega}\sin(\phi_n) - \sin(2\pi\theta + \phi_n))}{\lambda_i^2 + 4\pi^2\omega^2} \tag{3.30}$$

Here, λ_i is the corresponding eigenvalue of A. $\tilde{D}_{ii}$ can be bounded from above by the following.

$$\frac{2\pi\omega(1 + \cos(\phi_n)) - \lambda_i(1 - \sin(\phi_n))}{\lambda_i^2 + 4\pi^2\omega^2} \tag{3.31}$$

, which evolves as $\frac{1}{2\pi\omega}(1+\cos(\phi_n))$ for large ω. Moreover, $Ce^{A/\omega}(a_n - B_1q)$ for $a_n - B_1 q < 0$ monotonically decreases in ω due to the assumptions on the impulse response. Thus, y_1^{max}

decreases as ω increases, and one of the necessary conditions becomes easier to satisfy as ω increases.

Positive Spike. Let a_p and ϕ_p be the initial condition and the phase offset in question, with $a_n = \begin{bmatrix} a_1 \\ -q \end{bmatrix}$. Let $A = VDV^{-1}$, where D is the diagonal matrix of eigenvalues and V a full matrix whose columns are the corresponding eigenvectors. A necessary condition for subharmonic oscillations is $y_2(\theta) > -q$, where $y_2(\theta) = Ce^{A\theta/\omega}(a_p + B_1 q) + CRV\left(\int_0^{\theta/\omega} e^{D(\theta/\omega - \tau)} \sin(2\pi\omega\tau + \phi_p) d\tau\right) V^{-1} B_1$. Since the impulse response is monotonic in t, this can be bounded from below for $a_p + B_1 q > 0$, by the following.

$$y_2^{min} = Ce^{A/\omega}(a_p + B_1 q) + CRV\tilde{D}V^{-1}B_1 \tag{3.32}$$

, where $\tilde{D}$ is a diagonal matrix with the following as its i^{th} entry.

$$\tilde{D}_{ii} = \frac{2\pi\omega(e^{\theta\lambda_i/\omega}\cos(\phi_p) - \cos(2\pi\theta + \phi_p)) + \lambda_i(e^{\theta\lambda_i/\omega}\sin(\phi_p) - \sin(2\pi\theta + \phi_p))}{\lambda_i^2 + 4\pi^2\omega^2} \tag{3.33}$$

Here, λ_i is the corresponding eigenvalue of A. $\tilde{D}_{ii}$ can be bounded from below by the following.

$$\frac{-2\pi\omega(1 - e^{\lambda_i/\omega}\cos(\phi_p)) + \lambda_i(1 + e^{\lambda_i/\omega}\sin(\phi_p))}{\lambda_i^2 + 4\pi^2\omega^2} \tag{3.34}$$

, which evolves as $\frac{1}{2\pi\omega}(-(1 - \cos(\phi_p)))$ for large ω. Moreover, $Ce^{A/\omega}(a_p + B_1 q)$ for $a_p + B_1 q > 0$ monotonically increases in ω due to the assumptions on the impulse response. Thus, y_2^{min} increases as ω increases, and one of the necessary conditions becomes easier to satisfy as ω increases. □

Corollary 2. *Consider the system as in Equations 3.5-3.8, with* $r(t) = R\sin(2\pi\omega t + \phi_r)$. *Assume* $I - \mathrm{e}^{A_{MK}}$ *is invertible and all eigenvalues of* A_{MK} *are negative. Then, there exists a* $\omega_c > 0$ *such that for some* $\omega \geq \omega_c$, $\exists\{x_0, \phi_r\}$, *that will lead to subharmonic oscillations.*

Proof. Let $k = 2$, and let n be the order of MK, i.e. A_{MK} is an $n \times n$ matrix, B_{MK} is $n \times 1$, C_{MK} is $1 \times n$. We first let $a = [a_{MK}; -q]$ be the state of the system at a negative spike, and define a^*_{MK} as an initial condition that will lead to subharmonic oscillations. We find a^*_{MK} as a function of θ^*. If $I - \mathrm{e}^{A_{MK}}$ is invertible, so is $I - \mathrm{e}^{A_{MK}k/\omega}$. Thus, using Equation 3.21,

$$a^*_{MK}(\theta^*) = (I - \mathrm{e}^{A_{MK}k/\omega})^{-1}\mathrm{e}^{A_{MK}k/\omega}(\mathrm{e}^{-A_{MK}\theta^*/\omega} - I)B_{MK}q \tag{3.35}$$

Note that θ^* is unknown. $\phi^*(\theta^*)$ is found in the same way, using Equation 3.23; it is the solution to the following equation.

$$1 = \Phi^{\theta^*}_{21}(a^*_{MK}/q - B_{MK}) + \frac{R_0}{q\omega\pi}\sin(\pi\theta^*)\sin(\pi\theta^* + \phi^*) \tag{3.36}$$

Here, $\Phi^{\theta^*}_{21}$ is the $1 \times n$ vector comprising of the lower left hand side entries of $\mathrm{e}^{A\theta^*/\omega}$. In the case where $n = 1$, $\Phi^{\theta^*}_{21} = C_{MK}\left(\frac{1-\mathrm{e}^{A_{MK}\theta^*/\omega}}{A_{MK}}\right)$. Thus, the following holds under the condition that $|p| \leq 1$.

$$\phi^*(\theta^*) = 2\pi k' - \pi\theta^* + \sin^{-1}(p), \quad k' \in \mathcal{Z} \tag{3.37}$$

, where $p = \frac{(q - \Phi^{\theta^*}_{21}(a^*_{MK} - B_{MK}q))\omega\pi}{R_0 \sin(\pi\theta^*)}$.

We now want to find θ^* such that Equations 3.24 and 3.25 are satisfied. We first introduce the following.

$$\begin{aligned}
y_1^{min}(\theta, a^*_{MK}(\theta^*), \phi^*(\theta^*)) &= \Phi^{\theta}_{21}(a^*_{MK}/q - B_{MK}) + \frac{R_0}{2\pi\omega q}(\cos(\phi^*) - 1) \\
y_1^{max}(\theta, a^*_{MK}(\theta^*), \phi^*(\theta^*)) &= \Phi^{\theta}_{21}(a^*_{MK}/q - B_{MK}) + \frac{R_0}{2\pi\omega q}(\cos(\phi^*) + 1) \\
y_2^{min}(\theta, a^*_{MK}(\theta^*), \phi^*(\theta^*)) &= (\Phi^{\theta}_{21}\mathrm{e}^{-A_{MK}\theta^*/\omega} + \Phi^{-\theta^*}_{21})(a^*_{MK}/q - B_{MK}) \\
&\quad + \frac{R_0}{2\pi\omega q}(\cos(\phi^*) - 1) \\
y_2^{max}(\theta, a^*_{MK}(\theta^*), \phi^*(\theta^*)) &= (\Phi^{\theta}_{21}\mathrm{e}^{-A_{MK}\theta^*/\omega} + \Phi^{-\theta^*}_{21})(a^*_{MK}/q - B_{MK}) \\
&\quad + \frac{R_0}{2\pi\omega q}(\cos(\phi^*) + 1)
\end{aligned}$$

In the following, we drop all dependence on a^*_{MK} and ϕ^*, and just keep the dependence on θ^*. Note that $y_1^{min}(\theta, \theta^*) \leq y_1(\theta, \theta^*) \leq y_1^{max}(\theta, \theta^*)$ and $y_2^{min}(\theta, \theta^*) \leq y_2(\theta, \theta^*) \leq y_2^{max}(\theta, \theta^*)$.

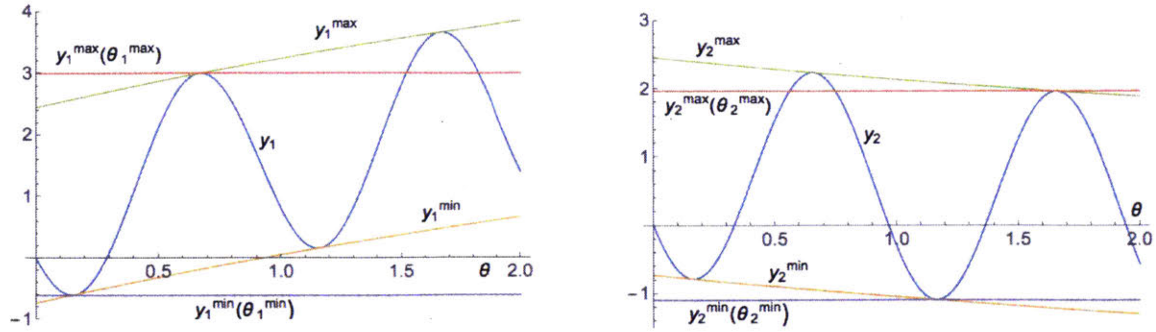

Figure 3-8: A. y_1, $\theta^* > 1$; B. y_2, $\theta^* \leq 1$.

We consider the two cases, (1) $\theta^* > 1$, and (2) $\theta^* \leq 1$, separately.

(1) $\theta^* > 1$: We need to ensure that $y_1^{min}(\theta, \theta^*) > -1$ and $y_1^{max}(\theta, \theta^*) < 1, \forall \theta \in [0, 1)$. We approximate $\theta_1^{min} = \arg\min_{\theta \in [0,1)} y_1^{min}(\theta, \theta^*)$ and $\theta_1^{max} = \arg\max_{\theta \in [0,1)} y_1^{max}(\theta, \theta^*)$, by setting $\frac{dy_1(\theta,\theta^*)}{d\theta} = 0$, and approximating $e^{A_{MK}\theta/\omega} \approx I$. This is a function of θ^*. We get an estimate of $\theta_{1,estimate}^{max} \geq \theta_{1,true}^{max}$ for $A_{MK} < 0$, which means that $y_1^{max}(\theta_{1,true}^{max}, \theta^*) \leq y_1^{max}(\theta_{1,estimate}^{max}, \theta^*)$; thus if $y_1^{max}(\theta_{1,estimate}^{max}, \theta^*) < 1$, then $y_1^{max}(\theta_{1,true}^{max}, \theta^*) < 1$. Similarly, $\theta_{1,estimate}^{min} \leq \theta_{1,true}^{min}$, which means that $y_1^{min}(\theta_{1,true}^{min}, \theta^*) \geq y_1^{min}(\theta_{1,estimate}^{min}, \theta^*)$; thus if $y_1^{min}(\theta_{1,estimate}^{min}, \theta^*) > -1$, then $y_1^{min}(\theta_{1,true}^{min}, \theta^*) > -1$. From now onwards, we characterize

$y_1^{max}(\theta_{1,estimate}^{max}(\theta^*), \theta^*)$ as $y_1^{max}(\theta^*)$, and similarly $y_1^{min}(\theta_{1,estimate}^{min}(\theta^*), \theta^*)$ as $y_1^{min}(\theta^*)$. We can now compute $\min_{\{1<\theta^*<2\}}(y_1^{min}(\theta^*))$, and if this quantity > -1, we will have subharmonic oscillations. This can also be written as the following.

$$\omega_1^* = \min \omega \; s.t. \; y_1^{min}(\theta^*) > -1, \;\; \forall \theta^* \in [1, 2) \tag{3.38}$$

To find the initial conditions that lead to these subharmonic oscillations, we plug in $\theta_1^* = \arg\min_{\{1<\theta^*<2\}}(y_1^{max}(\theta^*))$ into Equations 3.35 and 3.37.

(2) $\theta^* \leq 1$: We need to ensure that $y_2^{min}(\theta, \theta^*) > -1$ and $y_2^{max}(\theta, \theta^*) < 1, \forall \theta \in [1, 2)$. We approximate $\theta_2^{min} = \arg\min_{\theta \in [1,2)} y_2^{min}(\theta, \theta^*)$ and $\theta_2^{max} = arg\max_{\theta \in [1,2)} y_2^{max}(\theta, \theta^*)$, by setting $\frac{dy_2(\theta,\theta^*)}{d\theta} = 0$, and approximating $e^{A_{MK}\theta/\omega} \approx I$. This is a function of θ^*. We get an estimate of $\theta_{2,estimate}^{max} \geq \theta_{2,true}^{min}$, which means that $y_2^{min}(\theta_{2,true}^{min}, \theta^*) \geq y_2^{min}(\theta_{2,estimate}^{min}, \theta^*)$; thus if $y_2^{min}(\theta_{2,estimate}^{min}, \theta^*) > -1$, then $y_2^{min}(\theta_{2,true}^{min}, \theta^*) > -1$. Similarly for y_2^{max}. From now onwards, we characterize $y_2^{min}(\theta_{2,estimate}^{min}(\theta^*), \theta^*)$ as $y_2^{min}(\theta^*)$, and similarly, we characterize $y_2^{max}(\theta_{2,estimate}^{max}(\theta^*), \theta^*)$ as $y_2^{max}(\theta^*)$.

We can now compute $\max_{\{0<\theta^*<1\}}(y_2^{max}(\theta^*))$, and if this quantity is < 1, we will have subharmonic oscillations. This can also be written as the following.

$$\omega_2^* = \min \omega \; s.t. \; y_2^{max}(\theta^*) < 1, \;\; \forall \theta^* \in [0,1) \tag{3.39}$$

To find the initial conditions that lead to these subharmonic oscillations, we plug in $\theta_2^* = \arg\max_{\{0<\theta^*<1\}}(y_2^{min}(\theta^*))$ into Equations 3.35 and 3.37.

Finally, $\omega_c = \min(\omega_1^*, \omega_2^*)$. As k increases, for a given a and ϕ, subharmonic oscillations occur at higher values for ω. $\square$

Chapter 4

Real-Time Decoding of an Integrate and Fire Encoder

4.1 Introduction

One of the most detailed and widely accepted models of the neuron is the Hodgkin Huxley (HH) model [44]. It is a complex nonlinear model comprising of four differential equations governing the membrane potential dynamics as well as the dynamics of the sodium, potassium and calcium currents found in a neuron. We assume in the practical setting that we are recording multiple neurons using an extracellular electrode, and thus that the observable postprocessed outputs of each neuron are the time points at which the membrane voltage crosses a threshold, also known as spikes. Even with complete knowledge of the HH model parameters, it is intractable to decode the extrinsic signal applied to the neuron given only the spike times. Model reduction techniques are accurate in certain regimes [33]; theoretical studies have also guaranteed an input-output equivalence between a multiplicative or additive extrinsic signal applied to the HH model, and the same signal applied to an Integrate and Fire (IAF) neuron model with variable thresholds [64].

Specifically, take the example of a decoder in a brain machine interface (BMI) device, where the decoded signal drives a prosthetic limb in order to produce movement. Given the complications involved in decoding an extrinsic signal using a realistic neuron model, current practices include decoding using a Kalman filter (Figure 4-1), which often assumes

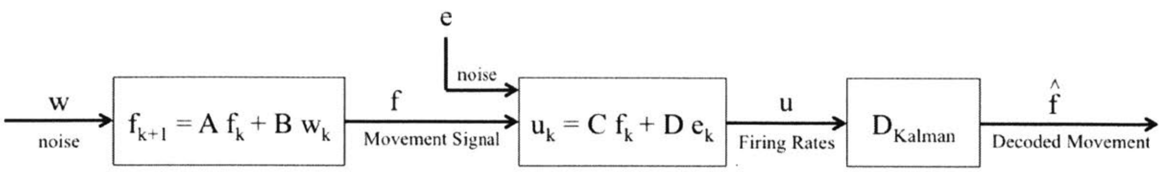

Figure 4-1: Decoding using a Kalman filter D_{Kalman}. Here, the movement signal f is usually parameterized as the states of the dynamical system (A, B, C, D) as shown in the diagram, with the firing rates of different neurons as the output of this system.

a linear time invariant (LTI) encoding with the states representing the desired movement signal, and the firing rate of the neuron(s) as the output [13, 99, 114]. Although extremely tractable for decoding, this approach (i) assumes a specific parametric structure for the movement signal, and (ii) ignores the nonlinear processing of this signal by the neurons. Moreover, assuming firing rates as the output of the neuron averages out the data and incurs inherent delays in the decoding process. Decoding of spike trains has also been performed using stochastic jump models such as point process models [10, 23], and [84] details the relationship between these encoding models and the IAF.

We consider a biophysically inspired IAF neuron model with variable thresholds as the encoding model, and only assume certain bandwidth and decay properties on the reference movement signal. It has been shown that, given the parameters of the model and given the spikes for all time, a bandlimited signal driving the IAF model can be perfectly reconstructed if the spikes are 'dense enough' [61, 67, 26]. This is a Nyquist-type reconstruction formula, although the sampling is non-uniform; specifically, samples of the range of the signal are provided instead of the domain. For this theory to be applicable to a real-time setting, as in the case of BMI, we need a causal real-time decoder that estimates the signal at every time t, and an estimate of the time taken for the convergence of the reconstructed signal to the real signal. There have also been some approaches for causal reconstruction of a signal encoded by an IAF encoder, such as in [27]. However, these do not show the convergence of the estimate to the real signal with the advent of time.

In this paper, we introduce a causal real-time decoder (Figure 4-2) that, given the parameters of the IAF encoding process, provides an estimate of the signal at every time, without the need to wait for a minimum amount of time to start decoding. We show that, under

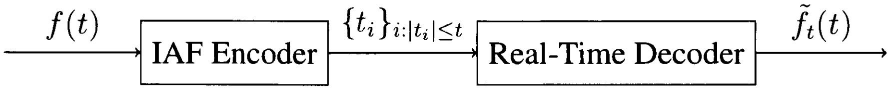

Figure 4-2: IAF Encoder and a Real-Time Decoder.

certain conditions on the input signal, the upper bound of the error between the estimated signal and the input signal decreases polynomially in time, leading to perfect reconstruction as $t \to \infty$, or a bounded error if a finite number of iterations are used. The bounded input bounded output (BIBO) stability of a decoder is extremely important to analyze for the application of a BMI. Here, we show that the $\mathcal{L}_2$ norm of the error is bounded, with an upper bound that depends on the bandwidth of the signal, the density of the spikes, and the decay of the input signal.

We numerically show the utility of the theory developed here. We first provide example reconstructions using the real-time decoder and compare our results with reconstructions obtained assuming a firing rate output. We then show the dependence of the decoding error on the properties of the input signal.

The theory and algorithm presented in this chapter (also presented in [93]) can be applied to any system that uses an IAF encoding device, for example in pluviometry. We introduce some preliminary definitions in Section 4.2, and then present our theoretical results in Section 4.3. We use a model IAF system to numerically simulate the output of an IAF encoder and provide causal real-time reconstruction in Section 4.4, and end this chapter with conclusions in Section 4.5.

4.2 Preliminaries

We first define the subsets of the $\mathcal{L}_2$ space that we consider. $\mathcal{L}_2^\Omega$ and $\mathcal{L}_{2,\beta}^\Omega$ are defined as the following.

$$\mathcal{L}_2^\Omega = \left\{ f \in \mathcal{L}_2 \mid \hat{f}(\omega) = 0 \;\; \forall \omega \notin [-\Omega, \Omega] \right\} \tag{4.1}$$

$$\mathcal{L}_{2,\beta}^\Omega = \left\{ f g_\beta \in \mathcal{L}_2 \mid \hat{f}(\omega) = 0 \;\; \forall \omega \notin [-\Omega, \Omega] \right\} \tag{4.2}$$

where $g_\beta(t) = (1 + |t|)^\beta$ and $\hat{f}(\omega) = (\mathcal{F}f)(\omega)$ is the Fourier transform of f. We will only consider signals in $\mathcal{L}^{\Omega}_{2,\beta}$ for $\beta \geq 0$.

Next, we define $\mathrm{sinc}_\Omega(t)$ and $\mathbb{1}_{[a,b]}(t)$, both of which will play an integral part in the reconstruction of signals.

$$\mathrm{sinc}_\Omega(t) = \begin{cases} \frac{\sin(\Omega t)}{\Omega t} & t \neq 0 \\ 1 & t = 0 \end{cases} \tag{4.3}$$

$$\mathbb{1}_{[a,b]}(t) = \begin{cases} 1 & t \in [a, b] \\ 0 & otherwise \end{cases} \tag{4.4}$$

Finally, we define the encoding system based on an IAF neuron model; we term this the IAF Encoder. We consider that this model has variable thresholds in its most general form, which may be useful if it is the result of a model reduction technique such as in [64], or in approaches where $\int_{t_i}^{t_{i+1}} f(\tau)d\tau$ can be calculated through other means, such as in [61]. A typical IAF Encoder is defined in the following way: given the thresholds $\{q_i\}$ where $q_i > 0 \; \forall i$, the spikes $\{t_i\}$ are such that

$$\int_{t_i}^{t_{i+1}} f(\tau)d\tau = \pm q_i \tag{4.5}$$

This signifies that the encoder outputs a spike at time t_{i+1} every time the integral $\int_{t_i}^{t} f(\tau)d\tau$ reaches the threshold q_i or $-q_i$. We assume that the decoder has knowledge of the value of the integral as well as the time at which the integral was reached. For a physical representation with neurons whose dynamics can faithfully be modeled using IAF neurons, we can imagine two neurons with the same input f; one neuron spikes when the positive threshold is reached while the other spikes when the negative threshold is reached. The decoder views the activity of both of these neurons and, with knowledge of the corresponding thresholds, decodes the signal accordingly. We can also take the approach of limiting ourselves to positive $f(t)$. In order to remain general in the following treatment, we assume that we have knowledge of $\left\{\int_{t_i}^{t_{i+1}} f(\tau)d\tau\right\}$, as well as the corresponding spike times $\{t_i\}$.

4.3 Theoretical Results

The following is a theorem introduced in [26], which was also applied to IAF Encoders in [68, 67, 35]. We will later use the operators and concepts introduced in this theorem.

Theorem 2. *Perfect Reconstruction: Given a sampling set* $\{t_i\}_{i\in\mathcal{Z}}$ *and the corresponding samples* $\int_{t_i}^{t_{i+1}} f(\tau)d\tau$*, we can perfectly reconstruct* $f \in \mathcal{L}_2^{\Omega}$ *if* $\sup_{i\in\mathcal{Z}}(t_{i+1} - t_i) = \delta$ *for some* $\delta < \frac{\pi}{\Omega}$*. Moreover,* f *can be reconstructed iteratively in the following way, such that*

$$\|f - f^k\|_2 \leq \left(\frac{\delta\Omega}{\pi}\right)^{k+1} \|f\|_2 \tag{4.6}$$

and $\lim_{k\to\infty} f^k = f$ *in* $\mathcal{L}_2$.

$$f^0 = \mathcal{A}f \tag{4.7}$$

$$f^1 = (I - \mathcal{A})f^0 + \mathcal{A}f = (I - \mathcal{A})\mathcal{A}f + \mathcal{A}f \tag{4.8}$$

$$f^k = (I - \mathcal{A})f^{k-1} + \mathcal{A}f = \sum_{n=0}^{k}(I - \mathcal{A})^n\mathcal{A}f \tag{4.9}$$

where the operator $\mathcal{A}f$ *is defined as the following.*

$$\mathcal{A}f = \sum_{i=1}^{\infty} \int_{t_i}^{t_{i+1}} f(\tau)d\tau \ \mathrm{sinc}_{\Omega}(t - s_i) \tag{4.10}$$

and $s_i = \frac{t_i+t_{i+1}}{2}$*, the midpoint of each pair of spikes.*

Proof. Provided in the Appendix. Also in [26]. □

Corollary 3. *Perfect Reconstruction after sampling with a multiplicative function: Let* $h \in \mathcal{L}_2$ *such that*

$$\frac{\int_{t_i}^{t_{i+1}} |1 - h(\tau)|^2 d\tau}{t_{i+1} - t_i} \leq \epsilon^2 \tag{4.11}$$

for some ϵ. *Given a sampling set* $\{t_i\}_{i\in\mathcal{Z}}$ *and the corresponding samples* $\int_{t_i}^{t_{i+1}} f(\tau)h(\tau)d\tau$, *we can perfectly reconstruct* $f \in \mathcal{L}_2^{\Omega}$ *if* $\sup_{i\in\mathcal{Z}}(t_{i+1} - t_i) = \delta$ *for* δ *such that* $\frac{\delta\Omega}{\pi} + \epsilon\left(1 + \frac{\delta\Omega}{\pi}\right) < 1$.

Remark 1. *Corollary 3 can be applied to IAF neurons sampled with a refractory period* R *if* f *can be upper bounded by a known quantity* F, *i.e.* $|f(t)| < F\ \forall t$ *[61]. Here,* $h(t) = \sum_{i\in\mathcal{Z}} \mathbb{1}_{[t_i+R,t_{i+1}]}$ *and* $\epsilon^2 = \frac{R}{\delta/F+R}$. *It can also be applied to leaky IAF neurons [62], with* $h(t) = \sum_{i\in\mathcal{Z}} \exp(\frac{-(t_{i+1}-t)}{b})\mathbb{1}_{[t_i,t_{i+1}]}$ *for some* b, *and* $\epsilon = 1 - \exp(-\delta/b)$, *which imposes a constraint on* b *for given values of* δ *and* Ω*: that the current may not decay 'too much'.*

Although providing perfect reconstruction, Theorem 2 and Corollary 3 both require an infinite number of spikes in order to start decoding. No results exist for the truncation errors for decoding from an IAF neuron, i.e. what happens if we have a finite number of spikes? We provide results for this question while considering real-time decoding. We would like a real-time decoder that outputs the 'best guess' at every time t in order for us to act on the estimate of the signal. In this paper, we introduce one such decoder; we first provide a high-level description of the real-time decoder, then a recursive algorithm to apply in the practical case, and finally we will provide error bounds for its performance.

Real-Time Decoder

At every time t, the decoder outputs an estimate of the input signal $\tilde{f}_t(t)$, where $\tilde{f}_t(t)$ is an estimate of the signal calculated using all the spikes from time 0 to t. Since there is no new information between spikes, this is essentially the same as calculating an estimate after every spike t_i, $\tilde{f}_{t_i}(t)$, and using this estimate till the next spike, i.e. for time $t \in [t_i, t_{i+1}]$ (see Figure 4-3).

We will show that we can calculate the estimate after every spike $\tilde{f}_{t_{i+1}}$ as the sum of the previous estimate $\tilde{f}_{t_i}$ and an innovation $g_{t_{i+1}}$. This procedure is captured in the algorithm given in Equations 4.12 and 4.13.

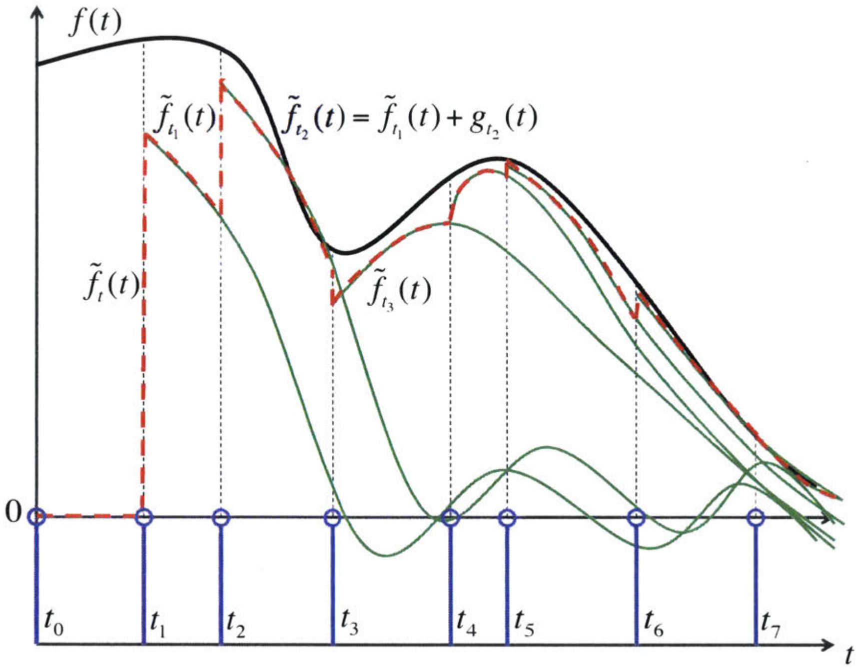

Figure 4-3: A visualization of the decoding process. The original signal $f(t)$ is shown in black and the spikes $\{t_i\}$ are shown in blue. As each spike t_i arrives, a new estimate $\tilde{f}_{t_i}(t)$ of the signal is formed (shown in green), which is modified after the next spike t_{i+1} by the innovation function $g_{t_{i+1}}$. The output of the decoder $\tilde{f}_t(t) = \sum_{i \in \mathcal{Z}} \tilde{f}_{t_i}(t) \mathbb{1}_{[t_i, t_{i+1})}(t)$ is shown in red.

Recursive Algorithm

$$\tilde{f}^0_{t_{i+1}} = \tilde{f}^0_{t_i} + g^0_{t_{i+1}} \tag{4.12}$$

$$\tilde{f}^k_{t_{i+1}} = \tilde{f}^k_{t_i} + g^k_{t_{i+1}} = \tilde{f}^k_{t_i} + \left(g^{k-1}_{t_{i+1}} + g^0_{t_{i+1}} - \mathcal{A}_{t_{i+1}} g^{k-1}_{t_{i+1}} \right) \tag{4.13}$$

Here, $\tilde{f}^0_{t_0} = 0$, and $g^0_{t_{i+1}}(t) = \left(\int_{t_i}^{t_{i+1}} f(\tau) d\tau \right) \operatorname{sinc}(t - s_i)$. We denote $\tilde{f}_{t_i}(t) = \lim_{k \to \infty} \tilde{f}^k_{t_i}(t)$ and $g_{t_{i+1}}(t) = \lim_{k \to \infty} g^k_{t_{i+1}}(t)$. We define the operator $\mathcal{A}_T f$ used in Equation 4.13 as the following.

$$\mathcal{A}_T f = \sum_{i : |t_i| \leq T} \int_{t_i}^{t_{i+1}} f(\tau) d\tau \operatorname{sinc}_\Omega(t - s_i) \tag{4.14}$$

The output of our causal real-time decoder can also be written as the following.

$$\tilde{f}_t(t) = \sum_{i \in \mathcal{Z}} \tilde{f}_{t_i}(t) \mathbb{1}_{[t_i, t_{i+1})}(t) \tag{4.15}$$

In the case of a decoder that uses a finite number of iterations K at every step, i.e. calculates $\tilde{f}^K_{t_i}$ after every spike t_i, the decoded signal is $\tilde{f}^K_t(t) = \sum_{i \in \mathcal{Z}} \tilde{f}^K_{t_i}(t) \mathbb{1}_{[t_i, t_{i+1})}(t)$. $\{\tilde{f}^k_{t_i}\}_k$ are stored after every spike t_i, and thus do not need to be recomputed at the arrival of the next spike. Thus, when a new spike arrives at t_{i+1}, each $\tilde{f}^k_{t_i}$ can be modified by adding the innovation functions $g^k_{t_{i+1}}$.

Next, we show an upper bound on the error incurred by the decoder.

Theorem 3. *Real-time reconstruction: Given a signal* $f \in \mathcal{L}^{\Omega}_{2,\beta}$ *passed through an IAF encoder with known thresholds, and given that the spikes satisfy a certain minimum density* $\sup_{i \in \mathbb{Z}}(t_{i+1} - t_i) = \delta$ *for some* $\delta < \frac{\Omega}{\pi}$, *we can construct a causal real-time decoder that reconstructs a function* $\tilde{f}_t(t)$ *using the recursive algorithm in Equations 4.12 and 4.13, s.t.*

$$|f(t) - \tilde{f}_t(t)| \leq \frac{c}{1 - \frac{\delta\Omega}{\pi}} \|f\|_{2,\beta}(1+t)^{-\beta} \tag{4.16}$$

, where c depends only on δ, Ω *and* β.

Moreover, if we use a finite number of iterations K *at every step, we obtain the following error.*

$$|f(t) - \tilde{f}^K_t(t)| \leq c \frac{1 - \left(\frac{\delta\Omega}{\pi}\right)^{K+1}}{1 - \frac{\delta\Omega}{\pi}} \|f\|_{2,\beta}(1+t)^{-\beta} + \left(\frac{\delta\Omega}{\pi}\right)^{K+1} \frac{1 + \frac{\delta\Omega}{\pi}}{1 - \frac{\delta\Omega}{\pi}} \|f\|_2 \tag{4.17}$$

Theorem 3 shows that the upper bound of the real-time reconstruction error using the decoding algorithm in Equations 4.12 and 4.13, decreases as a function of time. This implies that the approximation $\tilde{f}_t(t)$ becomes more and more accurate with the passage of time, and moreover, we can calculate the exact amount of time we would need to record to have a given level of accuracy. Given a maximum allowed error $\epsilon > 0$, these bounds can provide a combination (t, K) that will ensure $|f(t) - \tilde{f}^K_t(t)| \leq \epsilon$ if $f \in \mathcal{L}^{\Omega}_{2,\beta}$, and if the density constraint is met.

We can further show that the $\mathcal{L}_2$ norm of the reconstruction remains bounded with a bounded input (BIBO stability), by bounding the $\mathcal{L}_2$ norm of the error between the original signal and the reconstruction.

Corollary 4. *Bounded $\mathcal{L}_2$ norm: The causal decoder provided in Theorem 3, with the same assumptions and in the case of $K \to \infty$, constructs a signal $\tilde{f}_t(t)$ s.t. the $\mathcal{L}_2$ norm of the error $\|f - \tilde{f}_t\|_2 = \sqrt{\int_0^\infty |f(t) - \tilde{f}_t(t)|^2 dt}$ is bounded: $\|f - \tilde{f}_t\|_2 \leq \frac{c/\sqrt{2\beta-1}}{1-\frac{\delta\Omega}{\pi}}\|f\|_{2,\beta}$ where c is the same constant as in Theorem 3.*

Remark 1: This result also implies that we have a decay in the root-mean-square (RMS) error, i.e. $\sqrt{\frac{1}{T}\int_0^T |f(t) - \tilde{f}_t(t)|^2 dt} \xrightarrow{T\to\infty} 0$. For the case of a finite number of iterations $K < \infty$, the RMS error converges to a non-zero constant $\left(\frac{\delta\Omega}{\pi}\right)^{K+1} \frac{1+\frac{\delta\Omega}{\pi}}{1-\frac{\delta\Omega}{\pi}}\|f\|_2$.

Remark 2: The methods used in Corollary 4 also provide a bound on the error in the weighted $\mathcal{L}_2$ norm, i.e. $\|f - \tilde{f}\|_{2,\beta} \leq \frac{c/\sqrt{\beta-1}}{1-\frac{\delta\Omega}{\pi}}\|f\|_{2,\beta}$ for $\beta \geq 2$, which may be a more intuitive form to use for a subsequent stability analysis.

Corollary 5. *Real-Time Reconstruction after sampling with a multiplicative function: Let the assumptions in Corollary 3 hold. If $f \in \mathcal{L}^{\Omega}_{2,\beta}$ and we receive samples of $\int_{t_i}^{t_{i+1}} f(\tau)h(\tau)d\tau$, we can construct a causal real-time decoder that reconstructs a function $\tilde{f}_t(t)$ such that*

$$|f(t) - \tilde{f}_t(t)| \leq \frac{c_{\delta,\Omega,\beta}(1+\epsilon)}{1 - \left(\frac{\delta\Omega}{\pi} + \epsilon\left(1 + \frac{\delta\Omega}{\pi}\right)\right)}\|f\|_{2,\beta}(1+t)^{-\beta} \tag{4.18}$$

where $c_{\delta,\Omega,\beta}$ is the same as defined in Theorem 3, and ϵ is the same as defined in Corollary 3.

Corollary 5 can be applied to the real-time reconstruction if receiving spikes from an IAF neuron with a refractory period, or a leaky IAF neuron, by applying the concepts in Remark 1.

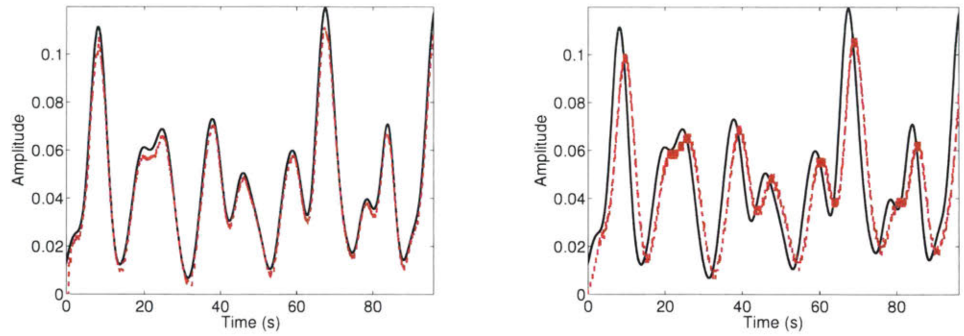

(A) $\Omega = 0.2\pi$; Real-Time Decoder (B) $\Omega = 0.2\pi$; Linear FR Decoder

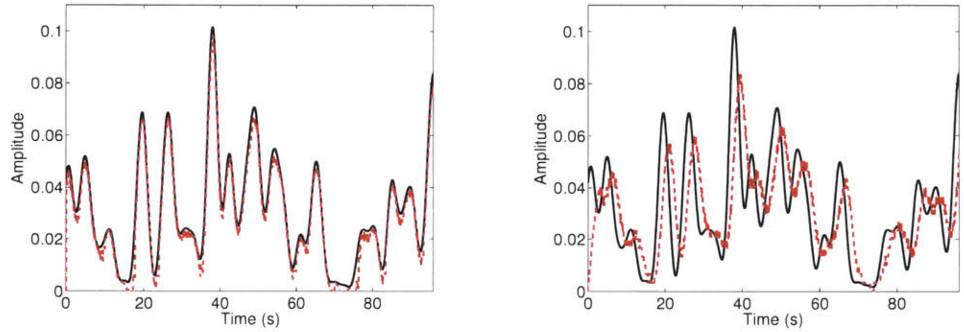

(C) $\Omega = 0.3\pi$; Real-Time Decoder (D) $\Omega = 0.3\pi$; Linear FR Decoder

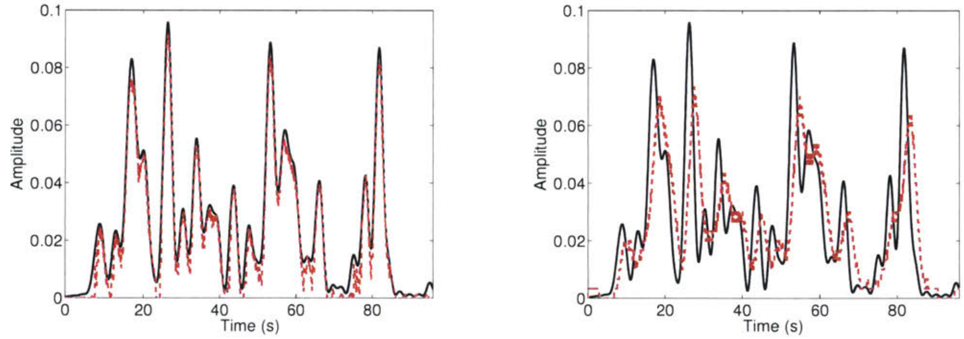

(E) $\Omega = 0.4\pi$; Real-Time Decoder (F) $\Omega = 0.4\pi$; Linear FR Decoder

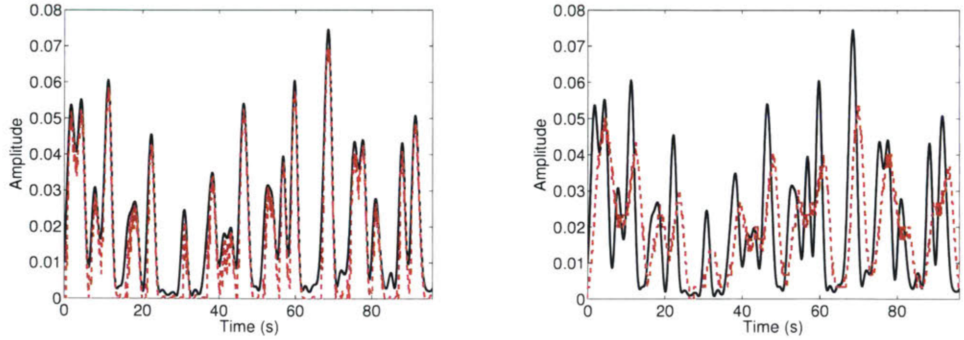

(G) $\Omega = 0.5\pi$; Real-Time Decoder (H) $\Omega = 0.5\pi$; Linear FR Decoder

Figure 4-4: (A,C,E,G) Four example reconstructions using the Real-Time Decoder, with the original signal $f(t)$ in black solid and the reconstructed signal $\tilde{f}_t(t)$ in red dashed lines. Here, $[\beta, K] = [2, 500]$, and $q_i = 0.01\ \forall i$. (B,D,F,G) The same signal was decoded using a Linear Firing Rate (FR) Decoder. A window size of $\Delta = 3$s was used.

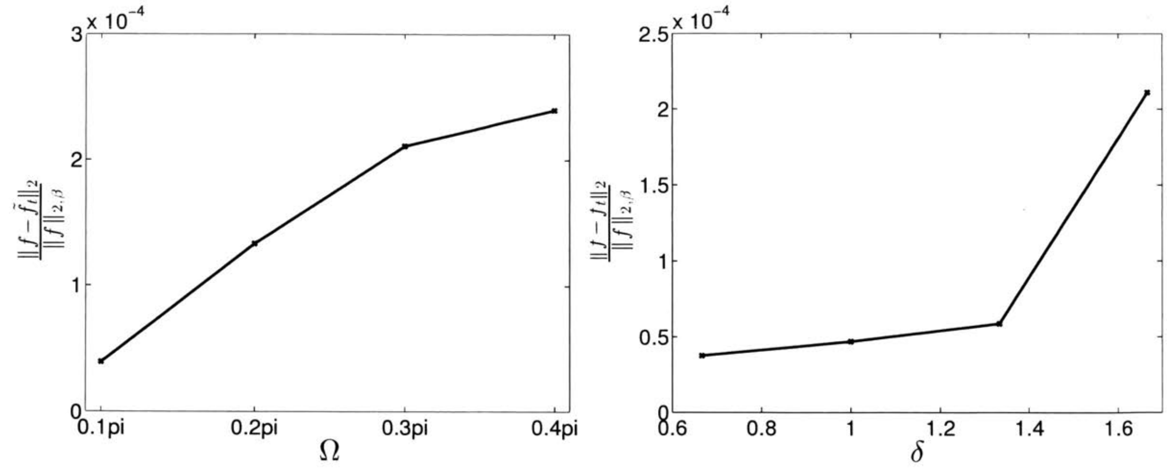

(A) Ω is varied; $[\beta, \delta, K] = [2, \frac{\pi}{2\Omega}, 500]$ (B) δ is varied; $[\Omega, \beta, K] = [0.3\pi, 2, 500]$

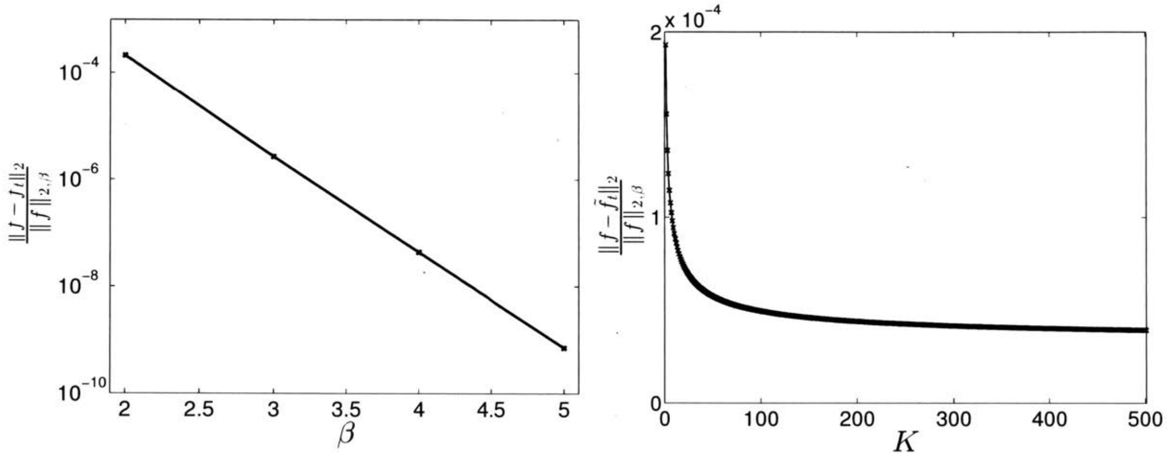

(C) β is varied; $[\Omega, \delta, K] = [0.3\pi, \frac{1}{0.3\beta}, 500]$ (D) K is varied; $[\Omega, \delta, \beta] = [0.3\pi, \frac{5}{3}, 2]$

Figure 4-5: Average error for 20 different signals while varying different parameters.

4.4 Numerical Simulations

We simulated signals $f(t)$ of the following form, for $t \in [0, 100]$, using a stepsize of 10^{-2}.

$$f(t) = \frac{\sum_{i=1}^{50} w_k \left(\operatorname{sinc}_\Omega (t - d_k)\right)^\beta}{\sum_{i=1}^{50} w_k} \tag{4.19}$$

Here, the w_k's and d_k's were picked uniformly at random from the interval $[0, 1]$ and $[0, 100]$ respectively. Note that $f \in \mathcal{L}_{2,\beta}^{\beta\Omega}$. All simulations were performed using MATLAB R2014a. For each simulation experiment, at every time t we decoded using only the spikes before time t.

We first provide example reconstructions using the Real-Time Decoder for four signals in Figure 4-4, using constant thresholds, i.e. $q_i = q \; \forall i$. We compare our results to those obtained using a Linear Firing Rate (FR) Decoder, i.e. we let the reconstructed signal be a linear function of the number of spikes in the past Δ seconds, Δ being the window size. We can see that there is a delay in the reconstruction with this decoding approach. Moreover, the reconstruction is not as accurate as that using the Real-Time Decoder.

Next, we show the decay of the real-time error by averaging out the error for 20 different input signals, while varying certain parameters, namely Ω, β, δ and K (Figure 4-5). The thresholds q_i were chosen to be constant a priori, but were reduced to satisfy the density constraint wherever necessary.

According to Equation 4.41 (including the effect of the constant c), the error should decrease as Ω is decreased. We see this effect in the simulation study in Figure 4-5A. For these simulations, we chose δ such that $\frac{\delta\Omega}{\pi} < 1$, thus δ was decreasing as Ω increased; however, the effect of the increasing Ω dominated in this case.

In Figure 4-5B we see that increasing δ while keeping the bandwidth constant does indeed increase the error, thus the algorithm is sensitive to the density of the spikes. In this figure, all the values of δ satisfy the density constraint, i.e. $\frac{\delta\Omega}{\pi} < 1$.

Increasing β is seen to have a large effect, as seen in Figure 4-5C: the error decreases polynomially in β (note the log scale on the y-axis). Although increasing β in our simulations also increased the bandwidth of the signal, the faster decay had a larger effect on the error than the change in bandwidth.

In Figure 4-5D, the effect of increasing K is apparent; however, this error flattens out for large values of K, showing convergence of the algorithm.

4.5 Conclusions

We provide a real-time decoder to reconstruct a signal $f \in \mathcal{L}_{2,\beta}^{\Omega}$ encoded by an IAF encoder. Under Nyquist-type spike density conditions, we show that the reconstructed signal $\tilde{f}_t(t)$ converges to $f(t)$ polynomially in time, or with a fixed error that depends on the computation power used to reconstruct the function. Moreover, we get a lower error as the spike density increases, i.e. we get better results if we have more spikes. Decreasing the bandwidth or increasing the decay of the signal both lead to a decrease in the error, corroborated by the numerical simulations. In simulation, this decoder outperforms the linear decoder that acts on the firing rate of the neuron. However, the main utility of this decoder is that it comes with verifiable bounds on the error of decoding as we record more spikes.

There is a severe need in the BMI community for considering error bounds while decoding signals from the brain. For example, in the case where the reconstructed signal is driving a prosthetic, we are usually placing the decoder and machine in an inherent feedback loop (where the feedback is visual in this case). A stability analysis of this feedback loop includes calculating a bound on the error incurred by the decoding process, which is the first step for the construction of a device that robustly tracks agile maneuvers. In this chapter, we provide an upper bound on the error incurred by the real-time decoding process, which can be used along with concepts in robust control theory to provide sufficient conditions on the prosthetic and feedback system in order to ensure stability. Stability analysis for the decoder presented in this chapter is provided in Chapter 5.

4.6 Proofs for Chapter 4

Here, we provide the proofs for theorems and corollaries presented in this chapter. For readability, the theorems and corollaries are also provided here again.

Theorem 2. *Perfect Reconstruction: Given a sampling set* $\{t_i\}_{i \in \mathcal{Z}}$ *and the corresponding samples* $\int_{t_i}^{t_{i+1}} f(\tau)d\tau$, *we can perfectly reconstruct* $f \in \mathcal{L}_2^\Omega$ *if* $\sup_{i \in \mathcal{Z}}(t_{i+1} - t_i) = \delta$ *for some* $\delta < \frac{\pi}{\Omega}$. *Moreover,* f *can be reconstructed iteratively in the following way, such that*

$$\|f - f^k\|_2 \leq \left(\frac{\delta\Omega}{\pi}\right)^{k+1} \|f\|_2 \tag{4.20}$$

, *and* $\lim_{k\to\infty} f^k = f$ *in* $\mathcal{L}_2$.

$$\begin{aligned} f^0 &= \mathcal{A}f && (4.21)\\ f^1 &= (I-\mathcal{A})f^0 + \mathcal{A}f = (I-\mathcal{A})\mathcal{A}f + \mathcal{A}f && (4.22)\\ f^k &= (I-\mathcal{A})f^{k-1} + \mathcal{A}f = \sum_{n=0}^{k}(I-\mathcal{A})^n\mathcal{A}f && (4.23)\end{aligned}$$

, *where the operator* $\mathcal{A}f$ *is defined as the following.*

$$\mathcal{A}f = \sum_{i=1}^{\infty}\int_{t_i}^{t_{i+1}} f(\tau)d\tau \ \mathrm{sinc}_\Omega(t-s_i) \qquad (4.24)$$

and $s_i = \frac{t_i+t_{i+1}}{2}$, *the midpoint of each pair of spikes.*

Proof. As presented in [26]

We first define an operator $\mathcal{A}f$ built only from the samples of $f(t)$. We will then show that applying this operator iteratively leads to perfect reconstruction of f under some conditions.

$$\mathcal{A}f = \sum_{i=1}^{\infty}\int_{t_i}^{t_{i+1}} f(\tau)d\tau \ \mathrm{sinc}_\Omega(t-s_i) \qquad (4.25)$$

Here, $s_i = \frac{t_i+t_{i+1}}{2}$, the midpoint of each pair of spikes.

Next, we calculate the error $\|f-\mathcal{A}f\|_2$ incurred by this operator. It is easier to calculate the error incurred by the adjoint $\mathcal{A}^*$, calculated below. In the following, we take both f and g to lie in $\mathcal{L}_2^\Omega$. Since f is bandlimited, $f = \mathrm{sinc}_\Omega * f$, where $*$ denotes convolution.

$$\begin{aligned} \langle f, \mathcal{A}^*g\rangle = \langle \mathcal{A}f, g\rangle &= \left\langle \sum_{i=1}^{\infty} \left\langle \mathrm{sinc}_\Omega * f, \mathbb{1}_{[t_i,t_{i+1}]}\right\rangle \ \mathrm{sinc}_\Omega(\cdot - s_i), g \right\rangle && (4.26)\\ &= \sum_{i=1}^{\infty} \left\langle f, \mathrm{sinc}_\Omega * \mathbb{1}_{[t_i,t_{i+1}]}\right\rangle \langle \mathrm{sinc}_\Omega(\cdot - s_i), g\rangle && (4.27)\\ &= \sum_{i=1}^{\infty} \left\langle f, \mathrm{sinc}_\Omega * \mathbb{1}_{[t_i,t_{i+1}]}\right\rangle g(s_i) && (4.28)\end{aligned}$$

Thus it follows that the adjoint operator $\mathcal{A}^*$ is defined as the following.

$$\mathcal{A}^* f = \sum_{i=1}^{\infty} f(s_i)(\mathrm{sinc}_\Omega * \mathbb{1}_{[t_i,t_{i+1}]}) \tag{4.29}$$

Note that $\mathcal{A}^* f \in \mathcal{L}_2^\Omega$ for all $f \in \mathcal{L}_2^\Omega$.

We now bound the error $\|f - \mathcal{A}^* f\|_2$.

$$\begin{aligned}
\|f - \mathcal{A}^* f\|_2^2 &= \left\| \mathrm{sinc}_\Omega * \left(f - \sum_{i \in \mathcal{Z}} f(s_i)\mathbb{1}_{[t_i,t_{i+1}]} \right) \right\|_2^2 && (4.30)\\
&\leq \left\| \sum_{i \in \mathcal{Z}} (f - f(s_i))\mathbb{1}_{[t_i,t_{i+1}]} \right\|_2^2 && (4.31)\\
&= \sum_{i \in \mathcal{Z}} \int_{t_i}^{t_{i+1}} |f(t) - f(s_i)|^2 dt && (4.32)
\end{aligned}$$

We split each integral in Equation (4.32) in two and use Wirtinger's inequality [26] to bound these (we need $f, f' \in \mathcal{L}^2(t_{i-1}, t_i),\ \forall\, i$). We have,

$$\begin{aligned}
\int_{t_i}^{t_{i+1}} |f(t) - f(s_i)|^2 dt &\leq \frac{4}{\pi^2}(s_i - t_i)^2 \int_{t_i}^{s_i} |f'(t)|^2 dt + \frac{4}{\pi^2}(t_{i+1} - s_i)^2 \int_{s_i}^{t_{i+1}} |f'(t)|^2 dt\\
&\leq \frac{\delta^2}{\pi^2} \int_{t_i}^{t_{i+1}} |f'(t)|^2 dt
\end{aligned}$$

We sum over i and use Bernstein's inequality [26] to obtain

$$\|f - \mathcal{A}^* f\|_2^2 \leq \frac{\delta^2}{\pi^2}\|f'\|_2^2 \leq \frac{\delta^2 \Omega^2}{\pi^2}\|f\|_2^2 \tag{4.33}$$

Given that $\|\mathcal{A}\|_2 = \|\mathcal{A}^*\|_2$, we see that $\|f - \mathcal{A}f\|_2 \leq \frac{\delta\Omega}{\pi}\|f\|_2$.

Finally, if $\delta < \frac{\pi}{\Omega}$, $f \in \mathcal{L}_2^\Omega$ is uniquely determined by its samples $\int_{t_i}^{t_{i+1}} f(\tau)d\tau$ and can be reconstructed iteratively as the following.

$$\begin{aligned}
f_0 &= \mathcal{A}f && (4.34)\\
f_1 &= (I - \mathcal{A})f_0 + \mathcal{A}f = (I - \mathcal{A})\mathcal{A}f + \mathcal{A}f && (4.35)\\
f_k &= (I - \mathcal{A})f_{k-1} + \mathcal{A}f = \sum_{n=0}^{k} (I - \mathcal{A})^n \mathcal{A}f && (4.36)
\end{aligned}$$

If $\frac{\delta\Omega}{\pi} < 1$, then $\lim_{k\to\infty} f_k = f$ in $\mathcal{L}_2$. $\square$

Corollary 3. *Perfect Reconstruction after sampling with a multiplicative function: Let $h \in \mathcal{L}_2$ such that*

$$\frac{\int_{t_i}^{t_{i+1}} |1 - h(\tau)|^2 d\tau}{t_{i+1} - t_i} \leq \epsilon^2 \tag{4.37}$$

for some ϵ. Given a sampling set $\{t_i\}_{i\in\mathcal{Z}}$ and the corresponding samples $\int_{t_i}^{t_{i+1}} f(\tau)h(\tau)d\tau$, we can perfectly reconstruct $f \in \mathcal{L}_2^{\Omega}$ if $\sup_{i\in\mathcal{Z}}(t_{i+1} - t_i) = \delta$ for δ such that $\frac{\delta\Omega}{\pi} + \epsilon\left(1 + \frac{\delta\Omega}{\pi}\right) < 1$.

Proof. We define the following operator $\mathcal{A}_h$.

$$\mathcal{A}_h f = \sum_{i=1}^{\infty} \int_{t_i}^{t_{i+1}} f(\tau)h(\tau)d\tau \ \mathrm{sinc}_{\Omega}(t - s_i) \tag{4.38}$$

Its adjoint is given by the following, where $\bar{h}(t) = h(-t)$.

$$\mathcal{A}_h^* f = \sum_{i=1}^{\infty} f(s_i)(\mathrm{sinc}_{\Omega} * \bar{h}\mathbb{1}_{[t_i,t_{i+1}]}) \tag{4.39}$$

We now calculate an upper bound on $\|f - \mathcal{A}_h^* f\|_2 = \|f - \mathcal{A}_h f\|_2$ as the following.

$$
\begin{aligned}
\|f - \mathcal{A}_h^* f\|_2 &= \left\| f * \mathrm{sinc}_\Omega - \sum_{i \in \mathcal{Z}} f(s_i) h \mathbb{1}_{[t_i, t_{i+1}]} * \mathrm{sinc}_\Omega \right\|_2 \\
&\leq \left\| f - \sum_{i \in \mathcal{Z}} f(s_i) h \mathbb{1}_{[t_i, t_{i+1}]} \right\|_2 \\
&\leq \left\| f - \sum_{i \in \mathcal{Z}} f(s_i) \mathbb{1}_{[t_i, t_{i+1}]} \right\|_2 + \left\| \sum_{i \in \mathcal{Z}} f(s_i)(1-h) \mathbb{1}_{[t_i, t_{i+1}]} \right\|_2 \\
&\leq \frac{\delta\Omega}{\pi} \|f\|_2 + \sqrt{\sum_{i \in \mathcal{Z}} \int_{t_i}^{t_{i+1}} |f(s_i)|^2 |1 - h(\tau)|^2 d\tau} \\
&\leq \frac{\delta\Omega}{\pi} \|f\|_2 + \epsilon \sqrt{\sum_{i \in \mathcal{Z}} \int_{t_i}^{t_{i+1}} |f(s_i)|^2 d\tau} \\
&\leq \frac{\delta\Omega}{\pi} \|f\|_2 + \epsilon \left\| \sum_{i \in \mathcal{Z}} f(s_i) \mathbb{1}_{[t_i, t_{i+1}]} \right\|_2 \\
&\leq \frac{\delta\Omega}{\pi} \|f\|_2 + \epsilon \left(1 + \frac{\delta\Omega}{\pi}\right) \|f\|_2 \\
&= \left(\frac{\delta\Omega}{\pi} + \epsilon \left(1 + \frac{\delta\Omega}{\pi}\right)\right) \|f\|_2
\end{aligned}
$$

Now we have the following condition for perfect recovery:

$$
\left(\frac{\delta\Omega}{\pi} + \epsilon \left(1 + \frac{\delta\Omega}{\pi}\right)\right) < 1 \tag{4.40}
$$

We can reconstruct the function f in the same way as in Theorem 2, using the operator $\mathcal{A}_h$ instead of $\mathcal{A}$. □

Theorem 3. *Real-time reconstruction: Given a signal* $f \in \mathcal{L}_{2,\beta}^{\Omega}$ *passed through an IAF encoder with known thresholds, and given that the spikes satisfy a certain minimum density* $\sup_{i \in \mathbb{Z}}(t_{i+1} - t_i) = \delta$ *for some* $\delta < \frac{\Omega}{\pi}$*, we can construct a causal real-time decoder that reconstructs a function* $\tilde{f}_t(t)$ *using the recursive algorithm in Equations* 11 *and* 12*, s.t.*

$$
|f(t) - \tilde{f}_t(t)| \leq \frac{c_{\delta,\Omega,\beta}}{1 - \frac{\delta\Omega}{\pi}} \|f\|_{2,\beta} (1+t)^{-\beta} \tag{4.41}
$$

, where c depends only on δ, Ω *and* β.

Moreover, if we use a finite number of iterations K *at every step, we obtain the following error.*

$$|f(t) - \tilde{f}_t^K(t)| \le c_{\delta,\Omega,\beta}\frac{1-\left(\frac{\delta\Omega}{\pi}\right)^{K+1}}{1-\frac{\delta\Omega}{\pi}}\|f\|_{2,\beta}(1+t)^{-\beta} + \left(\frac{\delta\Omega}{\pi}\right)^{K+1}\frac{1+\frac{\delta\Omega}{\pi}}{1-\frac{\delta\Omega}{\pi}}\|f\|_2 \quad (4.42)$$

Proof. We start with a few preliminaries, and the definition of a constant c that will be used later in the proof. These preliminary notions are also provided in [25]. We define a local maximum function on f:

$$f^{\#}(t) = \sup_{|u|\le\delta}|f(t+u)| \quad (4.43)$$

Note the following two properties of $f^{\#}(t)$ for $f \in \mathcal{L}_2^{\Omega}$, with a function $p_\alpha(t)$ such that $\hat{p}_\alpha(\omega) = 1$ for $\omega \in [-\Omega, \Omega]$, and $p_\alpha \in \mathcal{L}_{1,\alpha}$, for some $\alpha \ge \beta$. Here, $*$ denotes the convolution operator.

$$|\sum_{i=1}^{\infty} f(s_i)\mathbb{1}_{[t_i,t_{i+1}]}(t)| \le f^{\#}(t) \text{ pointwise} \quad (4.44)$$

$$f^{\#}(t) = (f * p_\alpha)^{\#}(t) \le (|f| * p_\alpha^{\#})(t) \quad (4.45)$$

As a consequence of equation (5.21), we obtain the following bound on the $\mathcal{L}_{2,\beta}$ norm of the local maximum function (5.19), using a function $p_\alpha(t)$ as described above.

$$\|f^{\#}\|_{2,\beta} \le \inf_{p_\alpha}\|p_\alpha^{\#}\|_{1,\alpha}\|f\|_{2,\beta} \quad (4.46)$$

We denote $\inf_{p_\alpha}\|p_\alpha^{\#}\|_{1,\alpha}$ for some $\alpha \ge \beta$ by $c_{\delta,\Omega,\beta}$, which depends only on δ, Ω and β.

We now bound the $\mathcal{L}_2$ norm of the error incurred using a decoder acting on all the spikes in a finite time period T, i.e. $\{t_i\}_{i:|t_i|\le T}$, and show that this error is decaying in T.

We consider that after the first approximation $\mathcal{A}_T f$ with a finite number of spikes, we can construct $\{t_i\}_{i:|t_i|>T}$ such that $\sup_{i:|t_i|>T}(t_{i+1} - t_i)$ is less than the required δ. Thus we can construct an operator $\mathcal{A}$ as long as it is not acting directly on f, where $\mathcal{A}$ is defined as in Theorem 2. The adjoint operators of $\mathcal{A}$ and $\mathcal{A}_T$ for $f \in \mathcal{L}_2^\Omega$ are $\mathcal{A}^*$ and $\mathcal{A}_T^*$ respectively.

$$\mathcal{A}^* f = \sum_{i \in \mathbb{Z}} f(s_i)(\mathrm{sinc}_\Omega * \mathbb{1}_{[t_i, t_{i+1}]}) \tag{4.47}$$

$$\mathcal{A}_T^* f = \sum_{i:|t_i| \leq T} f(s_i)(\mathrm{sinc}_\Omega * \mathbb{1}_{[t_i, t_{i+1}]}) \tag{4.48}$$

Equation 4.47 is shown in the proof of Theorem 2, and Equation 4.48 follows similarly. We first define $\tilde{f}_T$ as the result of the following iteration, i.e. $\tilde{f}_T = \lim_{k\to\infty} \tilde{f}_T^k$.

$$\tilde{f}_T^0 = \mathcal{A}_T f \tag{4.49}$$

$$\tilde{f}_T^1 = (I - \mathcal{A})\tilde{f}_T^0 + \mathcal{A}_T f = (I - \mathcal{A})\mathcal{A}_T f + \mathcal{A}_T f \tag{4.50}$$

$$\tilde{f}_T^k = (I - \mathcal{A})\tilde{f}_T^{k-1} + \mathcal{A}_T f = \sum_{n=0}^{k} (I - \mathcal{A})^n \mathcal{A}_T f \tag{4.51}$$

To derive $||f - \tilde{f}_T||_2$ for $f \in \mathcal{L}_2^\Omega$, we first note that the error incurred using a finite number of spikes is the same as the error in the adjoint space, i.e. $||f - \tilde{f}_T||_2 = ||f - \sum_{n=0}^\infty (I - \mathcal{A})^n \mathcal{A}_T f||_2 = ||f - \sum_{n=0}^\infty (I - \mathcal{A}^*)^n \mathcal{A}_T^* f||_2$

We can thus work exclusively with the adjoint operators $\mathcal{A}^* f$ and $\mathcal{A}_T^* f$ in order to derive

$\|f - \tilde{f}_T\|_2$ [12].

$$\begin{aligned}
\|f - \tilde{f}_T\|_2 &= \left\|\sum_{n=0}^{\infty}(I - \mathcal{A}^*)^n(\mathcal{A}^* f - \mathcal{A}_T^* f)\right\|_2 \leq \sum_{n=0}^{\infty} \|(I - \mathcal{A}^*)^n(\mathcal{A}^* f - \mathcal{A}_T^* f)\|_2 \\
&\leq \sum_{n=0}^{\infty}(\frac{\delta\Omega}{\pi})^{n+1}\|\mathcal{A}^* f - \mathcal{A}_T^* f\|_2 = \frac{1}{1-\frac{\delta\Omega}{\pi}}\left\|\sum_{i:|t_i|>T} f(s_i)\mathbb{1}_{[t_i,t_{i+1}]} * \mathrm{sinc}_\Omega\right\|_2 \\
&\leq \frac{1}{1-\frac{\delta\Omega}{\pi}}\left\|\sum_{i:|t_i|>T} f(s_i)\mathbb{1}_{[t_i,t_{i+1}]}\right\|_2 &(4.52)\\
&\leq \frac{1}{1-\frac{\delta\Omega}{\pi}}\left\|f^{\#}\mathbb{1}_{\mathbb{R}\setminus[-T,T]}\right\|_2 \quad (using\ (5.21)) &(4.53)\\
&= \frac{1}{1-\frac{\delta\Omega}{\pi}}\left\|f^{\#}\mathbb{1}_{\mathbb{R}\setminus[-T,T]}(1+|t|)^{\beta}(1+|t|)^{-\beta}\right\|_2 \\
&\leq \frac{1}{1-\frac{\delta\Omega}{\pi}}\left\|f^{\#}\right\|_{2,\beta} \sup_{t\in\mathbb{R}\setminus[-T,T]}(1+|t|)^{-\beta} \\
&\leq \frac{c_{\delta,\Omega,\beta}}{1-\frac{\delta\Omega}{\pi}}\|f\|_{2,\beta}(1+T)^{-\beta} \quad (using\ (5.22)) &(4.54)
\end{aligned}$$

, where $c_{\delta,\Omega,\beta}$ depends only on δ, Ω and β.

Now, only using a finite number of iterations, we have the following error bound.

$$\begin{aligned}
\|f - \tilde{f}_T^K\|_2 &= \left\|\sum_{n=0}^{\infty}(I - \mathcal{A}^*)^n\mathcal{A}^* f - \sum_{n=0}^{K}(I - \mathcal{A}^*)^n\mathcal{A}_T^* f\right\|_2 &(4.55)\\
&\leq \left\|\sum_{n=0}^{K}(I - \mathcal{A}^*)^n(\mathcal{A}^* f - \mathcal{A}_T^* f)\right\|_2 + \left\|\sum_{n=K+1}^{\infty}(I - \mathcal{A}^*)^n\mathcal{A}^* f\right\|_2 &(4.56)\\
&\leq c_{\delta,\Omega,\beta}\frac{1-\left(\frac{\delta\Omega}{\pi}\right)^{K+1}}{1-\frac{\delta\Omega}{\pi}}\|f\|_{2,\beta}(1+T)^{-\beta} \\
&\quad + \left(\frac{\delta\Omega}{\pi}\right)^{K+1}\frac{1+\frac{\delta\Omega}{\pi}}{1-\frac{\delta\Omega}{\pi}}\|f\|_2 &(4.57)
\end{aligned}$$

We now construct $\tilde{f}_t(t)$ using spikes $\{t_i\}_{i:|t_i|\leq t}$ at every time t. Thus, at every time t, we have a causal decoder that uses all spikes that have already occurred. We bound the error at every time t as the following.

$$|f(t) - \tilde{f}_t(t)| \leq \sup_{\tau\in\mathbb{R}}|f(\tau) - \tilde{f}_t(\tau)| \leq \|f - \tilde{f}_t\|_2 \leq \frac{c_{\delta,\Omega,\beta}}{1-\frac{\delta\Omega}{\pi}}\|f\|_{2,\beta}(1+t)^{-\beta} \quad (4.58)$$

Here, we used the fact that $\|x\|_\infty \leq \|x\|_2 \; \forall x \in \mathcal{L}_2$ for the first inequality, and Equation 4.54 for the second inequality. The proof for Equation 4.42 follows similarly from Equation 4.57.

We note that as a new spike t_{i+1} arrives, we can calculate the new estimate as a function of the old estimate due to the following.

$$\tilde{f}^0_{t_{i+1}} = \mathcal{A}_{t_{i+1}} f = \mathcal{A}_{t_i} f + \left(\int_{t_i}^{t_{i+1}} f(\tau) d\tau \right) \text{sinc}(t - s_i) = \tilde{f}^0_{t_i} + g^0_{t_{i+1}} \tag{4.59}$$

We can carry the term $g^0_{t_{i+1}}$ forward, and track its effect on future iterations to calculate $g^k_{t_{i+1}}$ as a function of $g^{k-1}_{t_{i+1}}$, to obtain Equation 4.13. ☐

Corollary 4. *Bounded $\mathcal{L}_2$ norm: The causal decoder provided in Theorem 3, with the same assumptions and in the case of $K \rightarrow \infty$, constructs a signal $\tilde{f}_t(t)$ s.t. the $\mathcal{L}_2$ norm of the error $\|f - \tilde{f}_t\|_2 = \sqrt{\int_0^\infty |f(t) - \tilde{f}_t(t)|^2 dt}$ is bounded: $\|f - \tilde{f}_t\|_2 \leq \frac{c/\sqrt{2\beta-1}}{1-\frac{\delta\Omega}{\pi}} \|f\|_{2,\beta}$ where c is the same constant as in Theorem 3.*

Proof.

$$\sqrt{\int_0^\infty |f(t) - \tilde{f}_t(t)|^2 dt} \;\leq\; \sqrt{\int_0^\infty \left(\frac{c}{1 - \frac{\delta\Omega}{\pi}} \right)^2 \|f\|^2_{2,\beta} (1+t)^{-2\beta} dt} = \frac{c/\sqrt{2\beta - 1}}{1 - \frac{\delta\Omega}{\pi}} \|f\|_{2,\beta}$$

Here, the first inequality is due to Theorem 3, and all the constants are as defined in the same. ☐

Corollary 5. *Real-Time Reconstruction after sampling with a multiplicative function: Let the assumptions in Corollary 3 hold. If $f \in \mathcal{L}^{\Omega}_{2,\beta}$ and we receive samples of $\int_{t_i}^{t_{i+1}} f(\tau) h(\tau) d\tau$, we can construct a causal real-time decoder that reconstructs a function $\tilde{f}_t(t)$ such that*

$$|f(t) - \tilde{f}_t(t)| \leq \frac{c_{\delta,\Omega,\beta}(1+\epsilon)}{1 - \left(\frac{\delta\Omega}{\pi} + \epsilon\left(1 + \frac{\delta\Omega}{\pi}\right)\right)} \|f\|_{2,\beta} (1+t)^{-\beta} \tag{4.60}$$

, where $c_{\delta,\Omega,\beta}$ is the same as defined in Theorem 3, and ϵ is the same as defined in Corollary 3.

Proof. We use the same arguments as in the proof of Theorem 3, with the operator $\mathcal{A}_h$ as in Corollary 3. Let $c_1 = \left(\frac{\delta\Omega}{\pi} + \epsilon\left(1 + \frac{\delta\Omega}{\pi}\right)\right)$. Continuing from the equivalent of Equation 4.52, we have the following.

$$\begin{aligned}
\|f - \tilde{f}_T\|_2 &\leq \frac{1}{1-c_1}\left\|\sum_{i:|t_i|>T} f(s_i)h\mathbb{1}_{[t_i,t_{i+1}]}\right\|_2 \\
&\leq \frac{1}{1-c_1}\left\|\sum_{i:|t_i|>T} f(s_i)\mathbb{1}_{[t_i,t_{i+1}]}\right\|_2 + \left\|\sum_{i:|t_i|>T} f(s_i)(1-h)\mathbb{1}_{[t_i,t_{i+1}]}\right\|_2 \\
&\leq \frac{c_{\delta,\Omega,\beta}}{1-c_1}\|f\|_{2,\beta}(1+T)^{-\beta} + \frac{1}{1-c_1}\sqrt{\sum_{i:|t_i|>T}\int_{t_i}^{t_{i+1}} |f(s_i)|^2|1-h(\tau)|^2 d\tau} \\
&\leq \frac{c_{\delta,\Omega,\beta}}{1-c_1}\|f\|_{2,\beta}(1+T)^{-\beta} + \frac{\epsilon}{1-c_1}\sqrt{\sum_{i:|t_i|>T}\int_{t_i}^{t_{i+1}} |f(s_i)|^2 d\tau} \quad (using\,(4.11)) \\
&\leq \frac{c_{\delta,\Omega,\beta}(1+\epsilon)}{1-c_1}\|f\|_{2,\beta}(1+T)^{-\beta}
\end{aligned}$$

The rest of the proof follows as in Theorem 3. □

Chapter 5

Analyzing the Stability of the Real-Time Decoder in Feedback

5.1 Introduction

Understanding movement generation as an optimal feedback control problem is a well known concept in literature [74, 105, 101]. In these formulations, the output is usually the movement or the muscle activity, and the plant and the controller are relevant structures of the brain. However, one usually sidesteps the binary nature of neuronal encoding and treats the structures of the brain as continuous input - continuous output plants in closed loop. The binary encoding and perfect decoding of neurons has, in fact, been studied in open loop using existing neuron models as encoders [61, 65, 63], with the caveat that the decoder needs access to all of the spikes. In practical applications, we need to understand the effect of finite time binary neuronal encoding and causal decoding on the closed loop feedback control formulation. Previous work on communication in feedback with finite measurements includes [90, 91].

Here, we employ an explicit neuronal model to encode the continuous time movement signal into spikes, then study the effect of decoding a finite number of spikes on the feedback loop model as shown in Figure 5-1. Employing a dynamic model instead of a nonparametric model for neuronal encoding has the advantage that the decoder is able to obtain

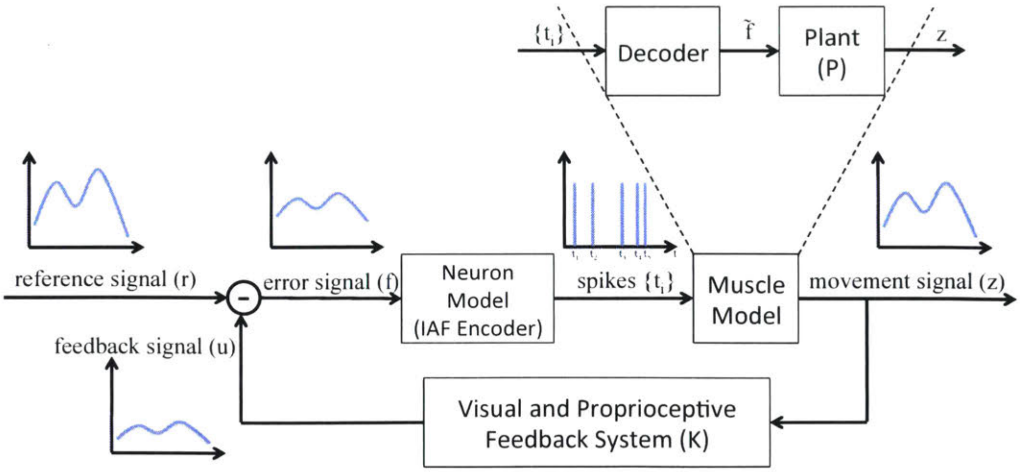

Figure 5-1: A schematic of the human motor system. The reference movement signal r provides input to a feedback loop in which the error signal drives a neuronal encoder. The spikes from the encoder directly drive the muscle model, which is decoupled in our analysis into a decoder and a plant P. The movement signal produced by the muscle model provides feedback to the reference signal, via the visual and proprioceptive feedback system (modeled by K). Our aim is to i) provide conditions for the well-posedness and stability of the feedback loop and ii) provide a reconstruction of r given a finite number of spikes $\{t_i\}$.

an approximate reconstruction of the signal with each added sample.

We limit ourselves to reference signals in the bandlimited $\mathcal{L}_2$ space. The motor neurons, here modeled as integrate and fire (IAF) neurons [54, 20], act as encoders of the error signal between the reference movement and the feedback. The resulting spikes are transformed into a smooth movement signal by the muscles. The movement information is fed back to the motor neurons via visual and proprioceptive feedback (here modeled by K). We consider that the muscle model can be decoupled into a decoder and a continuous time plant (P) in series, as we show in Figure 5-1. We use an IAF Decoder as presented in [61, 67] in the context of a neural decoder, although first presented in [26] as a reconstruction operator in the context of sampling theory. This decoder, given all spikes, perfectly reconstructs a bandlimited signal that has been fed into an IAF Encoder (see Equation (4.5)) under certain density conditions.

The main goals of this work are: i) to analyze the effect of a finite time encoder on the closed loop formulation and ii) to derive the conditions under which it is possible to

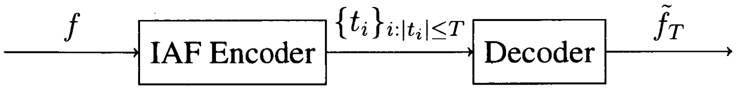

Figure 5-2: IAF Encoder and Decoder in open loop with a finite number of spikes.

reconstruct the reference signal r if we record a finite number of spikes $\{t_i\}$ as in Figure 5-1. To address these questions, we first show that the reconstruction error while decoding a finite number of spikes is bounded in open loop for bandlimited signals. We use these results to provide conditions on P and K such that the closed loop is well-posed and stable. Finally, we provide a method to reconstruct an approximation of the reference signal given a finite number of spikes $\{t_i\}$ in the closed loop. Moreover, we show that if we record all spikes $\{t_i\}$ such that $t_i \in [-T, T]$, the reconstruction error decreases as $O(T^{-\beta})$ if $r \in \mathcal{L}^{\Omega}_{2,\beta}$ (see Equation (4.2)).

The mathematical notation in Chapter 4 will be relevant in this chapter again. In Section 5.3, we consider the effect of a finite number of samples on the open loop reconstruction error for bandlimited signals. In Section 5.4, we first provide conditions for the well-posedness and stability of the feedback loop. We then provide a reconstruction method for the reference signal r given a finite number of spikes $\{t_i\}$ from the output of the IAF Encoder, and show the decay of the reconstruction error with added spikes. In Section 5.5, we show the results of numerical simulations using the reconstruction algorithm developed in this paper. We finally conclude this chapter with possible future directions in Section 5.6.

5.2 Perfect Reconstruction

We wish to reconstruct a bandlimited signal $f \in \mathcal{L}^{\Omega}_2$ while receiving all spike times $\{t_i\}_{i\in\mathcal{Z}}$, and with knowledge of the corresponding integrals $\left\{\int_{t_i}^{t_{i+1}} f(\tau)d\tau\right\}_{i\in\mathcal{Z}}$. In Chapter 4, we provided a summary of the theorem (Theorem 2), proof and algorithm for perfect reconstruction first presented in [26], since it will play a role in the subsequent analyses for an approximate reconstruction of the signal given a finite number of samples.

5.3 Reconstruction using a finite number of spikes

Let us now consider the case where we only have knowledge of a finite subset of the spikes from a bandlimited signal; let all spikes $\{t_i\}$ such that $|t_i| \leq T$ (denoted $\{t_i\}_{i:|t_i|\leq T}$) be accessible to the decoder. We want to find the error incurred by using these spikes for reconstruction, i.e. we want to find an upper bound on $||f - \tilde{f}_T||_2$, where the reconstructed function is denoted $\tilde{f}_T$ (see Figure 5-2).

Theorem 4. *Reconstruction using a finite number of consecutive samples: Given an incomplete sampling set* $\{t_i\}_{i:|t_i|\leq T}$ *and the corresponding samples* $\int_{t_i}^{t_{i+1}} f(\tau)d\tau$ *of* $f \in \mathcal{L}_2^{\Omega}$ *s.t.* $\sup_{i:|t_i|\leq T}(t_{i+1}-t_i) = \delta$ *for some* $\delta < \frac{\Omega}{\pi}$*, we can construct* $\tilde{f}_T$ *s.t.* $||f-\tilde{f}_T||_2 \leq c_{\delta,\Omega}||f||_2$*, where* $c_{\delta,\Omega}$ *depends only on the values of* Ω *and* δ*.*

Proof. Provided in Section 5.7. ☐

Note that the construction of $\mathcal{A}_T f$ only uses the timing information of the spikes $\{t_i\}_{i:|t_i|\leq T}$ and the integral thresholds $\left\{\int_{t_i}^{t_{i+1}} f(\tau)d\tau\right\}_{i:|t_i|\leq T}$.

5.4 Encoder and Decoder in Closed Loop

We now analyze the closed loop formulation of the encoder. We consider that the muscle model can be decoupled into the IAF Decoder of the form (5.25), and a plant P. The movement information z is fed back via visual and proprioceptive feedback modeled by the feedback system K, as in Figure 5-1. We first want to determine the conditions under which the feedback loop is well-posed and stable. Next, given samples of the error signal $\{t_i\}$, we would like to reconstruct the reference signal r.

We first describe the causal implementation of the IAF decoder. First note that at every time t, the decoder internally calculates an estimate of the signal using all the spikes till time t, i.e. the decoder internally has an estimate of the entire signal f given all spikes up till time t, which is $\tilde{f}_t(t)$. However, at every time t, the decoder only outputs the value of this estimate at time t; we call this signal $\hat{f}_t(t)$, the output of the causal decoder, defined as

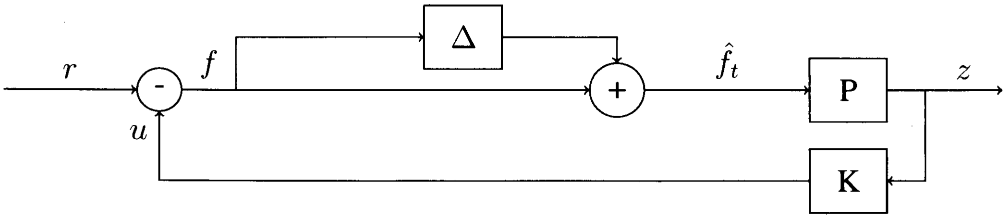

Figure 5-3: Representation of the IAF Encoder and Decoder as a multiplicative uncertainty $(1+\Delta)$ acting on the plant P.

the following.

$$\hat{f}_t(t) = \left(\sum_{n=0}^{\infty}(I-\mathcal{A})^n \mathcal{A}_t f\right)(t) \tag{5.1}$$

Note that $\hat{f}_t(t) = \tilde{f}_t(t)$ for every time $t \in \mathbb{R}$.

Although $\tilde{f}_t(t)$ is bandlimited, $\hat{f}_t(t)$ is not necessarily bandlimited, and since this signal is fed back (Figure 5-3), f is not necessarily bandlimited. Thus, we first calculate the error in decoding incurred due to a non-bandlimited f, for every time t. We denote $f_\Omega = \mathrm{sinc}_\Omega * f$.

$$\begin{aligned}
& |f(t) - \tilde{f}_t(t)| && (5.2)\\
\leq\; & \|f - \tilde{f}_t\|_\infty && (5.3)\\
\leq\; & \Bigg\| f - f_\Omega + f_\Omega - \sum_{n=0}^{\infty}(I-\mathcal{A})^n \mathcal{A}_t f_\Omega \\
+\; & \sum_{n=0}^{\infty}(I-\mathcal{A})^n \mathcal{A}_t f_\Omega - \sum_{n=0}^{\infty}(I-\mathcal{A})^n \mathcal{A}_t f \Bigg\|_\infty && (5.4)\\
\leq\; & \underbrace{\|f - f_\Omega\|_2}_{\mathrm{I}} + \underbrace{\left\| f_\Omega - \sum_{n=0}^{\infty}(I-\mathcal{A})^n \mathcal{A}_t f_\Omega \right\|_2}_{\mathrm{II}} \\
+\; & \underbrace{\left\| \sum_{n=0}^{\infty}(I-\mathcal{A})^n \mathcal{A}_t f_\Omega - \sum_{n=0}^{\infty}(I-\mathcal{A})^n \mathcal{A}_t f \right\|_\infty}_{\mathrm{III}} && (5.5)
\end{aligned}$$

Note that $I = III = 0$ if $f = f_\Omega$.

$I \leq \|f\|_2$, and $II \leq c_{\delta,\Omega}\|f\|_2$ via Equation 5.34. We now consider the third term, and we have the following error bound for $f \neq f_\Omega$.

$$\begin{aligned} III &\leq \frac{1}{1-\frac{\delta\Omega}{\pi}} \sum_{i:|t_i|\leq t} \left| \int_{t_i}^{t_{i+1}} (f - f_\Omega)(\tau) d\tau \right| && (5.6) \\ &\leq \frac{1}{1-\frac{\delta\Omega}{\pi}} \int_0^t |(f - f_\Omega)(\tau)| d\tau \\ &\leq \frac{1}{1-\frac{\delta\Omega}{\pi}} \sqrt{t} \|f - f_\Omega\|_2 \\ &\leq \frac{1}{1-\frac{\delta\Omega}{\pi}} \sqrt{t} \|f\|_2 \end{aligned}$$

Thus, $|f(t) - \tilde{f}_t(t)| \leq \left((1 + c_{\delta,\Omega}) + \frac{\sqrt{t}}{1-\frac{\delta\Omega}{\pi}}\right) \|f\|_2$.

5.4.1 Well-posedness and Stability of the Feedback Loop

We first introduce the notation used in this section. We denote an operator $M : \mathcal{L}_2 \to \mathcal{L}_2$ acting on a signal $f \in \mathcal{L}_2$ as Mf. In full generality, M is allowed to be nonlinear and time varying. Note that if the operator in question is time invariant, we can express the action of the operator in terms of convolution in the time domain or multiplication in the Fourier domain. We define the $\mathcal{L}_2$-Induced norm of M as $\|M\|_{2-ind} = \|M\|_\infty = \sup_{x\neq 0} \frac{\|Mx\|_2}{\|x\|_2}$. This is a standard abuse of notation utilized in control theory, and for more details, we refer the reader to [117, 21].

In order to determine well-posedness and stability of the feedback loop despite the approximate reconstruction of the error signal, we first express the feedback loop as in Figure 5-3, where Δ is an operator acting on $f \in \mathcal{L}_2$, defined as the following.

$$\begin{aligned} (\Delta f)(t) &= f(t) - \hat{f}_t(t) && (5.7) \\ &= \left(\sum_{n=0}^{\infty} (I - \mathcal{A})^n (\mathcal{A}f - \mathcal{A}_t f) \right)(t) && (5.8) \end{aligned}$$

Next, we calculate the truncated $\mathcal{L}_2$ norm incurred by the Δ operator.

$$\left(\int_0^T |(\Delta f)(t)|^2 dt\right)^{\frac{1}{2}} \tag{5.9}$$

$$= \left(\int_0^T |f(t) - \hat{f}_t(t)|^2 dt\right)^{\frac{1}{2}} \tag{5.10}$$

$$= \left(\int_0^T |f(t) - \tilde{f}_t(t)|^2 dt\right)^{\frac{1}{2}} \tag{5.11}$$

$$\leq \left(\int_0^T \left|(1 + c_{\delta,\Omega} + \frac{\sqrt{t}}{1 - \frac{\delta\Omega}{\pi}})\|f\|_2\right|^2 dt\right)^{\frac{1}{2}} \tag{5.12}$$

$$= \left((1 + c_{\delta,\Omega})^2 T + \frac{4(1 + c_{\delta,\Omega})T^{1.5}}{3\left(1 - \frac{\delta\Omega}{\pi}\right)} + \frac{T^2}{2\left(1 - \frac{\delta\Omega}{\pi}\right)^2}\right)^{\frac{1}{2}} \cdot\|f\|_2 \tag{5.13}$$

We define $\gamma = \left((1 + c_{\delta,\Omega})^2 + \frac{4(1+c_{\delta,\Omega})}{3\left(1-\frac{\delta\Omega}{\pi}\right)} + \frac{1}{2\left(1-\frac{\delta\Omega}{\pi}\right)^2}\right)^{\frac{1}{2}}$. We now have two upper bounds depending on the value of T:

$$\|(\Delta f)\mathbb{1}_{[0,T]}\|_2 \leq \begin{cases} \gamma\|f\|_2 & T < 1 \\ \gamma T\|f\|_2 & T \geq 1 \end{cases} \tag{5.14}$$

The representation of the IAF Encoder and Decoder as $f + \Delta f$ allows us to treat the effect of the truncated reconstruction as an uncertainty for the plant P, and thus provide conditions on stability using concepts in robust control.

Theorem 5. *Let K be stabilizing for the nominal plant P, i.e., by assumption, K and $(1 + KP)^{-1}$ are stable. The closed loop in Figure 5-3 with Δ as in (5.8) is bounded-input bounded-output (BIBO) stable if*

$$\left\|(1 + KP)^{-1}KP\,[1 \quad \sqrt{2}S]\right\|_\infty < \frac{1}{\sqrt{2}\gamma} \tag{5.15}$$

where $S(s) = \frac{1}{s}$ in the Laplace domain.

Proof. Provided in Section 5.7. □

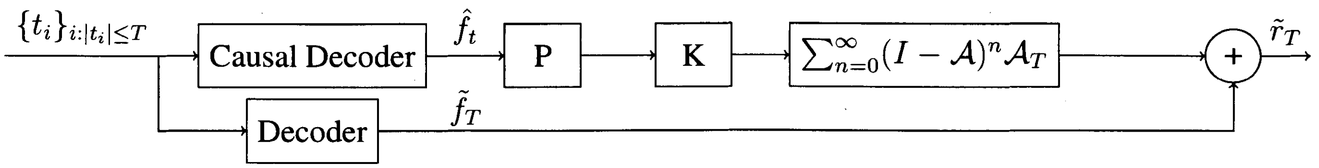

Figure 5-4: A schematic for the approximate reconstruction of $r(t)$ given $\{t_i\}_{i:|i|\leq T}$.

5.4.2 Reconstruction of the Reference Signal in Closed Loop

By observing the spikes $\{t_i\}_{i:|t_i|\leq T}$, we can reconstruct an approximation of the reference signal $r \in \mathcal{L}_2^{\Omega}$ driving the feedback loop.

Proposition 1. *Reconstruction of the reference signal in feedback: Given $\{t_i\}_{i:|t_i|\leq T}$ in the feedback loop shown in Figure 5-1, and with P and K stable, we can reconstruct $\tilde{r}_T$ as shown in Figure 5-4 for $r \in \mathcal{L}_2^{\Omega}$, with $\|r - \tilde{r}_T\|_2 \leq c_{\delta,\Omega}\|r\|_2$, with $c_{\delta,\Omega}$ as in Theorem 4. Moreover, if $r \in \mathcal{L}_{2,\beta}^{\Omega}$, $\|r - \tilde{r}_T\|_2 = O(T^{-\beta})$.*

Proof. Provided in Section 5.7. ☐

If we record a finite number of spikes from the encoder in closed loop, we can have an approximate reconstruction of the reference movement signal, where the approximation error decreases polynomially with the amount of time for which the spikes are recorded.

5.5 Numerical Simulations

In general, the constants $c_{\delta,\Omega}$ and $c_{\delta,\Omega,\beta}$ are not easy to calculate. Here, we provide a method to calculate an upper bound on $c_{\delta,\Omega}$ for a given pair $\{\delta,\Omega\}$. We want to construct a function $p \in \mathcal{L}_1$ such that $\hat{p}(\omega) = 1\ \forall\omega \in [-\Omega,\Omega]$. One such function is defined by $p_c(t) = \frac{\sqrt{2}}{\pi^{3/2}t^2}(\cos(\Omega t) - \cos((\Omega+\pi)t))$, whose Fourier transform is given by the following.

$$\hat{p}_c(\omega) = \begin{cases} 1 & |\omega| \leq \Omega \\ \frac{\Omega+\pi-|\omega|}{\pi} & \Omega < |\omega| < \Omega+\pi \\ 0 & o.w. \end{cases} \tag{5.16}$$

The maximum value of $p_c(t)$ is given by $p_c^{max} = \left(\Omega + \frac{\pi}{2}\right)\sqrt{\frac{2}{\pi}}$, and the envelope to $|p_c(t)|$ is given by $\bar{p}_c(t) = \min\left(\frac{2\sqrt{2}}{\pi^{3/2}t^2}, p_c^{max}\right)$. Since this envelope is monotonically decreasing, we can calculate the following upper bound on $\inf_p \|p^{\#}\|_1$.

$$\inf_p \|p^{\#}\|_1 \leq \|p_c^{\#}\|_1 \leq \|\bar{p}_c\|_1 + 2\delta p_c^{max} \tag{5.17}$$

This gives us an upper bound on $c_{\delta,\Omega}$; $c_{\delta,\Omega} \leq \frac{\|p_c^{\#}\|_1}{1-\frac{\delta\Omega}{\pi}}$. For example, $c_{0.2,4} \leq 10.45$.

We simulate the feedback loop shown in Figure 5-1 for three different reference signals $\{r_D\}_{D=2,3,4}$ defined as

$$r_D(t) = \left(\frac{\Omega}{\pi}\right)^D \sum_{i=1}^{5} c_k \left(\operatorname{sinc}\left(2(t-d_k)\right)\right)^D \tag{5.18}$$

, where c_k's and d_k's were picked uniformly at random from the interval $[0,5]$ and $[0,3]$ respectively. Note that $r_D \in \mathcal{L}_{2,\beta_D}^{\Omega_D}$, where $\Omega_D = 2D$, and $\beta_D = D-1$. We simulated signals for $t \in [0,20]$ with a stepsize of 10^{-4}. All simulations were performed using MATLAB R2013a. The integrals $\{q_i\}$ were usually equal to 0.1, but were chosen more carefully at low values of the signal in order to ensure the density condition. For each simulation experiment, the decoder estimated a signal $\tilde{f}_t$, but the output of the causal decoder was called $\hat{f}_t(t)$. We considered the plant $P(s) = \frac{s}{(s+2)^2}$ and the feedback system a simple gain $K(s) = k$. For the values of $\{\delta, \Omega\} = \{0.2, 4\}$, the estimated value for γ is 12.29. The sufficient condition for stability we derived in Theorem 5 is met with $k = 0.15$.

In Figure 5-5, we show the simulation for the aforementioned system and signals. We also tested the system for higher values of δ and k, for which the feedback was numerically observed to be stable for the signals we considered. We show the results in Figure 5-5. We can see that the reconstruction is better for higher values of D, since the signal decays faster. The reconstruction is seen to be slightly better for low values of k. For all values of T and D, we noticed a good local reconstruction, i.e. for $|t| \leq T$, even for low values of T.

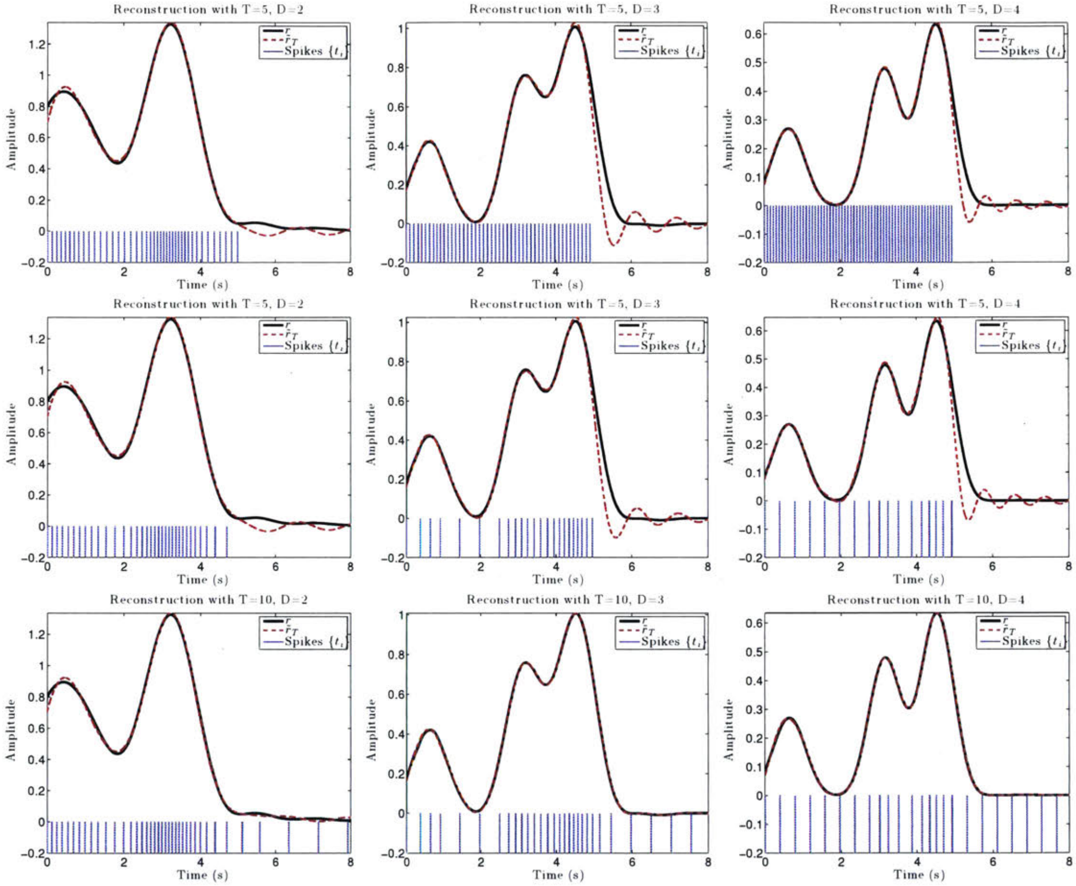

Figure 5-5: Reconstruction using the method described in Section 5.4.2, while varying T, for $D = 2$ (left column), $D = 3$ (middle column), and $D = 4$ (right column). The parameters are as follows: $\{k = 0.15, \delta < 0.2\}$ for the top row, $\{k = 2, \delta \text{ s.t. } \frac{\delta\Omega}{\pi} < 1\}$ for the middle and the bottom rows. The IAF Decoder has access to all spikes $\{t_i\}$ s.t. $t_i \in [-T, T]$. D controls the decay of the signal, and is defined in the text.

5.6 Conclusions and Future Work

In this chapter, we analyze the effect of a finite time IAF encoding model in a closed loop formulation, and provided an algorithm for the reconstruction of the reference signal given a finite subset of the samples from the IAF Encoder.

We first analyze the effect of a finite number of spikes $\{t_i\}_{i:|t_i|\leq T}$ on the decoding process, with the encoder and decoder in open loop as in Figure 5-2. We show that if $f \in \mathcal{L}_2^{\Omega}$, then the $\mathcal{L}_2$ error between the reconstruction $\tilde{f}_T$ and f is bounded. Moreover, we can show that if $f \in \mathcal{L}_{2,\beta}^{\Omega}$, then the reconstruction error $\|f - \tilde{f}_T\|_2$, decreases polynomially with T (using concepts presented in Proposition 1).
Next, we examine the effect of the encoder and the causal implementation of the decoder on the feedback loop. We provide conditions on the plant P and feedback system K for the well-posedness and stability of the closed loop despite the approximate reconstruction of the encoded signal f. We also show that, if $r \in \mathcal{L}_{2,\beta}^{\Omega}$ and $\{P, K\}$ satisfy certain conditions, then it is possible to reconstruct an approximation of r given all spikes $\{t_i\}$ in $[-T, T]$ such that the $\mathcal{L}_2$ reconstruction error decreases polynomially with T, i.e. as $O(T^{-\beta})$.

Throughout this paper, we had a density condition on the spikes, i.e. $\sup(t_{i+1} - t_i) = \delta$ for some $\delta < \frac{\pi}{\Omega}$. However, our sampling is directly dependent on the integral thresholds q_i's, whereas the sampling times t_i's and thus δ depend nontrivially on these thresholds. It is conceivable to *a priori* initialize a set of q_i's such that the density condition holds, given additional conditions on r, P and K. Further work is needed to identify such a set of conditions. Moreover, even if the density condition is not met in some cases, we have seen the algorithm to be robust to 'missing spikes' through numerical experiments, and in the future we would like to identify the exact effect of this phenomenon on the stability of the feedback loop as well as on the reconstruction error.

The encoder here is based on the IAF neuron model, which we showed in Chapter 2 to emulate the firing of motor neurons in a feedback setup. Although the setup in Chapter 2 showed K to be in the forward loop, the results discussed here can easily be extended to that setup. Further experiments would need to be performed in order to validate the theory discussed in this chapter. Specifically, with a similar experimental paradigm as discussed in the conclusion of Chapter 3, we can first apply system identification methods to find K and q, and we can then use recorded motor neuron spikes and directly drive the real-time decoder and prosthetic device with desired movement signals as specified in the experiment. Instead of just showing the target to be reached, one can specify the trajectory that needs to be followed as well, to have more complicated shapes for r. We can then analyze the time taken to reconstruct r from the spikes, as a function of Ω, in order to validate this theory.

The stable implementation of a binary encoder and a causal decoder in a feedback system gives us some insight into a possible method of neuronal decoding in the human body, with the systems P and K being tunable in order to reflect more realistic models of the muscles and the visual and proprioceptive systems, respectively. Moreover, the accurate reconstruction of the driving signal from neuronal spikes leads us to believe that the concepts developed in this paper may be used to drive further research in prosthetic control via neuronal decoding.

5.7 Proofs for Chapter 5

Theorem 4. *Reconstruction using a finite number of consecutive samples: Given an incomplete sampling set* $\{t_i\}_{i:|t_i|\leq T}$ *and the corresponding samples* $\int_{t_i}^{t_{i+1}} f(\tau)d\tau$ *of* $f \in \mathcal{L}_2^\Omega$ *s.t.* $\sup_{i:|t_i|\leq T}(t_{i+1}-t_i) = \delta$ *for some* $\delta < \frac{\Omega}{\pi}$*, we can construct* $\tilde{f}_T$ *s.t.* $||f-\tilde{f}_T||_2 \leq c_{\delta,\Omega}||f||_2$*, where* $c_{\delta,\Omega}$ *depends only on the values of* Ω *and* δ.

Proof. We first define a local maximum function on f [25]:

$$f^{\#}(t) = \sup_{|u|\leq\delta} |f(t+u)| \tag{5.19}$$

Note the following two properties of $f^{\#}(t)$ for $f \in \mathcal{L}_2^\Omega$, with a function $p(t)$ such that $\hat{p}(\omega) = 1$ for $\omega \in [-\Omega, \Omega]$, and $p \in \mathcal{L}_1$.

$$\begin{aligned} |\sum_{i=1}^{\infty} f(s_i)\mathbb{1}_{[t_i,t_{i+1}]}(t)| &\leq f^{\#}(t) \text{ pointwise} && (5.20) \\ f^{\#}(t) = (f*p)^{\#}(t) &\leq (|f|*p^{\#})(t) && (5.21) \end{aligned}$$

As a direct consequence of equation (5.21), we obtain the following bound on $||f^{\#}||_2$. We denote $\inf_p ||p^{\#}||_1$ by $d_{\delta,\Omega}$.

$$||f^{\#}||_2 \leq \inf_p ||p^{\#}||_1 ||f||_2 := d_{\delta,\Omega}||f||_2 \tag{5.22}$$

We define two operators adjoint to each other for $f \in \mathcal{L}_2^{\Omega}$.

$$\begin{aligned} \mathcal{A}_T f &= \sum_{i:|t_i|\leq T} \int_{t_i}^{t_{i+1}} f(\tau)d\tau \ \mathrm{sinc}_{\Omega}(t - s_i) & (5.23) \\ \mathcal{A}_T^* f &= \sum_{i:|t_i|\leq T} f(s_i)(\mathrm{sinc}_{\Omega} * \mathbb{1}_{[t_i,t_{i+1}]}) & (5.24) \end{aligned}$$

We consider that after the first approximation $\mathcal{A}_T f$ with a finite number of spikes, we can construct $\{t_i\}_{i:|t_i|>T}$ such that $\sup_{i:|t_i|>T}(t_{i+1} - t_i)$ is less than the required δ. Thus we can construct an operator $\mathcal{A}$ as long as it is not acting directly on f. We define $\tilde{f}_T$ as:

$$\tilde{f}_T = \sum_{n=0}^{\infty}(I - \mathcal{A})^n \mathcal{A}_T f \tag{5.25}$$

To derive $||f - \tilde{f}_T||_2$ for $f \in \mathcal{L}_2^{\Omega}$, we first note that the error incurred using a finite number of spikes is the same as the error in the adjoint space, i.e.

$$\begin{aligned} ||f - \tilde{f}_T||_2 &= \left\| f - \sum_{n=0}^{\infty}(I - \mathcal{A})^n \mathcal{A}_T f \right\|_2 & (5.26) \\ &= \left\| f - \sum_{n=0}^{\infty}(I - \mathcal{A}^*)^n \mathcal{A}_T^* f \right\|_2 & (5.27) \end{aligned}$$

We can thus work exclusively with the adjoint operators $\mathcal{A}^* f$ and $\mathcal{A}_T^* f$ in order to derive $||f - \tilde{f}_T||_2$. The following calculation is similar to that for the truncation error provided in

[12].

$$
\begin{aligned}
\|f - \tilde{f}_T\|_2 &= \left\| \sum_{n=0}^{\infty} (I - \mathcal{A}^*)^n (\mathcal{A}^* f - \mathcal{A}_T^* f) \right\|_2 && (5.28) \\
&\leq \sum_{n=0}^{\infty} \|(I - \mathcal{A}^*)^n (\mathcal{A}^* f - \mathcal{A}_T^* f)\|_2 && (5.29) \\
&\leq \sum_{n=0}^{\infty} \left(\frac{\delta\Omega}{\pi}\right)^n \|\mathcal{A}^* f - \mathcal{A}_T^* f\|_2 && (5.30) \\
&= \frac{1}{1 - \frac{\delta\Omega}{\pi}} \left\| \sum_{i:|t_i|>T} f(s_i) \mathbb{1}_{[t_i, t_{i+1}]} * \mathrm{sinc}_\Omega \right\|_2 && (5.31) \\
&\leq \frac{1}{1 - \frac{\delta\Omega}{\pi}} \left\| \sum_{i:|t_i|>T} f(s_i) \mathbb{1}_{[t_i, t_{i+1}]} \right\|_2 && (5.32) \\
&\leq \frac{1}{1 - \frac{\delta\Omega}{\pi}} \left\| f^{\#} \mathbb{1}_{\mathbb{R} \setminus [-T,T]} \right\|_2 && (5.33) \\
&\leq \frac{d_{\delta,\Omega}}{1 - \frac{\delta\Omega}{\pi}} \|f\|_2 && (5.34)
\end{aligned}
$$

We have $\|f - \tilde{f}_T\|_2 \leq c_{\delta,\Omega} \|f\|_2$, where $c_{\delta,\Omega} = \frac{d_{\delta,\Omega}}{1 - \frac{\delta\Omega}{\pi}}$ only depends on δ and Ω. □

Theorem 5. *Let K be stabilizing for the nominal plant P, i.e., by assumption, K and $(1 + KP)^{-1}$ are stable. The closed loop in Figure 5-3 with Δ as in (5.8) is bounded-input bounded-output (BIBO) stable if*

$$
\left\| (1 + KP)^{-1} KP \, [1 \quad \sqrt{2}S] \right\|_\infty < \frac{1}{\sqrt{2}\gamma} \qquad (5.35)
$$

, where $S(s) = \frac{1}{s}$ in the Laplace domain.

Proof. From Equation (5.14), we see the upper bound of $\|(\Delta f)\mathbb{1}_{[0,T]}\|_2$ is different for the two cases $T < 1$ and $T \geq 1$. These two cases need to be dealt with separately, and for this reason, we introduce a separate uncertainty operator for each case, $\bar{\Delta}_1$ and $\bar{\Delta}_2$ respectively, with $\bar{\Delta} = \left[\begin{smallmatrix} \bar{\Delta}_1 \\ \bar{\Delta}_2 \end{smallmatrix}\right]$. We define the two arbitrary operators with the following constraint; for $i \in \{1, 2\}$, $\bar{\Delta}_i : \mathcal{L}_2 \to \mathcal{L}_2$ such that $\|\bar{\Delta}_i x\|_2 \leq \gamma \|x\|_2 \, \forall x \in \mathcal{L}_2$, or equivalently $\|\bar{\Delta}_i\|_\infty \leq \gamma$. We consider the larger class of uncertainties $[1 \quad \sqrt{2}S]\bar{\Delta}$, and show that this satisfies the same conditions as Δ. Thus, if stability is achieved for $[1 \quad \sqrt{2}S]\bar{\Delta}$, it will be achieved for Δ.

- *Case 1: $T < 1$* We have $\|(\bar{\Delta}_1 f)\mathbb{1}_{[0,T]}\|_2 \leq \|(\bar{\Delta}_1 f)\|_2 \leq \gamma \|f\|_2$. Thus, $\bar{\Delta}_1$ satisfies the same constraints as Δ for $T < 1$.

- *Case 2: $T \geq 1$* Denote $f_2(t) = (\bar{\Delta}_2 f)(t)$, and $u(t)$ a unit step, i.e. the impulse response of S.

$$\|(S\bar{\Delta}_2 f)\mathbb{1}_{[0,T]}\|_2 \tag{5.36}$$

$$= \left(\int_0^T |(f_2 * u)(t)|^2 \, dt \right)^{\frac{1}{2}} \tag{5.37}$$

$$\leq \left(\int_0^T \left| \int_0^\infty f_2(\tau) u(t-\tau) d\tau \right|^2 dt \right)^{\frac{1}{2}} \tag{5.38}$$

$$\leq \left(\int_0^\infty |f_2(\tau)|^2 d\tau \int_0^\infty \int_0^T |u(t-\tau)|^2 dt d\tau \right)^{\frac{1}{2}} \tag{5.39}$$

$$= \left(\int_0^\infty |f_2(\tau)|^2 d\tau \int_0^\infty (T-\tau) u(T-\tau) d\tau \right)^{\frac{1}{2}} \tag{5.40}$$

$$\leq \frac{\gamma}{\sqrt{2}} T \|f\|_2 \tag{5.41}$$

Thus, $\sqrt{2}S\bar{\Delta}_2$ satisfies the same constraints as Δ for $T \geq 1$.

We have shown that $[1 \quad \sqrt{2}S]\bar{\Delta}$ adequately captures the uncertainty in Δ. We now express constraints on K and P such that the feedback loop is stable for the uncertainty set $\bar{\Delta}$ s.t. $\|\bar{\Delta}\|_\infty = \left\| \left[\begin{smallmatrix} \bar{\Delta}_1 \\ \bar{\Delta}_2 \end{smallmatrix} \right] \right\|_\infty \leq \sqrt{2}\gamma$. The condition in Equation (5.35) follows from the small gain theorem [117, 21], with the plant having a multiplicative uncertainty in the form of $(1 + [1 \quad \sqrt{2}S]\bar{\Delta})$. Note that the uncertainty does not need to be linear or time invariant for the small gain theorem to apply.

Here, we provide a brief exposition of the reason that the condition in Equation (5.35) is sufficient for BIBO stability. For more details, refer to [117, 21]. Since we have obtained an equivalent uncertainty set $\bar{\Delta}$, we will write our signals as a function of this operator. We first write r as a function of f (Figure 5-3).

$$
\begin{aligned}
r &= f + (KP(1 + [1 \;\; \sqrt{2}S]\bar{\Delta}))f && (5.42)\\
&= (1 + KP)(1 + (1 + KP)^{-1}KP[1 \;\; \sqrt{2}S]\bar{\Delta})f && (5.43)
\end{aligned}
$$

$(1+KP)^{-1}$ is stable by assumption. For $(1+(1+KP)^{-1}KP[1 \;\; \sqrt{2}S]\bar{\Delta})$ to be invertible, we need $\|(1+KP)^{-1}KP[1 \;\; \sqrt{2}S]\bar{\Delta}\|_\infty < 1$. We know that $\|\bar{\Delta}\|_\infty \leq \sqrt{2}\gamma$, and using the assumption in Equation (5.35), we have that

$$
\begin{aligned}
&\|(1 + KP)^{-1}KP[1 \;\; \sqrt{2}S]\bar{\Delta}\|_\infty && (5.44)\\
&\leq \;\; \|(1 + KP)^{-1}KP[1 \;\; \sqrt{2}S]\|_\infty \|\bar{\Delta}\|_\infty && (5.45)\\
&< \;\; \frac{1}{\sqrt{2}\gamma} \cdot \sqrt{2}\gamma = 1 && (5.46)
\end{aligned}
$$

Thus, the interconnection is BIBO stable. □

Proposition 1. *Reconstruction of the reference signal in feedback: Given* $\{t_i\}_{i:|t_i| \leq T}$ *in the feedback loop shown in Figure 5-1, and with* P *and* K *stable, we can reconstruct* $\tilde{r}_T$ *as shown in Figure 5-4 for* $r \in \mathcal{L}_2^\Omega$*, with* $\|r - \tilde{r}_T\|_2 \leq c_{\delta,\Omega}\|r\|_2$*, with* $c_{\delta,\Omega}$ *as in Theorem 4. Moreover, if* $r \in \mathcal{L}_{2,\beta}^\Omega$*,* $\|r - \tilde{r}_T\|_2 = O(T^{-\beta})$.

Proof. Firstly, we can construct $\tilde{f}_T$ using the samples as in (5.25). Next, we note the following relation due to the feedback loop.

$$
\begin{aligned}
\tilde{f}_T(t) &= \left(\sum_{n=0}^{\infty}(I - \mathcal{A})^n \mathcal{A}_T f\right)(t) && (5.47)\\
&= \left(\sum_{n=0}^{\infty}(I - \mathcal{A})^n \mathcal{A}_T (r - KP\hat{f}_t)\right)(t) && (5.48)
\end{aligned}
$$

Note that we can construct $\hat{f}_t(t)$ using the spikes $\{t_i\}_{i:|t_i| \leq t}$ for $t \in [0, T]$. Since the operators $\mathcal{A}$ and $\mathcal{A}_T$ are additive for a given sampling set $\{t_i\}$, i.e. $\mathcal{A}_T(f + g) = \mathcal{A}_T f + \mathcal{A}_T g \; \forall (f, g) \in \mathcal{L}_2$, we can construct $\tilde{r}_T = \sum_{n=0}^{\infty}(I - \mathcal{A})^n \mathcal{A}_T r$ from our spikes in the following way, also shown in Figure 5-4. Note that we need P and K to be stable for $\tilde{r}_T$ to be bounded.

$$\tilde{r}_T(t) = \tilde{f}_T(t) + \left(\sum_{n=0}^{\infty}(I - \mathcal{A})^n \mathcal{A}_T K P \hat{f}_t\right)(t) \tag{5.49}$$

Similarly to equation (5.34), this approximation of r is such that

$$||r - \tilde{r}_T||_2 \leq c_{\delta,\Omega}||r||_2 \tag{5.50}$$

We will now show that, if $r(t)$ is in the polynomially weighted $\mathcal{L}_2$ space, i.e. $r \in \mathcal{L}_{2,\beta}^{\Omega}$ as defined in (4.2), then our reconstruction error decreases polynomially with added spikes. The following calculation is similar to that provided in [12].

Firstly, similar to the arguments in the proof of Theorem 4, we obtain the following bound on the $\mathcal{L}_{2,\beta}$ norm of the local maximum function (5.19), using a function $p_\alpha(t)$ such that $\hat{p}_\alpha(\omega) = 1$ for $\omega \in [-\Omega, \Omega]$, and $p_\alpha \in \mathcal{L}_{1,\alpha}$, for some $\alpha \geq \beta$.

$$||r^{\#}||_{2,\beta} \leq \inf_{p_\alpha} ||p_\alpha^{\#}||_{1,\alpha}||r||_{2,\beta} \tag{5.51}$$

We denote $\inf_{p_\alpha} ||p_\alpha^{\#}||_{1,\alpha}$ for some $\alpha \geq \beta$ by $d_{\delta,\Omega,\beta}$.
We can now calculate the approximation error of $r \in \mathcal{L}_{2,\beta}^{\Omega}$. Note that we obtain the first inequality as in (5.33).

$$\begin{aligned}
& ||r - \tilde{r}_T||_2 && (5.52)\\
\leq\ & \frac{1}{1 - \frac{\delta\Omega}{\pi}} \left|\left|r^{\#}\mathbb{1}_{\mathbb{R}\setminus[-T,T]}\right|\right|_2 && (5.53)\\
=\ & \frac{1}{1 - \frac{\delta\Omega}{\pi}} \left|\left|r^{\#}\mathbb{1}_{\mathbb{R}\setminus[-T,T]}(1 + |t|)^{\beta}(1 + |t|)^{-\beta}\right|\right|_2 && (5.54)\\
\leq\ & \frac{1}{1 - \frac{\delta\Omega}{\pi}} \left|\left|r^{\#}\right|\right|_{2,\beta} \sup_{t\in\mathbb{R}\setminus[-T,T]} (1 + |t|)^{-\beta} && (5.55)\\
\leq\ & \frac{d_{\delta,\Omega,\beta}}{1 - \frac{\delta\Omega}{\pi}} ||r||_{2,\beta} (1 + T)^{-\beta} && (5.56)
\end{aligned}$$

Let $\frac{d_{\delta,\Omega,\beta}}{1-\frac{\delta\Omega}{\pi}}$ be denoted by $c_{\delta,\Omega,\beta}$, which only depends on δ, Ω and β. Thus, for $r \in \mathcal{L}_{2,\beta}^{\Omega}$, the $\mathcal{L}_2$ error decreases as $O(T^{-\beta})$ as T increases, i.e. as we have more spikes. □

Chapter 6

Conclusion and Future Work

6.1 Conclusions

This thesis focuses on the regime of fast movements in sensorimotor control. Specifically, we accomplished two goals:

1. We built a model of movement generation that is able to reproduce properties of spiking motor neurons, as well as recreate typical movement trajectories for simple movements. Moreover, this model encompasses the regime of fast movements, i.e. we capture the phenomena that occurs during the tracking of periodic fast movements, specifically, overshoot, undershoot and skipping of cycles.
2. In the BMI context, we designed a decoder for an integrate-and-fire encoding neuron model that provides a real-time estimate of the input signal given the spike times, and importantly, we can show that the reconstruction error decreases with time. We then provided conditions on the sensorimotor feedback system such that this real-time decoder is stable during reconstruction. We also provided means to reconstruct the reference signal from the spike times while in feedback.

6.1.1 Cutoff Frequency for the Real-Time Decoder

We can ask the question whether the real-time decoder provided in Chapter 4 also follows the concepts in Chapter 3, i.e. whether there exists a cutoff frequency ω_c such that

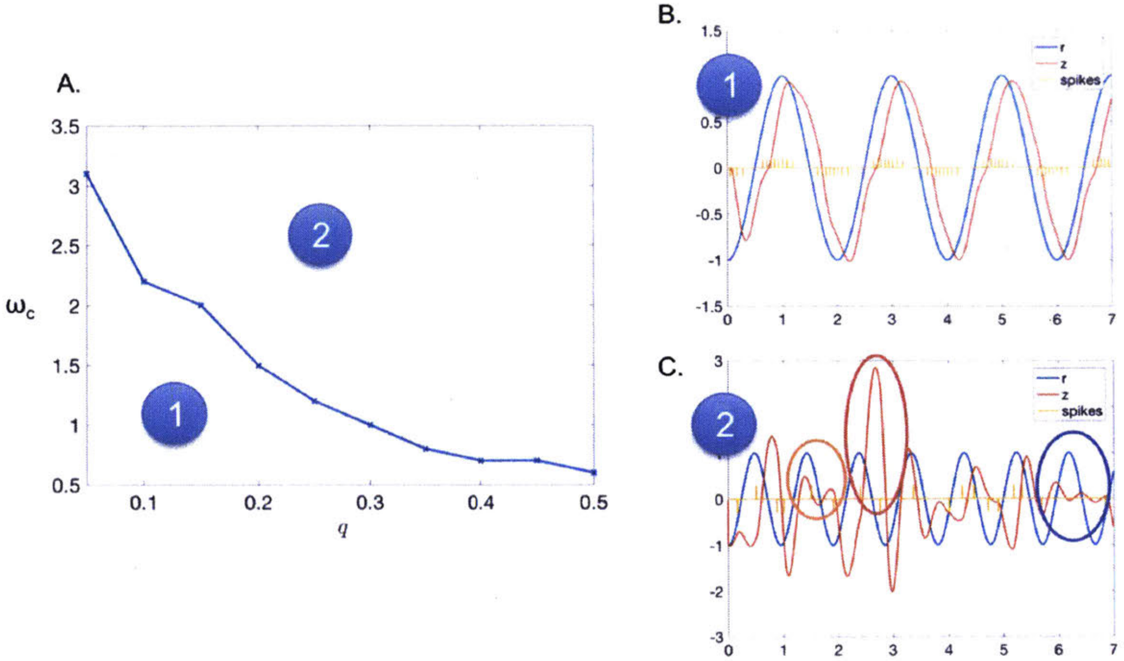

Figure 6-1: A. Cutoff frequency ω_c as a function of the threshold parameter q for the Real-Time Decoder as in Chapter 4, with $B = 2$; B. Results for $q = 0.1$, $\omega = 0.5 < \omega_c$; C. Results for $q = 0.3$, $\omega = 1.05 > \omega_c$. Here, we see evidence of undesirable phenomena as in Chapter 2, i.e., overshoot (red circle), undershoot (orange circle), and skipped cycles (blue circles).

we may see subharmonic oscillations for movements faster than this frequency. This is not evident since we showed all results in Chapter 3 for linear 'decoders', i.e. LTI systems that produce the same response at each spike. Note that linear decoders including firing rate decoders also fall in this regime, with the analyses following exactly as in Chapter 3. Here, we show in simulation that similar concepts hold for the real-time decoder, which produces a more accurate estimate of the encoding signal after every spike, i.e., a different response at every spike (time varying system). Although we are not able to show whether subharmonic oscillations as defined in Chapter 3 exist or not, we are able to show in simulation that as the frequency of oscillation increases, the same undesirable phenomena discussed in Chapter 2 exist, i.e., overshoot, undershoot, and skipped cycles. There is a cutoff frequency past which we see skipped cycles, and we show in Figure 6-1A this cutoff frequency ω_c as a function of the spiking threshold q, with model parameters as in Chapter 2. We also show in Figure 6-1B evidence of skipped cycles at a high frequency $\omega > \omega_c$. Intuitively, as long as the spiking signal is being low-pass filtered, even if the decoder is a time varying system, it should follow similar concepts as in Chapter 3, though proving this rigorously is beyond the scope of this thesis. Thus, the concept of a cutoff frequency is a general one - with decoders and prosthetic devices also falling in this paradigm.

6.1.2 Discussion on Simplified Models

Throughout this thesis, we utilize the power of simplified abstract models in order to derive the theoretical results. The utility in our case is twofold: (a) to observe and prove the existence of phenomena that may be much more difficult to prove in a more complicated nonlinear model, and (b) to design controllers for stabilization of dynamics incurred due to nonlinearities. In fact, in the world of control systems, one usually uses simple low-order models in order to design controllers; one famous example is the design of a controller to stabilize the dynamics of an airplane; this uses just a second-order model of the airplane. Our goal as theoreticians is to simplify the dynamics to the 'correct' degree that leads us to insights, without compromising on the actual effects seen. One of the important next steps is to validate the simplified model, or be able to have a path going forward to show that the results hold in face of more complex systems; and this is discussed below.

- **Using an IAF model for neural activity.** Although the IAF model provides a clear and computable cutoff frequency above which we see undesirable phenomena, do the simplifications outweigh the utility? Would it be reasonable to demand a fit to this kind of model for motor neuron activity? Moreover- how do we go from a single neuron model to a network of motor neurons all innervating the same muscle? In fact, the threshold nonlinearity represented by the IAF may be a manifestation of a systems-level phenomenon. One of the pieces of evidence lies in the reproduction of observed undesirable phenomena (skipping of cycles, undershoot, overshoot) past the cutoff frequency, while another piece of evidence is the successful modeling of movements using very similar threshold nonlinearities [28, 71, 72, 77, 81, 111, 37, 24]. It is, however, entirely possible that these phenomena arise from a different nonlinearity, and further experimental studies need to be performed in order to validate this model.

Some experimental and algorithmic ideas in order to test this model are detailed in the next section.

- **Using a second-order model for the musculoskeletal system.** It is important to note that this model, although discussed and motivated in detail in Chapter 2, is still a simplified model of the musculoskeletal system. It is only valid in certain regimes, and various highly sophisticated models of the musculoskeletal dynamics have been utilized in the past in different studies [54, 45, 116]. Our results in Chapters 3-5 hold for any low-pass LTI model for musculoskeletal dynamics; they hold for higher order models than the one we considered in Chapter 2. However, many of the muscle models that accurately describe musculoskeletal activity across several regimes are either time varying or nonlinear in nature [45, 59, 116]. These models in particular would not fall in the scope of this thesis, but in general, it is possible to encompass bounded nonlinearities in an uncertainty block as described below.

- **Using deterministic models for neural and musculoskeletal activity.** Although the theory as well as the algorithms presented in this thesis have concerned purely deterministic models for both neural activity and musculoskeletal system, we believe that the addition of stochastic models should not change the results greatly, depending on the type and amplitude of noise. One way to think about noise in threshold models is to express the thresholds themselves as some baseline plus additive noise, i.e. $q_i + \epsilon_i$, with ϵ_i arising from a uniform or Gaussian distribution with some amplitude σ.
  In the first part of this thesis, the concept of a cutoff frequency past which we may see skipped cycles, would still hold in the face of stochastic threshold model for neural activity. These skipped cycles may be transitory in the face of stochastic thresholds, but the concept of the cutoff frequency would still hold, though the value would now depend on the level of noise in the thresholds, i.e. the parameter σ. If the noise is modeled as additive noise on the signal, the same concepts apply. In fact, it can be shown that these two modalities are equivalent [66]. In the second part of this thesis, the stability of the feedback loop can be ensured in the face of stochastic models, using an uncertainty block as described below.

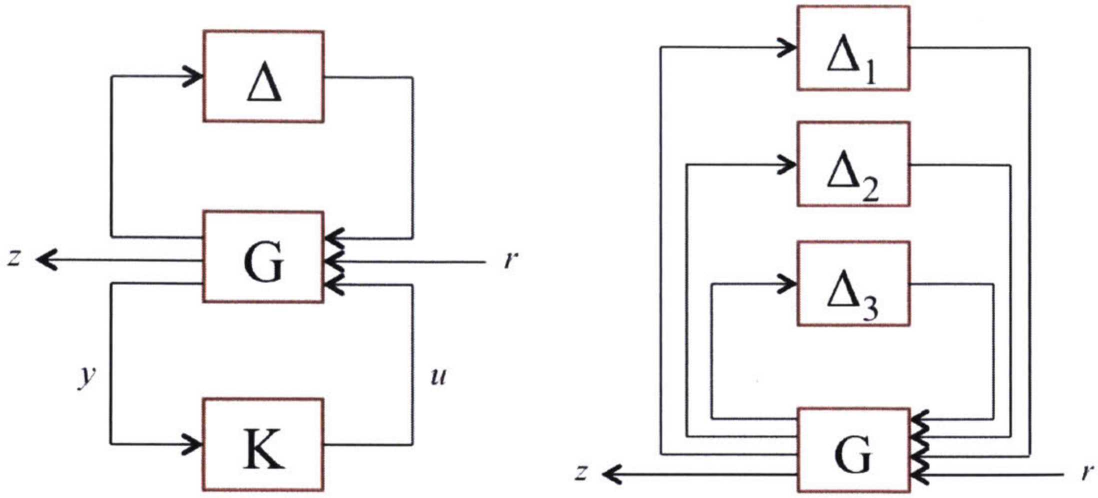

Figure 6-2: The utilization of uncertainty blocks Δ_i for robust control to subsume unmodeled nonlinearities, stochasticity or both. (A) The design of a controller K in the face of an unstructured uncertainty Δ, and (B) the analysis of multiple uncertainties Δ_i on the nominal system G.

An uncertainty block can be used to encompass uncertainty due to unmodeled nonlinear behavior, stochasticity in the system, or both. A detailed exposé of corresponding methods are provided in [117], and we provide a brief overview here. In Section 3.2, an outline of linear fractional transformations (LFT) of systems is provided, also seen in Figure 6-2A. The system G contains known dynamics of the system, while uncertainty or nonlinearities in the system may be subsumed by the system into an unstructured block Δ. As long as Δ can be bounded, i.e. $||\Delta||_\infty < \gamma$, we can analyze the system to prove stability, and moreover, design a controller K in order to stabilize as well as guide the dynamics of the closed loop system.

This provides us a framework in which to deal with unmodeled dynamics. In fact, this procedure is used to prove the results in Chapter 5 of this thesis. Moreover, with additional uncertainty or nonlinear blocks such as in Figure 6-2B, and with knowledge of bounds on each of them, i.e. $||\Delta_i||_\infty < \gamma_i$, the closed loop is only stable if the structured singular value μ of G satisfies some bounds as well (more details in [117]). Thus, it is possible to add details to the models discussed in this thesis, as well as incorporate additional bounded nonlinearities and uncertainties, using concepts from robust control theory.

6.2 Future Work

This thesis presents ideas that are motivated by experimental observations, and rooted in theoretical neuroscience as well as control theory. There are a number of experimental studies that burgeon out of this thesis. I describe some experimental and algorithmic paradigms next. In brief, we would like to record data from relevant motor structures in the brain as well as the neurons directly driving the musculoskeletal system, while the subject performs different types of tasks. Models can be built for the neural activity as well as the musculoskeletal dynamics using algorithms detailed here, and the concepts presented in this thesis can be verified using this experimental data. In general, more experiments need to be designed in order to accurately characterize the fast movement regime, especially in the context of feedback control.

It is extremely important, and the next natural step in the course of this study, to analyze the data sources that we would need to validate the theory, as well as the methods required to fit the relevant models. For this purpose, we describe a summary of an example experiment to conduct, as well as procedures to fit the models described in Chapters 2 and 3. We will also discuss fitting and analysis of network-based models currently used to characterize neural activity.

Moreover, there currently do not exist many experimental studies that quantitatively analyze the movement properties in the 'fast' movement regime, i.e. for high frequency periodic movements where subharmonic oscillations may occur, or at least where subjects start skipping cycles. We will detail one such primate experiment that may be carried out, though many such experiments are conceivable.

6.2.1 Desired Experimental Data for Model Fitting

We can use data from subjects performing reaching tasks in order to fit the relevant models. The desired movements would be simple in nature, only using single joints at a time, in order to not have undue external influences. We would record spiking data from the alpha motor neurons during these experiments; this spiking data can either be directly recorded using extracellular electrodes in the muscles, or via the deconvolution of electromyographic (EMG) signals of the relevant muscles [76]. Since model fitting only needs EMG recordings at the minimum, and is thus noninvasive, this task is amenable for humans as well as primates. Any neural recordings made would be an added bonus that would benefit the model fitting procedure.

Intramuscular EMG activity can be recorded using established techniques [94, 88, 97, 19], each subject can be implanted with bipolar EMG electrodes in multiple upper extremity muscles that act across the shoulder and/or elbow for a reaching task.

A standard setup for the task consists of a screen with a central target and eight peripheral dots. The subject controls the cursor. A green light comes on in the center when the task begins, and when a peripheral dot lights up green, the subject reaches towards that target and performs the relevant task. Only one peripheral dot would be lit at any one time. With timing information also included in the task, we can control how fast we would like the subject to move. Different tasks that would be useful for our purposes are (1) a center-out reaching task from a central location to a peripheral target, (2) one smooth there-and-back movement from the center to a peripheral target and back to the center, and (3) a back-and-forth movement consisting of reaching from the center to a peripheral target multiple times in a row. The desired movements in these cases can be modeled as (1) a step signal, (2) an impulse signal, and (3) a sinusoidal signal. All three of these cases and the expected responses are also discussed in Chapter 2. These desired movements would be $r(t)$, while the actual movement by the cursor would be $z(t)$. During the task, spike trains from alpha motor neurons would be recorded (either directly or via EMG).

In case the reference signal $r(t)$ is not directly provided in given experimental data, it can be estimated using the starting and ending points and the total time taken to get there. To examine the bottlenecks in information transfer in the sensorimotor control pathway, it is also important to record neural activity simultaneously with the experiments. The recorded neural and EMG activity would allow us to build the models discussed in Chapter 2, with example algorithms provided below, and the cutoff frequency can then be calculated using the relevant parameters as in Chapter 3. In order to *validate* the cutoff frequency, we need an experimental paradigm with an explicit reference signal to be tracked.

6.2.2 Offline Closed-Loop System Identification of the Neuronal Model

There exist numerous algorithms to fit a linear dynamical system feeding into a generalized IAF model as described in Chapter 2. Some are given in [58, 85, 83, 106]. We describe a procedure here, heavily following ideas in [85]. We assume that we have access to $r(t)$, $z(t)$, and the alpha motor neuron activity driving the musculoskeletal system, i.e. the spike train $u(t)$. We assume that all the directionally tuned neurons' spike trains can be merged to form $u(t)$. In full generality, we assume that we are recording from a stochastic leaky IAF, i.e. the subthreshold voltage evolves according to the following equation.

$$\frac{dV}{dt} = -aV(t) + \int_0^t k(\tau)e(t-\tau)d\tau + \sigma N_t \tag{6.1}$$

where N_t is standard Gaussian noise, $k(t)$ is the impulse response of K, and $e(t) = r(t) - Fz(t)$. When $V(t)$ reaches a threshold q, it emits a spike. This translates to linear constraints on $V(t)$; we first characterize the evolution of $V(t)$. Between any two spikes t_i and t_{i+1}, i.e. for $t \in [t_i, t_{i+1})$, in the absence of noise ($\sigma = 0$), the membrane voltage evolves as the following.

$$V(t) = V_0 e^{-a(t-t_i)} + \int_{t_i}^t (k \cdot e)(s) e^{-a(t-s)} ds \tag{6.2}$$

Here, V_0 is the reset voltage after a spike, and $(k \cdot e)(s) = \int_0^s k(\tau)e(s-\tau)d\tau$. We first normalize all the above parameters by dividing by q, e.g., $\tilde{V}_0 = \frac{V_0}{q}$, $\tilde{k} = \frac{k}{q}$. We then have that the normalized $V(t)$, i.e. $\tilde{V}(t) = \frac{V(t)}{q}$, emits a spike when it reaches a threshold of 1. It is known that that adding Gaussian noise to $\tilde{V}(t)$ at each time t induces a Gaussian density over $\tilde{V}(t)$, since linear dynamics preserve Gaussianity [55]. Following the nomenclature in [85], we denote this Gaussian density $G(\tilde{V}(t)|r_i, z_i, \theta)$, where $\theta = \{\tilde{k}, \tilde{V}_0, F, a, \sigma\}$, and r_i and z_i are the known chunks of desired and actual movement, that is $r_i \equiv r(t),\ t \in [t_i, t_{i+1})$ and $z_i \equiv z(t),\ t \in [t_i, t_{i+1})$. Over the course of any interspike interval $t \in [t_i, t_{i+1}]$, we know that $\tilde{V}(t)$ is less than 1 for all times before t_{i+1}, and is equal to or greater than 1 at

t_{i+1}. This can be written as the following set of linear constraints on $\tilde{V}(t)$.

$$C_i = \bigcap_{t_i \leq t < t_{i+1}} \{\tilde{V}(t) < 1\} \cap \{\tilde{V}(t_{i+1}) \geq 1\} \tag{6.3}$$

Thus, the likelihood that the neuron first spikes at time t_{i+1}, given that there was a spike at time t_i, is the probability of the event $\tilde{V}(t) \in C_i$, which is given by

$$\int_{\tilde{V} \in C_i} G(\tilde{V}(t)|r_i, z_i, \theta) \tag{6.4}$$

This is the integral of the Gaussian density $G(\tilde{V}(t)|r_i, z_i, \theta)$ over the set C_i of (unobserved) voltage paths consistent with the observed spike train data. The likelihood for the entire spike train is therefore the product of these terms over all observed spikes. The full likelihood can now be written as the following.

$$L_{\{r_i, z_i, t_i\}}(\theta) = \prod_i \int_{\tilde{V} \in C_i} G(\tilde{V}(t)|r_i, z_i, \theta) \tag{6.5}$$

where the product, is over all observed spike times $\{t_i\}$ and corresponding desired and actual movement segments $\{r_i, z_i\}$. As proved in [85], this likelihood has no nonglobal local extrema in the parameters θ for any $\{r_i, z_i, t_i\}$. Thus, the maximum likelihood estimation of θ can now be performed using computational methods described in detail in [85]. Moreover, details of model validation techniques based on [9], also described in [85], are necessary using unobserved data in order to verify that the learnt θ fits the spiking data well.

Fitting a model for M is easier since we have the input spike train $u(t)$, as well as the actual movement output $z(t)$, and we need to fit a linear model to find m, the impulse response of M. There are numerous techniques for this; the standard techniques are provided in [70]. In brief, we can apply linear regression techniques, with regularization if needed.

6.2.3 Verification of Fundamental Limits on Speed

Once we have an identified model for $\tilde{K}$, M, and F, with $q = 1$, we can apply the analysis as in Chapter 3 in order to find ω_c as a function of these parameters. We first investigate whether the estimated fundamental limits on speed are physiologically relevant, given the identified neural model and the musculoskeletal system. We can then test these fundamental limits in an experimental procedure in the same subject. This would be done by using various sinusoidal signals at the increased speeds (Task 3) at frequencies that the subject cannot track well, and starts skipping cycles. The frequency of the target signal would be randomized at each subsequent trial, and the sinusoidal target signals would be interleaved with target signals of other shapes, for ex. ramps and chirps. This is to ensure that the subject cannot predict the next signal, and thus uses a feedback mechanism to make the movement. This speed at which tracking breaks down would be compared to the derived ω_c.

Specifically, at low frequencies, as seen in the data in [14], we expect that the EMG signal and the alpha motor firing show periodic oscillations with frequency roughly equal to the frequency ω of the reference signal $r(t)$. In this low frequency regime, the primate is able to accurately track the sinusoidal signal. In this regime, we can take the discrete Fourier transform of the cursor movement trajectory over multiple trials to quantify the mean power (and the standard deviation around the mean) at subharmonic frequencies ω/k where k is an integer, for $k \in [2, 10]$. These mean values and standard deviations will be used as a 'null model' to evaluate whether there is statistically significant increase in power at subharmonic frequencies for movement frequencies ω beyond the predicted ω_c. Similarly, we can also quantify the overshoot and undershoot in the movement as a function of the reference movement frequency ω. We can use the regime of slow and accurate movement to quantify the null expectations and detect statistically significant overshoots and undershoots for the higher frequency movements.

Further experiments can be performed in order to robustly verify the fundamental limits as they depend on the different system parameters. For example, we can perform reversible inactivation of certain brain structures or directly the alpha motor neurons in order to study the effect on ω_c. Reversible inactivation of the cerebral cortex can be produced by intracortical injection of the GABAA agonist, muscimol, using techniques as detailed in [96, 95]. Muscimol reliably provides a steady, prolonged inactivation of a substantial cortical territory.

6.2.4 Extensions using Neural Data recorded from Brain Structures

Intuitively speaking, the subharmonic regime is reached due to the inability of the neurons to process information 'fast' enough. Although in this thesis we model subharmonics being generated at the level of the alpha motor neurons, the 'bottleneck' could actually be present at any point in the sensorimotor pathway. Here, I detail a possible mechanism to pinpoint the location of the bottleneck, using simultaneous recordings from individual neurons in various structures along the sensorimotor pathway. In diseased states, this could be used to design stimulation paradigms in the identified structures to restore functioning where it is needed.

Modeling Networks of Neurons

In either of the two experiments discussed above, the dynamics of both the neural and EMG data can be modeled in a closed loop sensorimotor control model with a structure as shown in Figure 6-3. Depending on the experimental paradigm, $z(t)$ is commonly a 2 or 3 dimensional signal denoting the dynamics of the recorded angle (position, velocity and acceleration) of a mechanical joystick, or the dynamics of a cursor on a screen. The EMG signal that feeds into the musculoskeletal system M is denoted by $y(t)$ and the proprioceptive and visual feedback denoted by F. The 'error' between the reference signal and the feedback signal $d(t)$ is denoted by $e(t) = r(t) - d(t)$.

We can first fit a model M for muscle activity using the measured EMG activity $y(t)$ and measured movement output $z(t)$. Since the dimension of y is usually much higher than the dimension of z, and there are several trials for each task, we can apply standard linear regression to fit M [70].

Next, we can fit a dynamical model to describe neural activity using the reference sig-

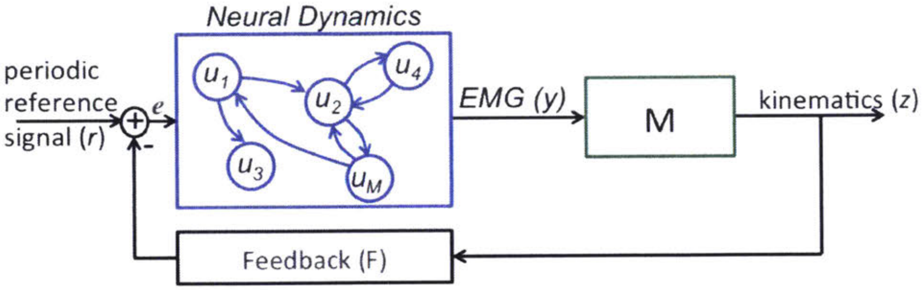

Figure 6-3: The closed loop model of neural activity. We can use a network of gIAF neurons, to model the motor cortex neural dynamics.

nal, the muscle model, and the EMG signal. We model the spiking activity of the neurons as emanating from a spike-based network of interconnected generalized integrate-and-fire (gIAF) neurons [85]. An LTI feedback model F can be fitted concurrently with each of the neural models. We can also incorporate additional data collected from different parts of the motor cortex, cerebellum, and the primary visual cortex directly into this model by adding external currents to this state equation.

Each neuron's spikes is modeled as emanating from a stochastic gIAF (also known as linear-non-linear integrate and fire L-NLIF [85]), which receives its inputs from the error signal as well as the spiking activity of all other neurons. Specifically, for each of the M task-related neurons recorded in the brain with spike trains $u_i(t),\ i \in [1, M]$, the dynamics of the subthreshold voltage V_i at a time t between two spikes $t_{i,n}$ and $t_{i,n+1}$ is described as follows (now expressed in discrete time).

$$V_i(t+1) \quad = \quad -a_iV_i(t) + \sum_{\tau=0}^{t} k_i(\tau)e(t-\tau) + \sum_{j=1}^{M}\sum_{\tau=0}^{t} h_{ij}(\tau)u_j(t-\tau) + w_i(t) \tag{6.6}$$

When V_i reaches a threshold 1, it emits a 'spike', with the spike time represented as $t_{i,n+1}$, and the membrane voltage is reset to V_{i0}. The spike trains $u(t)$ are now a series of 1's and 0's, i.e. 1 at every spike time $\{t_{i,1}, \dots, t_{i,N}\}$, and 0 otherwise. $w_i \sim N(0, \sigma_i)$ represents noise. The parameters $a_i > 0$, $\{k_i(\tau)\}_{i\in[1,M],\tau\in[0,T_1]}$ and $\{h_{ij}(\tau)\}_{i,j\in[1,M],\tau\in[0,T_2]}$ represent the leak factor, the convolutional kernel describing the effect of the input signal on each neuron, and the strength of the interneuronal interactions, respectively. The vector θ to be estimated using maximum likelihood methods consists of these parameters, as well as V_{i0}, and σ_i for $i \in [1, M]$. T_1 and T_2 can be pre-chosen from a distribution of physiologically relevant durations for these different interactions.

The problem of determining θ from data on the spiking times can be cast as a maximum likelihood estimation problem, with no nonglobal local maxima [85]. Briefly, if two consecutive spikes occur at $t_{i,n}$ and $t_{i,n+1}$ for the i^{th} neuron, the probability of observing the interspike interval $t_{i,n+1} - t_{i,n}$ can be calculated given θ, $e(t)$ and entire spike trains from all neurons, i.e. $\{u_i(t)\}_{i \in [1,K]}$. The dynamics of the neuron voltage in the interspike interval can be described by a linear Fokker-Plank equation. Notably, efficient methods have been developed to numerically estimate the probability that a neuron voltage exceeds its threshold in time $t_{i,n+1} - t_{i,n}$ [85, 82, 32]. The total likelihood for a spike train of one neuron is simply a product over all these separate interspike intervals. Assuming that the spike trains of all neurons are mutually *conditionally independent*, i.e. given all spike trains and the input $e(t)$, the network likelihood is the product over all the likelihoods for each neuron.

Despite efficient methods to compute the likelihood, the number of parameters to be estimated may still be prohibitively large. In order to limit the number of fitted parameters, we can impose $\mathcal{L}_1$ regularization to estimate the strength of the interneuronal interactions, thus rendering sparse estimates of the relevant kernels, and $\mathcal{L}_2$ regularization can be used to avoid overfitting. In addition to imposing $\mathcal{L}_1$ regularization, in order to gain tractability, we can impose that individual neurons are governed by a linear combination of multiple spike trains rather than individual spike trains, thus simplifying the matrix of interactions h_{ij}. Moreover, model validation techniques based on [9], also described in [85, 82], are necessary using unobserved data in order to verify that the learnt θ fits the spiking data well. Using MLE methods, a family of networks consistent with the experimental data with different parameters and regularization terms can be obtained.

Next, we can use a two step process to model the EMG as an output of the neural dynamics. We can first model the EMG signal as being produced by alpha motor neuron activity [76]. Next, we can incorporate these motor neurons in the gIAF network model.

In addition to fitting the models to data, we can also investigate whether the models resemble the physiology of motor cortex neurons and whether they are generalizable. Specifically, we can address the following questions. (1) Does a network-based model fit the neural and EMG data better as compared to a linear dynamical system feeding into an IAF, and what does this say about the importance of modeling the network activity? (2) Does the degree of interconnections of the neuronal connections as learnt by the models match the level of known synaptic interconnections in the motor cortex and other recorded structures? (3) Does the model learn connections specifically for the movement types in the experiment, or can I input other types of signals (eg. chirps, triangular), with reasonable tracking accuracy? (4) What is the level of redundancy in the network? For example, if I knock out a subset of the neurons, what is the decline in accuracy of the output?

Approximate methods to find ω_c

For the data as well as the model, we can first investigate the dependence of the accuracy of the movements on their speeds, with the hypothesis being that faster movements are less accurate, as found in earlier motor control experiments as in [29]. Next, for a given model, we can computationally analyze the Fourier spectrum of the output $z(t)$ as a function of the frequency ω of the input $r(t)$ to identify the cutoff frequency ω_c beyond which the output Fourier spectrum shows a significant peak in frequencies ω/k where $k > 1$ is an integer. We expect these outputs to also show undershoot and/or overshoot in the time domain, which can be quantified as well.

We would have at our disposal a family of networks, i.e. a distribution of parameters, that are consistent with the experimental data. We can next explore whether ω_c is robustly predicted across this parameter distribution. Specifically, we can calculate the coefficient of variation of ω_c for the distribution of parameters, and further refine the models if the coefficient of variation (CV) is large. We can test the robustness of ω_c with respect to small changes in model parameters, specifically, the neural and feedback parameters. We can add Gaussian noise with variance σ^2 one-by-one to each parameter, and test the sensitivity of ω_c by calculating the CV of ω_c as compared to σ^2. We can also test the sensitivity of ω_c to the network structure by (1) knocking out a subset of the interneuronal interactions, (2) producing a graded decrease in interneuronal interactions, (3) producing a graded decrease in the parameters dictating the output of the motor cortex neurons to the EMG signal. We hypothesize that these alterations will produce a significantly lower ω_c in all cases.

We can also extend theoretical analyses as discussed in Chapter 3 to develop analytical methods to characterize the maximum speed past which we see undesirable phenomena. This can be done by first exploring the existence of key 'bottleneck' connections where, if the spiking activity is further lowered by increasing the relevant neuronal thresholds, undesirable phenomena will be apparent. Then, we can linearize the remaining connections and thus have a tractable model which retains only the essential nonlinearities. We can proceed as discussed in Chapter 3, to analytically characterize ω_c. Briefly, we can reformulate the closed loop as a switched linear system with possibly a larger number of linear manifolds, and build a Poincaré map to analytically calculate the switching times and thus ω that lead to subharmonic oscillations.

If the network model fails to show subharmonic behavior, or if ω_c is significantly variable across multiple maximum likelihood estimated models, we can constrain the models further by requiring that the output of the neural activity not only reproduce the experimentally measured EMG signal but also the experimentally measured kinematics. This may further constrains the models to show physiologically realistic properties. We can then carry out the above computational analysis on these constrained models.

Validating ω_c and characterizing the 'information bottleneck'

Next, we can identify the regions of the sensorimotor system that act as 'information bottlenecks' giving rise to subharmonic oscillations. When $\omega > \omega_c$, we hypothesize that (a) the EMG signal displays subharmonic oscillations since the kinematics are a direct result of the muscle activity, and (b) that a subset of the motor cortex neurons display subharmonic oscillations since there exist direct connections to the alpha motor neuron activity driving the EMG signal. Intuitively speaking, the subharmonic regime is reached due to the inability of the neurons to process information 'fast' enough. The motor cortex receives inputs from several structures, and we may see both harmonic and subharmonic activity by the neurons. Moreover, with recordings from a variety of the structures involved in sensorimotor control, we may be able to pinpoint where the activity of the neurons

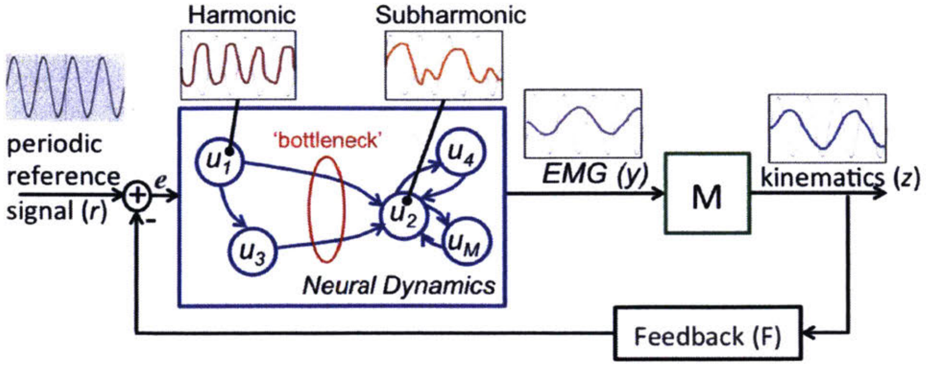

Figure 6-4: Hypothetical data in the subharmonic regime. The reference signal is a sinusoidal signal, shown in the background of every signal. The cursor kinematics as well as the example EMG signal are periodic with $1/2$ the driving frequency. The neuronal activity shows a dichotomy of responses, allowing us to characterize the 'bottleneck' as the connections where the harmonic responses switch to subharmonics.

switches from harmonic to subharmonic. As a result, we would be able to identify the *bottleneck* for the transfer of information as the structure at which the activity switches from harmonic to subharmonic oscillations (see Fig. 6-4 as an example). This idea holds in particular for tree structures of graphs, and to elucidate it further, a tree structure can be imposed when learning the parameters of the network model in the previous section. If the majority of the motor cortex neurons fire at the reference movement frequency while the EMG signal shows subharmonic oscillations, we can conclude that the bottleneck for the transfer of information lies between the motor cortex and the alpha motor neurons.

It is also conceivable to implement the real-time decoder in feedback as discussed earlier in this thesis, and investigate (a) the stability and performance of this decoder in feedback, and (b) the existence of undesirable phenomena with this decoder in feedback. The implementation of such a decoder would require real-time spike sorting from recorded data - either EMG signals or extracellularly recorded brain structures.

If the primate fails to display regular subharmonic oscillations due to lack of incentive in the high frequency regime or due to noisy movement signals from one trial to the next, we can analyze the inaccuracies for high frequency movements, including undershoot, overshoot, and lack of robustness of responses, and analyze the neural mechanisms for these undesirable phenomena using similar models.

We provided one testable hypothesis in this chapter emanating directly from the theoretical work in this thesis. There are a number of intriguing experiments and fresh analyses conceivable within the framework outlined in this work. We hope to have provided the rudiments for research directed towards further elucidating the neural control of movement.

Bibliography

[1] William Abend, Emilio Bizzi, and Pietro Morasso. Human arm trajectory formation. *Brain: a journal of neurology*, 105(Pt 2):331–348, 1982.

[2] GI Allen and N Tsukahara. Cerebrocerebellar communication systems. *Physiological reviews*, 54(4):957–1006, 1974.

[3] Kai-Nan An, FC Hui, BF Morrey, RL Linscheid, and EY Chao. Muscles across the elbow joint: a biomechanical analysis. *Journal of biomechanics*, 14(10):659–669, 1981.

[4] Riccardo Barbieri, M. C. Quirk, L. M. Frank, M. A. Wilson, and Emery N. Brown. Construction and analysis of non-poisson stimulus-response models of neural spiking activity. *J Neurosci Methods*, 105:25–37, 2001.

[5] George EP Box. Robustness in the strategy of scientific model building. *Robustness in statistics*, 1:201–236, 1979.

[6] Romain Brette and Wulfram Gerstner. Adaptive exponential integrate-and-fire model as an effective description of neuronal activity. *Journal of neurophysiology*, 94(5):3637–3642, 2005.

[7] VB Brooks. Some examples of programmed limb movements. *Brain research*, 71(2-3):299–308, 1974.

[8] Vernon B Brooks. *The neural basis of motor control.* Oxford University Press, 1986.

[9] Emery N Brown, Riccardo Barbieri, Valérie Ventura, Robert E Kass, and Loren M Frank. The time-rescaling theorem and its application to neural spike train data analysis. *Neural computation*, 14(2):325–346, 2002.

[10] Emery N Brown, Loren M Frank, Dengda Tang, Michael C Quirk, and Matthew A Wilson. A statistical paradigm for neural spike train decoding applied to position prediction from ensemble firing patterns of rat hippocampal place cells. *The Journal of Neuroscience*, 18(18):7411–7425, 1998.

[11] Nicolas Brunel and Mark CW Van Rossum. LapicqueâĂŹs 1907 paper: from frogs to integrate-and-fire. *Biological cybernetics*, 97(5):337–339, 2007.

[12] P Butzer, Hans G. Feichtinger, and Karlheinz Gröchenig. Error analysis in regular and irregular sampling theory. *Applicable Analysis*, 50(3-4):167–189, 1993.

[13] Jose M Carmena, Mikhail A Lebedev, Roy E Crist, Joseph E O'Doherty, David M Santucci, Dragan F Dimitrov, Parag G Patil, Craig S Henriquez, and Miguel AL Nicolelis. Learning to control a brain–machine interface for reaching and grasping by primates. *PLoS biology*, 1(2):e42, 2003.

[14] Mark M Churchland, John P Cunningham, Matthew T Kaufman, Justin D Foster, Paul Nuyujukian, Stephen I Ryu, and Krishna V Shenoy. Neural population dynamics during reaching. *Nature*, 487(7405):51, 2012.

[15] RI Close. Dynamic properties of mammalian skeletal muscles. *Physiological reviews*, 52(1):129–197, 1972.

[16] David Cofer, Gennady Cymbalyuk, James Reid, Ying Zhu, William J Heitler, and Donald H Edwards. Animatlab: a 3d graphics environment for neuromechanical simulations. *Journal of neuroscience methods*, 187(2):280–288, 2010.

[17] D. R. Cox and V. Isham. *Point Processes.* CRC, Boca Raton, FL, 2000.

[18] Kenneth JW Craik. Theory of the human operator in control systems. *British journal of psychology*, 38(2):56–61, 1947.

[19] Adam G Davidson, Vanessa Chan, Ryan O'Dell, and Marc H Schieber. Rapid changes in throughput from single motor cortex neurons to muscle activity. *Science*, 318(5858):1934–1937, 2007.

[20] Peter Dayan and Laurence F Abbott. *Theoretical neuroscience.* Cambridge, MA: MIT Press, 2001.

[21] Charles A Desoer and Mathukumalli Vidyasagar. *Feedback systems: input-output properties*, volume 55. SIAM, 2009.

[22] Kenji Doya. *Bayesian brain: Probabilistic approaches to neural coding*. MIT press, 2007.

[23] Uri T Eden, Loren M Frank, Riccardo Barbieri, Victor Solo, and Emery N Brown. Dynamic analysis of neural encoding by point process adaptive filtering. *Neural Computation*, 16(5):971–998, 2004.

[24] S F Farmer. Pulsatile central nervous control of human movement. *J.Physiol.*, 517(1):3, 1999.

[25] Hans G Feichtinger and Karlheinz Gröchenig. Irregular sampling theorems and series expansions of band-limited functions. *Journal of mathematical analysis and applications*, 167(2):530–556, 1992.

[26] Hans G Feichtinger and Karlheinz Gröchenig. Theory and practice of irregular sampling. *Wavelets: mathematics and applications*, 1994:305–363, 1994.

[27] Hans G Feichtinger, José C Príncipe, José Luis Romero, Alexander Singh Alvarado, and Gino Angelo Velasco. Approximate reconstruction of bandlimited functions for the integrate and fire sampler. *Advances in computational mathematics*, 36(1):67–78, 2012.

[28] Alon Fishbach, Stephane A. Roy, Christina Bastianen, Lee E. Miller, and James C. Houk. Deciding when and how to correct a movement: Discrete submovements as a decision making process. *Experimental Brain Research*, 177(1):45–63, 2007.

[29] Paul M Fitts. The information capacity of the human motor system in controlling the amplitude of movement. *Journal of experimental psychology*, 47(6):381, 1954.

[30] AF Fuchs. Periodic eye tracking in the monkey. *The Journal of physiology*, 193(1):161, 1967.

[31] Andrew J Fuglevand, DAVID A Winter, and AFTAB E Patla. Models of recruitment and rate coding organization in motor-unit pools. *Journal of neurophysiology*, 70(6):2470–2488, 1993.

[32] Alan Genz. Numerical computation of multivariate normal probabilities. *Journal of computational and graphical statistics*, 1(2):141–149, 1992.

[33] Wulfram Gerstner and Werner M Kistler. *Spiking neuron models: Single neurons, populations, plasticity*. Cambridge university press, 2002.

[34] Claude Ghez. Muscles: effectors of the motor systems. *Principles of neural science*, pages 548–563, 1991.

[35] David Gontier and Martin Vetterli. Sampling based on timing: Time encoding machines on shift-invariant subspaces. *Applied and Computational Harmonic Analysis*, 36(1):63–78, 2014.

[36] DG Goroso, RRL Cisi, and AF Kohn. The amplitude and phase responses of the firing rates of some motoneuron models. *Biosystems*, 58(1):33–39, 2000.

[37] S Hanneton, a Berthoz, J Droulez, and J J Slotine. Does the brain use sliding variables for the control of movements? *Biological cybernetics*, 77(6):381–393, 1997.

[38] CJ Heckman, Michael Johnson, Carol Mottram, and Jenna Schuster. Persistent inward currents in spinal motoneurons and their influence on human motoneuron firing patterns. *The Neuroscientist*, 2008.

[39] Elwood Henneman and Lorne Mendell. Functional organization of motoneuron pool and its inputs. *Handbook of physiology*, pages 423–507, 1981.

[40] Elwood Henneman and Lorne M Mendell. Functional organization of motoneuron pool and its inputs. *Comprehensive Physiology*, 2011.

[41] Elwood Henneman, George Somjen, and David O Carpenter. Excitability and inhibitibility of motoneurons of different sizes. *Journal of neurophysiology*, 28(3):599–620, 1965.

[42] JL Hindmarsh and RM Rose. A model of the nerve impulse using two first-order differential equations. *Nature*, 296(5853):162–164, 1982.

[43] AL Hodgkin and Pv Horowicz. The influence of potassium and chloride ions on the membrane potential of single muscle fibres. *The Journal of physiology*, 148(1):127–160, 1959.

[44] Alan L Hodgkin and Andrew F Huxley. A quantitative description of membrane current and its application to conduction and excitation in nerve. *The Journal of physiology*, 117(4):500, 1952.

[45] Neville Hogan. Adaptive control of mechanical impedance by coactivation of antagonist muscles. *IEEE Transactions on Automatic Control*, 29(8):681–690, 1984.

[46] Gordon Holmes. The goulstonian lectures on spinal injuries of warfare: delivered before the royal college of physicians of london. *British medical journal*, 2(2867):855, 1915.

[47] James C Houk, William Z Rymer, and Patrick E Crago. Dependence of dynamic response of spindle receptors on muscle length and velocity. *Journal of Neurophysiology*, 46(1):143–166, 1981.

[48] Eugene M Izhikevich et al. Simple model of spiking neurons. *IEEE Transactions on neural networks*, 14(6):1569–1572, 2003.

[49] Eugene M Izhikevich and Richard FitzHugh. Fitzhugh-nagumo model. *Scholarpedia*, 1(9):1349, 2006.

[50] Thomas M Jessell. Neuronal specification in the spinal cord: inductive signals and transcriptional codes. *Nature Reviews Genetics*, 1(1):20–29, 2000.

[51] Sungho Jo and Steve G Massaquoi. A model of cerebellum stabilized and scheduled hybrid long-loop control of upright balance. *Biological cybernetics*, 91(3):188–202, 2004.

[52] Sungho Jo and Steve G Massaquoi. A model of cerebrocerebello-spinomuscular interaction in the sagittal control of human walking. *Biological Cybernetics*, 96(3):279–307, 2007.

[53] Hans Joachim Büdingen and Hans-Joachim Freund. The relationship between the rate of rise of isometric tension and motor unit recruitment in a human forearm muscle. *Pflügers Archiv European Journal of Physiology*, 362(1):61–67, 1976.

[54] Eric R Kandel, James H Schwartz, Thomas M Jessell, et al. *Principles of neural science*, volume 4. McGraw-Hill New York, 2000.

[55] Samuel Karlin and Howard E Taylor. *A second course in stochastic processes*. Elsevier, 1981.

[56] Mario Kleiner, David Brainard, Denis Pelli, Allen Ingling, Richard Murray, Christopher Broussard, et al. What's new in psychtoolbox-3. *Perception*, 36(14):1, 2007.

[57] Konrad P Körding and Daniel M Wolpert. Bayesian decision theory in sensorimotor control. *Trends in cognitive sciences*, 10(7):319–326, 2006.

[58] Shinsuke Koyama and Liam Paninski. Efficient computation of the maximum a posteriori path and parameter estimation in integrate-and-fire and more general state-space models. *Journal of computational neuroscience*, 29(1):89–105, 2010.

[59] F Lacquaniti, M Carrozzo, and NA Borghese. Time-varying mechanical behavior of multijointed arm in man. *Journal of neurophysiology*, 69(5):1443–1464, 1993.

[60] Louis Lapicque. Recherches quatitatives sur l'excitation electrique des nerfs traitee comme polarisation. *J. Physiol. Pathol. Gen.*, 9:620–635, 1907.

[61] Aurel A Lazar. Time encoding with an integrate-and-fire neuron with a refractory period. *Neurocomputing*, 58:53–58, 2004.

[62] Aurel A Lazar. Multichannel time encoding with integrate-and-fire neurons. *Neurocomputing*, 65-66:401–407, 2005.

[63] Aurel A Lazar. Information representation with an ensemble of hodgkin–huxley neurons. *Neurocomputing*, 70(10):1764–1771, 2007.

[64] Aurel A Lazar. Population encoding with hodgkin–huxley neurons. *Information Theory, IEEE Transactions on*, 56(2):821–837, 2010.

[65] Aurel A Lazar and Eftychios A Pnevmatikakis. Faithful representation of stimuli with a population of integrate-and-fire neurons. *Neural computation*, 20(11):2715–2744, 2008.

[66] Aurel A Lazar and Eftychios A Pnevmatikakis. Reconstruction of sensory stimuli encoded with integrate-and-fire neurons with random thresholds. *EURASIP Journal on Advances in Signal Processing*, 2009:3, 2009.

[67] Aurel A Lazar and László T Tóth. Time encoding and perfect recovery of bandlimited signals. *Proceedings of the ICASSP*, 3:709–712, 2003.

[68] Aurel A Lazar and László T Tóth. Perfect recovery and sensitivity analysis of time encoded bandlimited signals. *Circuits and Systems I: Regular Papers, IEEE Transactions on*, 51(10):2060–2073, 2004.

[69] RJ Leigh and DS Zee. Smooth pursuit and visual fixation. *The neurology of eye movements, Ed*, 2:139–166, 1991.

[70] Lennart Ljung. System identification. In *Signal Analysis and Prediction*, pages 163–173. Springer, 1998.

[71] I D Loram, H Gollee, M Lakie, and P J Gawthrop. Human control of an inverted pendulum: is continuous control necessary? Is intermittent control effective? Is intermittent control physiological? *The Journal of Physiology*, 589(2):307–324, 2011.

[72] Ian David Loram, Cornelis Van De Kamp, Martin Lakie, Henrik Gollee, and Peter J. Gawthrop. Does the motor system need intermittent control? *Exercise and Sport Sciences Reviews*, 42(3):117–125, 2014.

[73] Zachary F Mainen, Jasdan Joerges, John R Huguenard, and Terrence J Sejnowski. A model of spike initiation in neocortical pyramidal neurons. *Neuron*, 15(6):1427–1439, 1995.

[74] Steve G Massaquoi and Helge Topka. Models of cerebellar function. *The cerebellum and its disorders. Cambridge University Press, Cambridge*, pages 69–94, 2002.

[75] Joseph McIntyre and Emilio Bizzi. Servo hypotheses for the biological control of movement. *Journal of motor behavior*, 25(3):193–202, 1993.

[76] Roberto Merletti and Philip A Parker. *Electromyography: physiology, engineering, and non-invasive applications*, volume 11. John Wiley & Sons, 2004.

[77] R. C. Miall, D. J. Weir, and J. F. Stein. Intermittency in human manual tracking tasks. *Journal of Motor Behavior*, 25(1):53–63, 1993.

[78] Vernon B Mountcastle. Modality and topographic properties of single neurons of cat's somatic sensory cortex. *Journal of Neurophysiology*, 1957.

[79] Fernando Navas and Lawrence Stark. Sampling or intermittency in hand control system dynamics. *Biophysical Journal*, 8(2):252–302, 1968.

[80] Miguel A. L Nicolelis, Asif A Ghazanfar, Barbara M Faggin, Scott Votaw, and Laura M. O Oliveira. Reconstructing the engram: Simultaneous, multisite, many single neuron recordings. *Neuron*, 18(4):529 – 537, 1997.

[81] K. Novak, L. Miller, and J. Houk. The use of overlapping submovements in the control of rapid hand movements. *Experimental Brain Research*, 144(3):351–364, 2002.

[82] Murat Okatan, Matthew A Wilson, and Emery N Brown. Analyzing functional connectivity using a network likelihood model of ensemble neural spiking activity. *Neural computation*, 17(9):1927–1961, 2005.

[83] Liam Paninski. Maximum likelihood estimation of cascade point-process neural encoding models. *Network: Computation in Neural Systems*, 15(4):243–262, 2004.

[84] Liam Paninski, Jonathan Pillow, and Jeremy Lewi. Statistical models for neural encoding, decoding, and optimal stimulus design. *Progress in brain research*, 165:493–507, 2007.

[85] Liam Paninski, Eero P Simoncelli, and Jonathan W Pillow. Maximum likelihood estimation of a stochastic integrate-and-fire neural model. In *Advances in Neural Information Processing Systems*, pages 1311–1318, 2004.

[86] Brodal Per. *The Central Nervous System: Structure and Function.* Oxford University Press, 1998.

[87] J Andrew Pruszynski and Stephen H Scott. Optimal feedback control and the long-latency stretch response. *Experimental brain research*, 218(3):341–359, 2012.

[88] Adam G Rouse and Marc H Schieber. Spatiotemporal distribution of location and object effects in primary motor cortex neurons during reach-to-grasp. *Journal of Neuroscience*, 36(41):10640–10653, 2016.

[89] S. V. Sarma, Uri T. Eden, Ming L. Cheng, Ziv M. Williams, Rollin Hu, Emad Eskandar, and Emery N. Brown. Using point process models to compare neuronal activity in sub-thalamic nucleus of parkinson's patients and a healthy primate. *IEEE Trans on Biomed Eng*, 57:1297–1305, 2010.

[90] Sridevi V Sarma and Munther A Dahleh. Remote control over noisy communication channels: A first-order example. *Automatic Control, IEEE Transactions on*, 52(2):284–289, 2007.

[91] Sridevi V Sarma and Munther A Dahleh. Signal reconstruction in the presence of finite-rate measurements: finite-horizon control applications. *International Journal of Robust and Nonlinear Control*, 20(1):41–58, 2010.

[92] S. Saxena, S. Santaniello, E. B. Montgomery, J. T. Gale, and S. V. Sarma. Point process models show temporal dependencies of basal ganglia nuclei under deep brain stimulation. In *Proc.* 32^{nd} *IEEE EMBS Conference*, Buenos Aires, AR, 2010.

[93] Shreya Saxena and Munther Dahleh. Real-time decoding of an integrate and fire encoder. In *Advances in Neural Information Processing Systems*, pages 2906–2914, 2014.

[94] Marc H Schieber. Muscular production of individuated finger movements: the roles of extrinsic finger muscles. *The Journal of Neuroscience*, 15(1):284–297, 1995.

[95] Marc H Schieber. Inactivation of the ventral premotor cortex biases the laterality of motoric choices. *Experimental brain research*, 130(4):497–507, 2000.

[96] Marc H Schieber and Andrew V Poliakov. Partial inactivation of the primary motor cortex hand area: effects on individuated finger movements. *The Journal of neuroscience*, 18(21):9038–9054, 1998.

[97] Marc H Schieber and Gil Rivlis. A spectrum from pure post-spike effects to synchrony effects in spike-triggered averages of electromyographic activity during skilled finger movements. *Journal of neurophysiology*, 94(5):3325–3341, 2005.

[98] R. Schmid and S. Ron. A model of eye tracking of periodic square wave target motion. *Biological Cybernetics*, 54(3):179–187, 1986.

[99] Mijail D Serruya, Nicholas G Hatsopoulos, Liam Paninski, Matthew R Fellows, and John P Donoghue. Brain-machine interface: Instant neural control of a movement signal. *Nature*, 416(6877):141–142, 2002.

[100] R Shadmehr and SP Wise. A simple muscle model. *Supplement to (Shadmehr and Wise, 2005a). Online at http://www. shadmehrlab.org/book/musclemodel.pdf*, 2005.

[101] Reza Shadmehr, Maurice A Smith, and John W Krakauer. Error correction, sensory prediction, and adaptation in motor control. *Annual review of neuroscience*, 33:89–108, 2010.

[102] D. L. Snyder and M. I. Miller. *Random Point Processes in Time and Space*. Springer, New York, NY, 1991.

[103] L Squire and JW Brown. The history of neuroscience in autobiography, vol. 1. *Journal of Nervous and Mental Disease*, 186(4):250, 1998.

[104] WT Thach, JG Perry, SA Kane, and HP Goodkin. Cerebellar nuclei: rapid alternating movement, motor somatotopy, and a mechanism for the control of muscle synergy. *Revue neurologique*, 149(11):607–628, 1992.

[105] Emanuel Todorov and Michael I Jordan. Optimal feedback control as a theory of motor coordination. *Nature neuroscience*, 5(11):1226–1235, 2002.

[106] Howell Tong. *Threshold models in non-linear time series analysis*, volume 21. Springer Science & Business Media, 2012.

[107] Wilson Truccolo, Uri T. Eden, Matthew R. Fellows, John P. Donoghue, and Emery N. Brown. A point process framework for relating neural spiking activity for spiking history, neural ensemble and extrinsic covariate effects. *J Neurophys*, 93:1074–1089, 2005.

[108] Margaret A Vince. Corrective movements in a pursuit task. *Quarterly Journal of Experimental Psychology*, 1(2):85–103, 1948.

[109] Charles Watson, Matthew Kirkcaldie, and George Paxinos. *The brain: an introduction to functional neuroanatomy*. Academic Press, 2010.

[110] Jack M Winters. How detailed should muscle models be to understand multi-joint movement coordination? *Human Movement Science*, 14(4):401–442, 1995.

[111] D M Wolpert, R C Miall, J L Winter, and J F Stein. Evidence for an Error Deadzone in Compensatory Tracking. *Journal of Motor Behavior*, 24(4):299, 1992.

[112] Daniel M Wolpert. Probabilistic models in human sensorimotor control. *Human movement science*, 26(4):511–524, 2007.

[113] Daniel M Wolpert, Zoubin Ghahramani, and Michael I Jordan. An internal model for sensorimotor integration. *Science-AAAS-Weekly Paper Edition*, 269(5232):1880–1882, 1995.

[114] Wei Wu, Jayant E Kulkarni, Nicholas G Hatsopoulos, and Liam Paninski. Neural decoding of hand motion using a linear state-space model with hidden states. *Neural Systems and Rehabilitation Engineering, IEEE Transactions on*, 17(4):370–378, 2009.

[115] George Ireneus Zahalak. A distribution-moment approximation for kinetic theories of muscular contraction. *Mathematical Biosciences*, 55(1-2):89–114, 1981.

[116] Felix E Zajac and Jack M Winters. Modeling musculoskeletal movement systems: joint and body segmental dynamics, musculoskeletal actuation, and neuromuscular control. *Multiple muscle systems: Biomechanics and movement organization*, 8:121–148, 1990.

[117] Kemin Zhou and John Comstock Doyle. *Essentials of robust control*, volume 104. Prentice hall Upper Saddle River, NJ, 1998.

[118] Kemin Zhou, John Comstock Doyle, Keith Glover, et al. *Robust and optimal control*, volume 40. Prentice hall New Jersey, 1996.